TECHNISCHE
UNIVERSITÄT
WIEN
Vienna University of Technology

DIPLOMARBEIT

Vibrations and Diffusion in Colloidal Cluster Crystals

Ausgeführt am Institut für

Theoretische Physik

der Technischen Universität Wien

unter der Anleitung von

Ao.Univ.Prof. Dipl.-Ing. Dr. Gerhard Kahl und

Dr. Daniele Coslovich

durch

Lukas Strauss

Schubertstraße 12, 2460 Bruck/Leitha

2. November 2009

Kurzfassung

In der Physik der weichen Materie haben in den letzten Jahren die noch wenig bekannten „Cluster-Phasen" großes Interesse hervorgerufen. Diese Phasen wurden etwa in Systemen entdeckt, in denen Teilchen durch beschränkte, rein abstoßende Potentiale miteinander wechselwirken, die wiederum auf effektiven Wechselwirkungen zwischen weichen Kolloiden (z.B. Dendrimeren) beruhen. Bei entsprechend hohen Dichten bilden sich in jenen Systemen Cluster von überlappenden Teilchen, die sich an den regelmäßigen Punkten eines Kristallgitters anordnen. Diese Cluster-Kristalle haben erstaunliche Eigenschaften wie sie bislang in der harten Materie noch nicht angetroffen wurden. So reagiert das System auf Kompression durch Vergrößerung der Cluster, während die Gitterabstände im Kristall unverändert bleiben. In der vorliegenden Arbeit untersuchen wir die dynamischen Eigenschaften von Cluster-Kristallen mithilfe von Molekulardynamik-Simulationen. Um das Spektrum der Schwingungen in derartigen Systemen zu charakterisieren, wenden wir eigens entwickelte Techniken zur Datenanalyse an. Basierend auf unseren Ergebnissen können wir zwei verschiedene Arten von Teilchenvibrationen identifizieren, die der Bewegung einzelner Teilchen und kollektiver Bewegung entsprechen. In den betrachteten Cluster-Kristallen findet Diffusion dadurch statt, dass Teilchen zwischen den einzelnen Clustern springen. Wir untersuchen dieses Verhalten im Detail und zeigen, dass ein wesentlicher Anteil der Teilchensprünge hoch korreliert ist und weit über die Distanz zu nächsten Nachbarn hinausgeht. Unsere Resultate gewähren somit tieferen Einblick in die mikroskopischen Diffusionsmechanismen, die in Cluster-Kristallen vor sich gehen.

Abstract

In soft matter physics novel kinds of "cluster phases" have attracted considerable attention recently. These phases are observed, for instance, in systems in which particles interact via bounded, purely repulsive potentials that originate from the effective interactions between soft colloids, such as dendrimers. At sufficiently high densities these particles overlap, thereby forming clusters which occupy the regular sites of a cubic lattice. These cluster crystals exhibit astonishing new features that have not been encountered in hard matter so far. Such systems react upon compression by increasing the average cluster size while the lattice spacings remain constant. In the present work, we study the dynamic properties of cluster crystals by means of molecular dynamics simulations. We employ advanced data analysis techniques to characterise the spectrum of vibrations in such systems. We identify two different kinds of oscillatory motion of particles in the system, corresponding to single-particle and collective motion. In the cluster crystals under consideration, diffusion takes place through so-called particle hopping processes between distinct cluster sites. We analyse the behaviour of hopping particles in detail and show that a significant fraction of hopping events is highly correlated and involves particles travelling over many nearest-neighbour distances. Our results shed some new light on the microscopic mechanisms of diffusion at work in cluster crystals.

Contents

Introduction

Milk, paint, gels, cosmetics, blood, proteins, DNA, liquid crystals, pharmaceuticals, ... – what do all of these substances have in common? Quite generally, they can be classified as *soft* matter – ubiquitous in our daily lives.

A particular kind of soft matter systems is the class of *colloidal dispersions* or *complex fluids*. Such systems consist of *mesoscopic* particles, i.e. particles with typical sizes ranging from 1 nm to 1 μm, that are dispersed in a solvent formed by particles of microscopic size. The mesoscopic particles, or *colloids*[1] (such as polymer chains, dendrimers, or microgels) in turn are usually composed of a large number of atoms or molecules. Nowadays, these microscopic building blocks can be assembled in the laboratory so as to control the architecture and chemical nature of colloids and steer their macroscopic properties. In a similar way, the properties of the solvent can be influenced, leading to substantial modifications in the interactions between the dispersed mesoscopic particles. Colloids can thus be considered as "designer atoms" whose shape and interactions can be selected with ease to the wish of the scientist or the need of the application.

A theoretical description of colloidal systems in soft matter physics appears very hard to grasp at first, owing to the huge number of degrees of freedom contained in every single colloidal particle as well as all solvent particles. For this reason, suitable coarse-graining procedures [1] have to be employed, in which, first, the degrees of freedom of all solvent particles are traced out. In a second step, the degrees of freedom of the constituent microscopic particles of the colloids are averaged out, with the aim of deriving a simplified description of the interaction between two of these macromolecules. Consequently, the mesoscopic aggregates are represented by their centres of mass, interacting by means of an *effective* potential. Within this approach, the thermodynamic properties of the soft matter system remain unaffected and the problem becomes treatable with well-known techniques of statistical mechanics.

The vast range of macromolecular complexes that can nowadays be synthesised in the lab or conceived *in silico*, on the computer, leads to an enormous diversity of effective potentials, and thus to an unprecedented, rich variety of new phase behaviours.

---

[1]The term "colloid" derives from the Greek words κόλλα (glue) and είδος (kind).

Prominent examples of the latter are the "re-entrant melting" behaviour and the "clustering" behaviour encountered in systems interacting via *bounded, purely repulsive* potentials. The second of these two phenomena is particularly interesting due to its counter-intuitive character: for sufficiently steep potentials, the formation of clusters in the complete absence of attraction is observed. It is on energetic grounds that, at high densities, aggregates of overlapping particles form *cluster crystals*, i.e. crystals with multiply occupied lattice sites, which exhibit astonishing features such as a density-independent lattice constant and a remarkable way of responding to compression [2, 3]. In computer simulations, amphiphilic dendrimers [4, 5] were found to interact via the above interactions, which allow these macromolecules to overlap or even penetrate each other, without violating excluded volume conditions on the monomeric level.

In the present work, we focus on the characterisation of the dynamic properties of the above cluster crystals. We study the spectrum of vibrations due to both single-particle oscillations as well as the coherent motion of particles in clusters. In addition, we investigate the diffusive behaviour of particles and find that it remarkably differs from the one encountered in single-occupancy crystals. For these purposes, Monte Carlo and molecular dynamics simulations are carried out for a representative ultrasoft, purely repulsive potential, the so-called *generalised exponential model of index 4* (GEM-4) [2, 6]. Our data analysis is based on a newly developed cluster analysis tool, designed to follow each particle's individual trajectory with respect to the cluster centres of mass in time.

Our work is organised as follows: In **Chapter 1** we provide the basic theoretical background necessary to understand the thermodynamics of multiple-occupancy crystals. In **Chapter 2** we introduce the basic elements of the molecular simulation methods applied in our studies. In **Chapter 3** we give an overview of the most relevant thermodynamic quantities and introduce the concept of normal mode analysis. Subsequently, we present our cluster analysis algorithm in detail. Our results on vibrations and diffusion in cluster crystals obtained by molecular dynamics simulations will be discussed in **Chapter 4** and **5**. In **Conclusion**, we summarise the key results of our work.

Chapter 1

Theoretical background

To be able to understand how clusters can form in a system of ultrasoft, repulsive particles, it is indispensable to start with a basic theoretical background for the description of multiple-occupancy crystals.

In Section 1.1 we introduce our model interaction and present a criterion for the occurrence of the clustering phenomenon. In Section 1.2 we focus on the description of ordered cluster phases through density functional theory. The most important results on the statics of clustering systems and recent ideas about their dynamic properties, on which this work is based, will be summarised in Section 1.3.

1.1 Model

1.1.1 The generalised exponential model of index n

The spherically symmetric pair interactions that we consider in the present work originate from a particular class of one-component model systems. In this specific class of systems, particles interact via a bounded, purely repulsive potential which has been given the name "*generalised exponential model of index n*" (GEM-n) [2]. Potentials of the GEM-n class share the same analytical form,

$$\phi(r) = \varepsilon \, e^{-(r/\sigma)^n}. \tag{1.1}$$

While the quantities ε and σ set the characteristic energy and length scale of GEM-n systems, the non-negative real parameter n triggers the steepness of the repulsion. Since the 1970s mainly two representatives of the GEM-n class have been under most frequent discussion: the *Gaussian core model* (GCM) [7] and the *penetrable sphere*

model (PSM) [8]. In their functional form they are given by

$$\text{GCM:} \qquad \phi(r) = \varepsilon\, e^{-(r/\sigma)^2}$$

$$\text{PSM:} \qquad \phi(r) = \begin{cases} \varepsilon & r < \sigma \\ 0 & \text{else} \end{cases}. \tag{1.2}$$

The GCM potential is identical to the GEM-n for $n = 2$, GEM-2, whereas the PSM potential is obtained in the limit $n \to \infty$ leading to a GEM-∞ interaction (see Fig. 1.1).

More recently [6], the GEM-n family as a whole, for all possible values of n, has started attracting the attention of a broader scientific community. Above all, this is owed to the fact that among the members of this particular interaction class two surprisingly different phase behaviours are encountered, depending on the index n and thus on the steepness of the potential. In Fig. 1.2 a schematic representation of the phase diagrams of PSM and GCM systems is shown. Despite the fact that both of them are members of the GEM-n family, the phase diagrams of the two models exhibit a qualitatively very different topology. Upon increasing the density at fixed temperature in systems interacting via the PSM, a mechanism sets in that has been referred to as "*clustering*" [8]. At the sites of a regular Bravais lattice, overlapping particles begin to agglomerate to homogeneously sized clusters. In contrast to this behaviour, when compressing a GCM system at constant temperature T below a so-called upper freezing temperature T_{u}, a first-order transition from the fluid to a crystalline phase is observed, where single particles occupy the lattice sites. Upon further increase in density the solid system melts again, which has got known as "*re-entrant melting*".

1.1.2   Clustering criterion

The fact that the GCM and the PSM belong to the same class of bounded, purely repulsive interactions, yet react in such a contrary fashion to an increase in density, immediately asks for an explanation. Obviously, the value of n, i.e. the steepness of the interaction, must play a crucial role, leading to the two different phase behaviours. And indeed, Likos *et al.* [10] established a criterion to decide whether clustering or re-entrant melting will be observed in a system where particles interact via ultrasoft, purely repulsive potentials. Being based on the analysis of the behaviour of the structure factor (cf. Section 3.1.3), the criterion applies to all pair interactions $\phi(r)$ which decay sufficiently fast to zero with $r \to 0$, such that they are integrable and their Fourier transforms exist. Depending on the functional behaviour of the Fourier transform, $\tilde{\phi}(q)$, of the pair potential as a function of the wavenumber q, two possible scenarios are encountered:
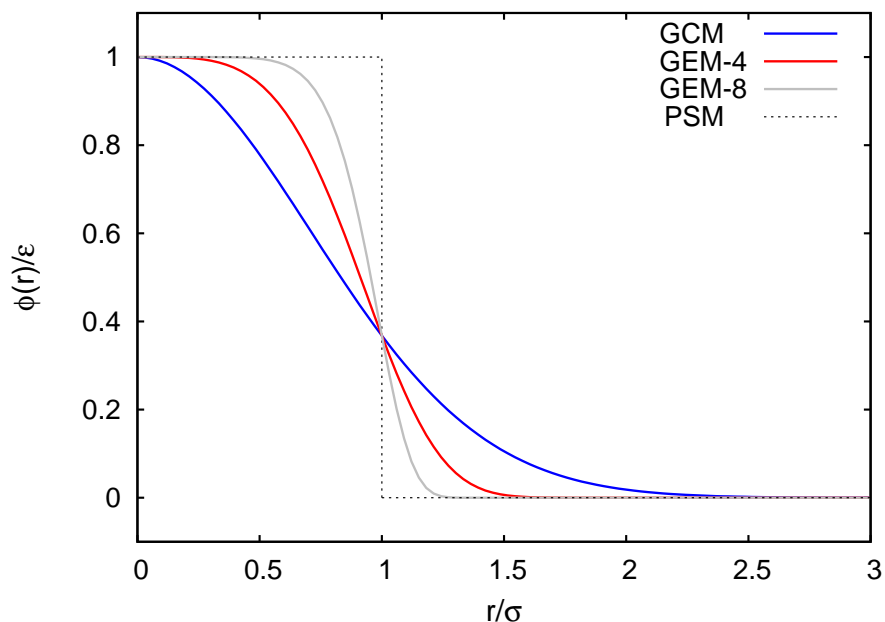
Figure 1.1: Four members of the GEM-n class. The GCM ($n = 2$), the GEM-4 and GEM-8, and the PSM ($n = \infty$).
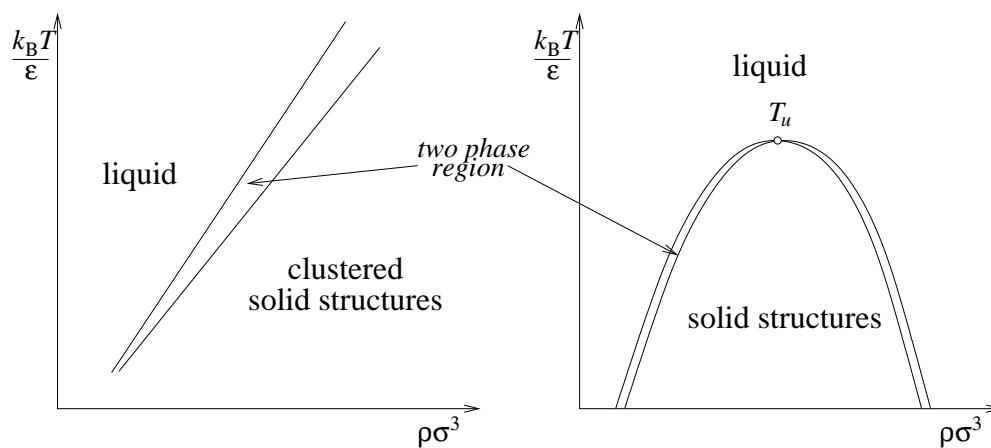
Figure 1.2: A sketch of the topology of the phase diagrams of the PSM (left) and the GCM (right). The PSM forms a cluster crystal with multiply occupied lattice sites at all temperatures, whereas the GCM displays re-entrant melting below an upper freezing temperature T_{u} for high densities. The figure is taken from [9], Chapter 2.2.

- Interactions for which the Fourier transform is non-negative for all possible values of q, $\tilde{\phi}(q) \geq 0 \; \forall q$, will exhibit re-entrant melting. They are said to belong to the Q^+ class.

- If, on the other hand, $\tilde{\phi}(q)$ oscillates, i.e. takes negative values for certain wave numbers q, the system is expected to show clustering. Accordingly, the corresponding potentials $\phi(r)$ are members of the so-called $Q^{\pm}$ class.

With these conditions at hand, we conclude that the GCM belongs to the Q^+ class, whereas the PSM is a representative of the $Q^{\pm}$ category. Conveniently, in practice the Fourier transform $\tilde{\phi}(q)$ does not need to be evaluated explicitly. From a relation [2], which links the second derivative of the pair potential at $r = 0$, $\phi''(r = 0)$, to $\tilde{\phi}(q)$,

$$\phi''(r = 0) = -\frac{1}{6\pi^2} \int\limits_0^\infty \mathrm{d}q \, q^4 \, \tilde{\phi}(q), \tag{1.3}$$

it becomes clear that, if $\phi''(r = 0) \geq 0$, then $\tilde{\phi}(q)$ must necessarily have negative parts and thus $\phi(r)$ is a $Q^{\pm}$ potential.

Returning to the GEM-n interaction class, the second derivative of $\phi(r)$, given in eq. (1.1), is

$$\phi''(r) = \frac{\varepsilon n}{\sigma^2} \, e^{-(r/\sigma)^n} \left[n \left(\frac{r}{\sigma}\right)^{2(n-1)} - (n-1) \left(\frac{r}{\sigma}\right)^{n-2} \right]. \tag{1.4}$$

This expression reveals that the transition from the Q^+ to the $Q^{\pm}$ class precisely occurs at $n = 2$. For sufficiently high densities, all systems interacting via a GEM-n, $n > 2$, potential will form cluster crystals. For the remainder of this work we will focus our attention on the properties of these clustering systems.

1.1.3 Amphiphilic dendrimers

In spite of the elegantly formulated criterion on which the clustering phenomenon is based, one may well question the physical reality of bounded ultrasoft potentials. A satisfactory legitimating answer to this question was proposed by Mladek *et al.* who focused on a special class of macromolecules in their recent work [9, 4]. In an effort to tailor substances on the computer that show clustering they found *amphiphilic dendrimers* (see Fig. 1.3) to display exactly the form of $Q^{\pm}$ interactions. Dendrimers are synthetic macromolecules which are characterised by a high degree of monodispersity in both size and shape, and a well-defined, highly-branched internal structure [9]. In [1, 5] evidence was given that the behaviour of dendrimers can be treated on the
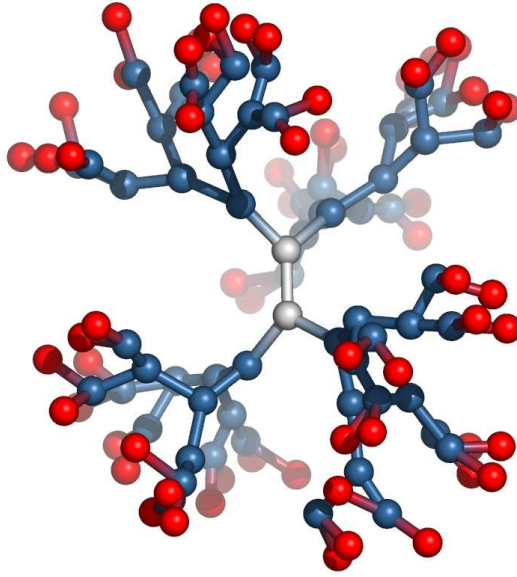
Figure 1.3: Schematic representation of a 5th generation dendrimer in dense-shell configuration. The figure is taken from [9], Chapter 7.1.

level of effective interactions. After a coarse-graining procedure in which the degrees of freedom of the constituent monomers are averaged out, dendrimers can be regarded as point particles interacting by means of a pair potential.

In [4, 9] amphiphilic dendrimers were designed in a "computer synthesis", in which effective interactions of model molecule structures were calculated with the aid of the Monte Carlo (MC) method (cf. Section 2.2). By assembling such macromolecule models with a solvophobic core and a solvophilic shell group, the authors aimed at a structure that is more open than the one of simple dendrimers, and that involves a stronger segregation between outer and inner monomers. In this way, the shape of a GEM-n potential for $n > 2$, consisting of a flat core region and a steep decay for larger separations, could be reasonably well reproduced. Finally, a guideline was presented with the ambition to encourage the synthesis of such clustering dendrimers in the lab, as the experimental realisation of clustering systems is still missing.

1.2 Ordered cluster phases

Since the main aim of this work is to characterise the dynamics of cluster *crystals*, we only provide the theoretical background for the description of *solid* clustering phases. As far as the fluid phase is concerned, the reader is referred to the original works [6, 9, 11], where detailed explanations on *integral equation theories*, the formalism employed for this phase, are given.

1.2.1   Genetic algorithms

When dealing with ordered cluster phases one first has to determine the lattice structure in which the system freezes. From the outset, in principle many crystal structures are suitable candidates and it is not clear a priori which one will be preferred in a clustering system. To identify suitable crystal structures in an unbiased fashion a search tool based on ideas of *genetic algorithms* (GA) [12] was developed, i.e. a numerical tool that is able to search among basically all possible lattices for the equilibrium structure. As the energetically most favourable ordered structures at $T = 0$, the body-centred cubic (bcc) and the face-centred cubic (fcc) phase were obtained [13, 14, 15] and considered as candidates for the phase diagram at finite temperatures.

1.2.2   Density functional theory

As a formalism appropriate for the description of ordered cluster phases at finite temperatures classical *density functional theory* (DFT) [16] was introduced. DFT allows to determine the free energy F as a functional $\mathcal{F}[\varrho]$ of the one-particle density

$$\varrho(\boldsymbol{r}) = \left\langle \sum_{i=1}^{N} \delta(\boldsymbol{r} - \boldsymbol{r}_i) \right\rangle. \tag{1.5}$$

According to the formalism of DFT the equilibrium one-particle density is obtained by a variational requirement on $\mathcal{F}[\varrho]$. $\mathcal{F}$ can be split up as follows:

$$\mathcal{F}[\varrho] = \mathcal{F}_{\mathrm{id}}[\varrho] + \mathcal{F}_{\mathrm{ex}}[\varrho], \tag{1.6}$$

where the ideal part $\mathcal{F}_{\mathrm{id}}[\varrho]$ is given by

$$\mathcal{F}_{\mathrm{id}}[\varrho] = k_{\mathrm{B}}T \int \mathrm{d}\boldsymbol{r}\, \varrho(\boldsymbol{r}) \left\{ \log[\varrho(\boldsymbol{r})\Lambda^3] - 1 \right\}, \tag{1.7}$$

with Λ being the de Broglie wavelength, see Appendix A.1, eq. (A.3). Following the considerations of [2] a mean-field format for the excess free energy functional, $\mathcal{F}_{\mathrm{ex}}[\varrho]$, was used,

$$\mathcal{F}_{\mathrm{ex}}[\varrho] = \frac{1}{2} \iint \mathrm{d}\boldsymbol{r}_1 \mathrm{d}\boldsymbol{r}_2\, \varrho(\boldsymbol{r}_1)\varrho(\boldsymbol{r}_2)\, \phi(|\boldsymbol{r}_1 - \boldsymbol{r}_2|). \tag{1.8}$$

A clustering system is characterised by the multiple occupancy of lattice sites by overlapping particles. Contrary to conventional crystals of single occupancy, the number of particles, N, and the number of lattice sites, N_{c}, do not coincide, which necessitates the introduction of the occupation variable (or, cluster size) n_{c},

$$n_{\mathrm{c}} = \frac{N}{N_{\mathrm{c}}}. \tag{1.9}$$

To describe a cluster crystal in the framework of DFT, clusters are set up in a periodic arrangement. For the cluster-density a Gaussian density profile is assumed,

$$\varrho_{\mathrm{cl}}(\boldsymbol{r}) = n_{\mathrm{c}} \left(\frac{\alpha}{\pi}\right)^{3/2} e^{-\alpha \boldsymbol{r}^2}, \tag{1.10}$$

which is localised at the lattice sites, $\{\boldsymbol{R}\}$, and normalised to n_{c} [2]. $\varrho_{\mathrm{cl}}(\boldsymbol{r})$ is used to parametrise the inhomogeneous one-particle density field $\varrho(\boldsymbol{r})$,

$$\varrho(\boldsymbol{r}) = \sum_{\{\boldsymbol{R}\}} \varrho_{\mathrm{cl}}(\boldsymbol{r} - \boldsymbol{R}) = n_{\mathrm{c}} \left(\frac{\alpha}{\pi}\right)^{3/2} \sum_{\{\boldsymbol{R}\}} e^{-\alpha(\boldsymbol{r}-\boldsymbol{R})^2}. \tag{1.11}$$

In this ansatz $\varrho(\boldsymbol{r})$ is uniquely determined by the localisation parameter α and the occupation number n_{c}. The equilibrium values of α and n_{c} are obtained by minimising the functional $\mathcal{F}[\varrho]$, given by eqs. (1.6) to (1.8), with respect to both α and n_{c} at fixed ϱ and T. Upon inserting the ansatz (1.11) into eqs. (1.6) to (1.8) the free energy functional per particle, $\mathcal{F}[\varrho]/N$, reduces to a function $f = f(n_{\mathrm{c}}, \alpha)$ which can be split into and ideal, an inter-, and an intra-cluster contribution,

$$f(n_{\mathrm{c}}, \alpha) = f_{\mathrm{id}}(n_{\mathrm{c}}, \alpha) + f_{\mathrm{inter}}(n_{\mathrm{c}}, \alpha) + f_{\mathrm{intra}}(n_{\mathrm{c}}, \alpha). \tag{1.12}$$

The respective expressions are given by

$$f_{\mathrm{id}}(n_{\mathrm{c}}, \alpha) = k_{\mathrm{B}}T \left[\log n_{\mathrm{c}} + 3/2 \log(\alpha \sigma^2/\pi) - 5/2 + 3 \log(\Lambda/\sigma)\right], \tag{1.13}$$

$$f_{\mathrm{inter}}(n_{\mathrm{c}}, \alpha) = n_{\mathrm{c}} \sqrt{\frac{\alpha}{8\pi}} \sum_{\boldsymbol{R} \neq 0} \int_0^\infty \mathrm{d}r \, \frac{r}{R} \left[e^{-\alpha(r-R)^2/2} - e^{-\alpha(r+R)^2/2}\right] \phi(r), \tag{1.14}$$

$$f_{\mathrm{intra}}(n_{\mathrm{c}}, \alpha) = (n_{\mathrm{c}} - 1) \sqrt{\frac{\alpha^3}{2\pi}} \int_0^\infty \mathrm{d}r \, r^2 \, e^{-\alpha r^2/2} \phi(r). \tag{1.15}$$

A detailed study of these terms provides the key to understand how clusters can form in a system despite the complete absence of attraction. In Fig. 1.4 these contributions are drawn for fixed α as a function of n_{c}. f_{inter}, corresponding to the interaction between clusters, drops monotonically with n_{c}: upon increasing n_{c}, the lattice spacings are enlarged and close contacts to nearest-neighbour clusters become less probable. The self-interaction within the cluster, expressed by f_{intra}, and the entropy loss due to particle aggregation, expressed by the logarithmic dependence $\log n_{\mathrm{c}}$ in f_{id}, on the other hand, disfavour the formation of clusters [9]. Nevertheless, the interplay of
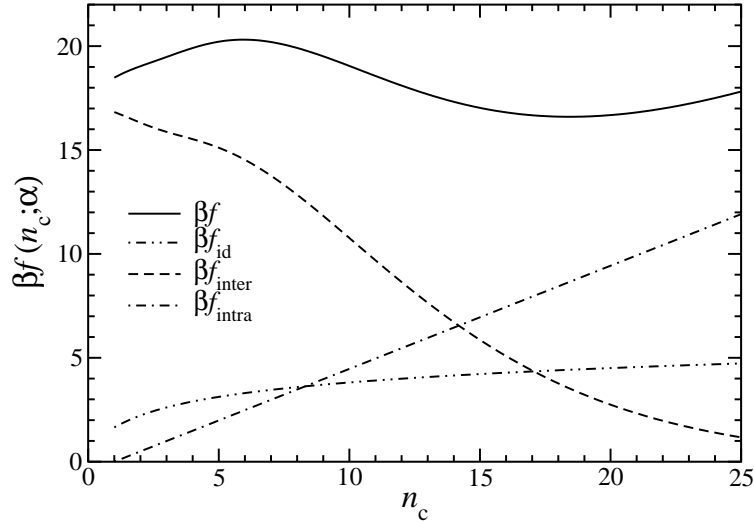
Figure 1.4: Minimising the free energy per particle, $f(n_c, \alpha)$, with respect to n_c at fixed α for an fcc crystal formed in a GEM-4 system at $T = 1.0$ and $\varrho = 9.0$. The contributions to $\beta f(n_c, \alpha)$ of the three parts of $f(n_c, \alpha)$, the ideal, the inter-, and the intra-cluster part, are shown. The inverse temperature β is defined in Appendix A.1, eq. (A.2). The figure is taken from [9], Chapter 7.3.

these competing contributions leads to an overall $f(n_c, \alpha)$ with a global minimum at finite n_c, which represents the equilibrium free energy per particle of a mechanically stable cluster crystal. This provides evidence that the clustering scenario indeed minimises the crystal's free energy [2].

1.3 Characteristic features of GEM-4 cluster crystals

The theoretical predictions of DFT on the properties of a clustering system were put to the test by comparing them to the results of MC simulations [17]. In these simulations cluster crystal equilibrium configurations were generated by minimising the free energy in a procedure based on *thermodynamic integration* [18, 19]. For the example of one of the members of the GEM-n class, the GEM-4 potential, the DFT-results for the fluid-bcc and bcc-fcc transition lines were proven to be in excellent agreement with the simulation data. Both theory and computer experiment reveal astonishing features of the behaviour of cluster crystals [3, 15, 20, 21, 22, 23], which shall be summarised in the following.
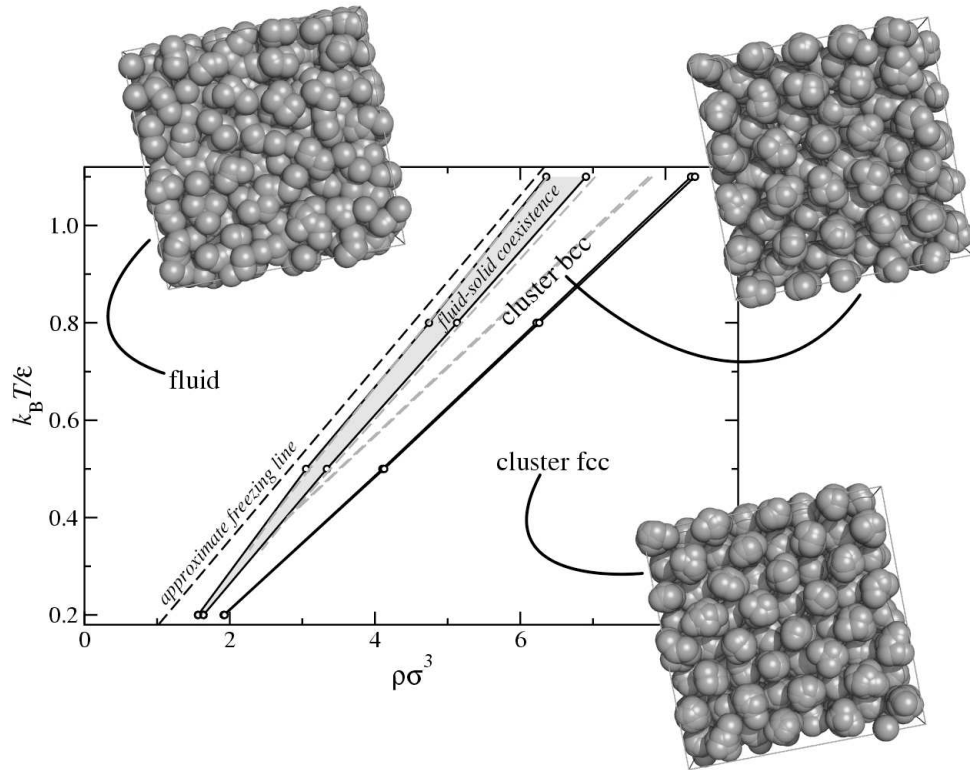
Figure 1.5: Phase diagram of the GEM-4 system. The black circles are phase coexistence points obtained from MC simulations. The dashed grey lines show the theoretical predictions on the fluid-bcc and bcc-fcc transition lines. Three simulation snapshots for the fluid, the bcc and the fcc phase are displayed as well. The particle diameters are arbitrarily scaled to enhance visibility. The figure is taken from [9], Chapter 7.3.

1.3.1   Phase diagram

In Fig. 1.5 the phase diagram of a GEM-4 system, determined in a joint effort of GA, DFT, and MC simulations, is shown. The fluid phase may be described as a mixture of strongly aspherical clusters with a vast variation of cluster size, n_c. When compressing the system at constant T a first-order transition into a cluster bcc phase is encountered, which occupies a wedge-like shape in the phase diagram [15]. Upon further increase in density the system undergoes a structural transition to an fcc phase. The thermodynamically more favourable fcc crystal remains stable for all higher densities, covering the overwhelming part of the phase diagram. The circumstance that the cluster crystal takes on a bcc and fcc structure points to the fact that effective cluster-cluster interactions are harshly repulsive. In fact, this is a typical property of systems that freeze into fcc and bcc, such as Lennard-Jones systems for example.

1.3.2 Density-independent lattice constant

From the DFT predictions and the determination of the equilibrium site occupancy number, n_c, in MC simulations [15], n_c turns out to scale linearly with density. A rigorous theoretical explanation of this effect has been provided in [2]. In that work, it was shown that, at the freezing transition, a clustering system adapts its lattice constant a in such a way that the modulus of its shortest reciprocal lattice vector coincides with the wave number q_*; q_* denotes the position of the first negative minimum of the Fourier transform of the potential, $\tilde{\phi}(q)$. The location of the first minimum in the Fourier transform solely depends on the functional form of the potential $\phi(r)$, and not on density or temperature. Thus, the density-independent lattice constant a is dictated by q_* alone,

$$a \propto \frac{1}{q_*}. \tag{1.16}$$

The linear dependence of n_c on ϱ is given by

$$n_c = \frac{8\sqrt{2}\pi^3}{q_*^3}\,\varrho. \tag{1.17}$$

The above results entail far-reaching implications for the behaviour of clustering systems. In striking contrast to systems of harshly repulsive interaction, a GEM-4 crystal does not react to an increase in density by tightening its lattice spacing [15]. Instead, the system follows the strategy of optimising its lattice constant with respect to q_* by adjusting the number of particles per lattice site n_c. This also means that any new particles that are inserted in the crystal will preferably join existing clusters, thereby maintaining the underlying crystal structure or, equally, the volume of a primitive unit cell.

1.3.3 Bulk modulus

The above considerations in mind, it is not surprising that the elastic behaviour of the GEM-4 system is strongly influenced by the fact that the lattice constant does not change with density.

The bulk modulus, B, measures the resistance of a substance to compression. It is defined as

$$B = -V\left(\frac{\partial P}{\partial V}\right)_{N,T} \tag{1.18}$$

where P is the pressure exerted on the system. For a clustering system eq. (1.18) has to be reconsidered and adopted to the specific feature that, unlike in single-occupancy crystals, the number of lattice sites, N_c, need not be equal to the number

of particles, N, anymore. In [3, 17] it has been shown that in this case the bulk modulus takes the form

$$
\begin{aligned}
B &= -V \left(\frac{\partial P}{\partial V} \right)_{N,T,N_c} - V \left(\frac{\partial P}{\partial N_c} \right)_{N,T,V} \left(\frac{\partial N_c}{\partial V} \right)_{N,T} \\
&= B_{\mathrm{vir}} - B_{\mathrm{del}},
\end{aligned} \tag{1.19}
$$

where the right-hand side is evaluated for an equilibrium state point, corresponding to a minimum of the free energy F. From eq. (1.19) we see that there are now two mechanisms by which the system can react upon an increase in density (see Fig. 1.6). The first term, B_{vir}, reflects the ordinary response of a system to compression: when reducing the volume particles move closer together, which leads to affine shrinking of the crystal [17]. In the second mechanism, expressed by B_{del}, lattice sites in the system can be deleted; the corresponding clusters are dissolved, their particles redistribute onto the remaining lattice sites. By evaluating the magnitude of the two contributions to the bulk modulus, it was found out that the latter correction to B, B_{del}, is far from being negligible. For the GEM-4 potential B_{del} results in a reduction of the original value of B of over 40 percent, which suggests that the deletion of lattice sites considerably weakens the system's response to compression [3].

The compression-induced rearrangement of particles is another aspect of the phenomenon of microscopic "self-assembly", which is one of the main features of cluster crystals.

1.3.4 Cluster crystal dynamics

Regarding the dynamic properties of cluster crystals, recently two main aspects have been put in the centre of attention. In [2, 15] two different types of particle excitation in a cluster crystal have been anticipated – vibration and particle hopping. Considering a cluster crystal as a Bravais lattice with an n_c-point basis, its phonon spectrum has been predicted to consist of three acoustic branches and $3(n_c - 1)$ optical branches [24], corresponding to collective and individual motion of particles in the system.

The second type of excitation refers to the possibility that, through an activated hopping mechanism, particles hop between lattice sites, while the underlying crystal structure remains intact. This represents another important feature of cluster crystals. Such crystals are diffusive on the single-particle level, allowing mass transport, however arrested on the collective level and thus rigid as a conventional solid [9]. In [23] it was found out that the incessant hopping processes result in a long-time diffusivity D which solely depends on the ratio ϱ/T.
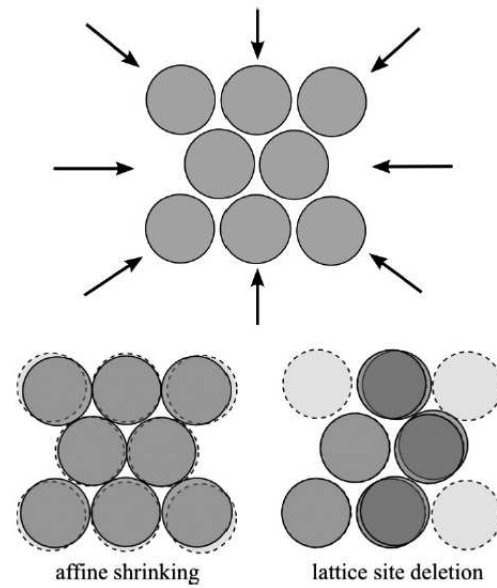
Figure 1.6: Schematic sketch of the behaviour of a cluster crystal upon uniform compression. In contrast to conventional single-occupancy crystals, diminishing the lattice constant a is not the only possible response. Additionally, in a second mechanism, lattice sites are deleted by redistributing the corresponding particles to neighbouring clusters. The figure is taken from [17].

For the present work, the recent investigations of vibrations and diffusion in cluster crystals are taken as a starting point and motivation to further explore the features of the phonon spectrum, on the one hand, and to characterise the hopping mechanism in more detail, on the other hand. The respective results that are obtained will be extensively discussed in Chapter 4 and 5.

Chapter 2

Molecular simulations

In the past decades molecular simulations have become an indispensable numerical tool in numerous fields of scientific research. From the point of view of statistical mechanics, molecular simulations are capable of providing essentially exact results where problems lack rigorous analytical solutions. In addition, they allow to test theoretical models at physical conditions that might pass experimental limitations, e.g. high pressure or temperature. Making it possible to simulate the macroscopic properties of interest from microscopic details of a system in a controlled and reliable fashion, they play a crucial role in intermediating between theory and real experiments.

In Section 2.1 we present the basic ideas of molecular simulation, which are common to both molecular dynamics and Monte Carlo simulations of bulk systems. In Section 2.2 we will deal with the Monte Carlo (MC) method, an advanced technique commonly used to evaluate ensemble averages of static system properties. Molecular dynamics (MD) simulations, extensively employed in our work to characterise the dynamic behaviour of cluster crystals, will be treated in Section 2.3.

2.1 Basic concepts of molecular simulations

2.1.1 Interaction model

Before any kind of molecular simulation can be carried out, a decision has to be taken on the type of *interaction model* that suitably represents the system under consideration.

In general, any potential energy function $\mathcal{U}$ is a many-body function $\mathcal{U}(\{\boldsymbol{r}^N\})$ dependent on all N particle positions $\{\boldsymbol{r}^N\} = (\boldsymbol{r}_1, \boldsymbol{r}_2, ..., \boldsymbol{r}_N)$. Usually, it is assumed that $\mathcal{U}$ can be split up into a sum of terms consisting of single-, pair-, triplet-, etc.

contributions to the potential energy, i.e.

$$\mathcal{U}(\{\boldsymbol{r}^N\}) = \sum_i \phi_1(\boldsymbol{r}_i) + \sum_i \sum_{j>i} \phi_2(\boldsymbol{r}_i, \boldsymbol{r}_j) + \sum_i \sum_{j>i} \sum_{k>j>i} \phi_3(\boldsymbol{r}_i, \boldsymbol{r}_j, \boldsymbol{r}_k) + \dots \quad (2.1)$$

Here, we implicitly assume that all particles are of the same kind ("species") and interact via the same potential. In the above expression the first term $\phi_1(\boldsymbol{r}_i)$ corresponds to an external potential, such as container walls or an external field imposed on the system. The second term – in general the most important one – is the *pair potential* $\phi_2(\boldsymbol{r}_i, \boldsymbol{r}_j)$, which we assume to depend only on the pair separation, $r_{ij} = |\boldsymbol{r}_i - \boldsymbol{r}_j|$, hence $\phi_2(\boldsymbol{r}_i, \boldsymbol{r}_j) = \phi_2(r_{ij})$. The third term in eq. (2.1), $\phi_3(\boldsymbol{r}_i, \boldsymbol{r}_j, \boldsymbol{r}_k)$, is then the first one taking into account directional interactions, as it involves the relative positions of a triplet of interacting particles.

In many computer simulations, however, many-body contributions to the potential are either ignored or intentionally not considered,[1] since any calculation of interactions between three or more particles is very time-consuming. Dropping the first term in eq. (2.1) assuming that there is no external interaction, the full expansion of the potential energy is then approximated by

$$\mathcal{U}(\{\boldsymbol{r}^N\}) = \sum_i \sum_{j>i} \phi_2(r_{ij}). \qquad (2.2)$$

This expression represents the class of interactions, i.e. *pair* interactions, which will be used throughout this work.

2.1.2   Periodic boundary conditions

The main restriction on what we can realistically expect of a molecular simulation is of technical rather than physical nature. Above all, the size of any system we simulate is limited by a reasonable length of the time span needed for computation on present-day computers. Consequently, the typical system size is very small compared to macroscopic systems. The latter usually consist of a number of particles, N, of the order $N \approx 10^{23}$, whereas in MD simulations of an Argon-like Lennard-Jones fluid, for instance, N ranges from 10^3 to 10^5 for simulated times scales of the order of μs. Additionally, for a system contained in a box of cubic shape the fraction of particles located at its faces is proportional to $N^{-1/3}$. For example, for $N = 1000$, 488 particles are located on the surface of such a cubic arrangement. Since these particles are exposed to a very different surrounding than particles closer to the centre of the box, the influence of surface effects will be drastic. Thus, if we are

---

[1]This is a very common and justified approach if the shape of the particles of the system is very close or equal to a sphere. The most frequently used Lennard-Jones or the GEM-4 potential to be treated in this work apply to such cases by virtue of their spherically symmetric form.
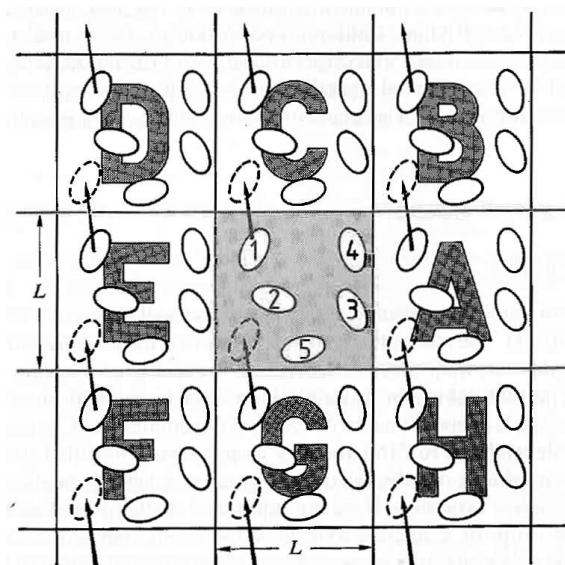
Figure 2.1: A two-dimensional system with periodic boundary conditions. The system is effectively infinite. As a particle leaves the system, i.e. the central simulation box, by crossing a boundary (see arrows), its image particle enters the cell on the opposite edge. The figure is taken from [25], Chapter 1.5.

interested in the bulk properties of a system we have to find a way to minimise these surface effects.

A solution to this problem is provided by the use of *periodic boundary conditions* (PBC): that is, we surround the central simulation box by an infinite number of replica of this box, thereby filling the entire space. By creating an effectively infinite lattice of boxes we remove any kind of surface effect, since we imitate in this way the presence of an infinite bulk. This situation is illustrated for a two-dimensional system in Fig. 2.1. Around the central cell its first 8 *periodic images* are arranged, labelled in an arbitrary manner. If a particle (say, particle 1) leaves the central box by crossing a boundary on one edge, its periodic image particle enters the cell on the opposite side, the absolute number of particles being conserved in this way.[2]

Even though removal of surface effects is achieved by the implementation of PBC, it remains to be discussed if the properties of a system of small size are representative of its macroscopic counterpart. This leads to the question of *finite size effects*. Not quite surprisingly, PBC do not enable us to scale down the system to arbitrarily small sizes. Even though PBC allow to mimic the behaviour of a bulk system, unexpected artefacts might be introduced. These may lead, for example, to correlation functions (such as the radial distribution function $g(r)$) between spherical particles that are

---

[2]In a sense, the topology of such a system is equal to that of the surface of a three-dimensional torus, which appears to be infinite from the point of view of someone located on this manifold.

not entirely radial [26]. Luckily, major finite size effects can in general be avoided easily by choosing a sufficiently large system; typically, some hundreds of particles are enough. In practice the actual choice of the system size will also depend on the potential range and the phenomena under investigation.

Still, some more intricate artefacts due to PBC and finite size may remain. For instance, density fluctuations can interfere with themselves giving rise to artificial travelling sound waves [27]. Moreover, any fluctuations of wavelength larger than L are inhibited, limiting the validity of all wave-vector dependent quantities computed from molecular simulation data. These problems can only be overcome by a thorough analysis in which finite size effects for different system sizes are assessed. Consequently, the properties calculated from the finite system can be extrapolated to the macroscopic system [25].

A final remark concerns the actual shape of the simulation box. In principle, any space-filling geometrical object can be taken up as an elementary cell. Nevertheless, for the vast majority of cases one tends to keep things as simple as possible, which is the reason why we will from now on restrict all our considerations to the cubic cell.

2.1.3   Potential truncation and minimum image convention

Having introduced PBC we realise that, in principle, the calculation of the potential energy of a particle configuration requires to sum over an infinite number of pairs of particles, including those in the central box as well as in all periodic images. Obviously, this is an impossible task in practice. Two further approximations have to be included, which are known in literature as *potential truncation* and *minimum image convention* (MIC), the second of which was first used in simulation in [28].

Fortunately, for short-range interactions the contributions of the immediate neighbours of a particle to the potential energy represent by far the most dominant part. For this reason, by truncating the potential, $\phi(r)$[3], with a spherical cutoff $r_{\rm c} \leq L/2$,

$$\phi^{\rm tr}(r) = \begin{cases} \phi(r) & r \leq r_{\rm c} \\ 0 & r > r_{\rm c} \end{cases}, \tag{2.3}$$

we do not introduce a large error in the calculation of the potential energy, yet manage to reduce the number of neighbours of a tagged particle.

Using this approach it may still happen that the sphere around a particle (say, particle number 1) exceeds the central simulation cell (see Fig. 2.2). In this case, the MIC provides a rule to determine which particles, or image particles, are regarded as interaction partners of particle 1. A cube $\mathcal{C}$ of the same size as the simulation box

---

[3]The subscript "$_2$" of ϕ, still present in eq. (2.2) to denote ϕ as a pair potential, is dropped, since no interactions other than *pair* interactions are considered.
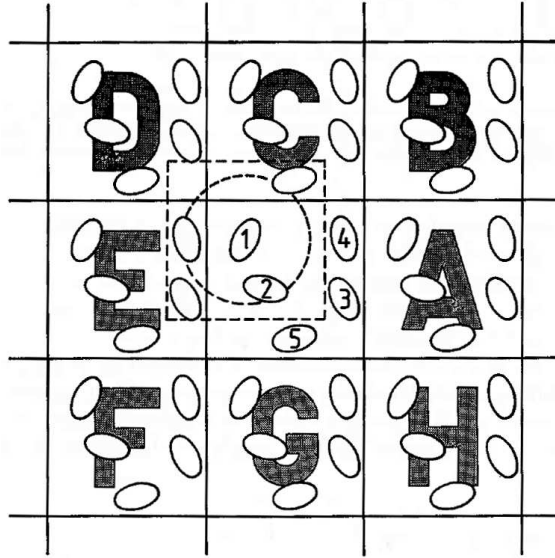
Figure 2.2: Minimum image convention and potential truncation. MIC: for the potential evaluation only neighbours within a box centred around a particle are chosen. Potential truncation: the number of neighbours is reduced by truncating the potential with a spherical cutoff in accordance with the interaction range. The figure is taken from [25], Chapter 1.5.

is introduced. $\mathcal{C}$ is centred around particle 1 that located in the central cell. For the calculation of the potential energy of this particle we take into account only those particles which are situated in $\mathcal{C}$, no matter whether these particles are located in the central simulation cell or in one of its periodic images (see again Fig. 2.2). In that way, the interaction of particle 1 with only those (image) particles is considered, from which it has the minimum distance; hence the name *minimum* image convention.

Note that the truncated potential, $\phi^{\mathrm{tr}}(r)$, should be still refined by using more sophisticated cutoff schemes that remove the discontinuity at r_{c} introduced in eq. (2.3). This can be achieved, for instance, with the help of a "cut and shift" prescription, a linear or quadratic correction to the potential, or a spline interpolation from $\phi(r_c)$ towards zero [25]. We want to stress, however, that smoothing the potential at r_{c} seems to be a dispensable provision, in particular when the cutoff radius, r_{c}, is chosen generously enough in the case of very short-ranged potentials. For example, the value of the GEM-4 potential at the cutoff radius that we use in our MD simulations is

$$\phi(r_{\mathrm{c}} = 2.5\,\sigma) \approx 10^{-17}\,\phi(r = 0). \tag{2.4}$$

2.1.4   Speeding up a molecular simulation

It is worth mentioning briefly some "tricks of the trade" of how to speed up a molecular simulation.

- **Tabulated potential.**
  The repeated direct evaluation of the potential can be avoided by setting up a look-up table. This table is constructed only once, at the beginning of the simulation, according to a grid ins space previously chosen. During a simulation the actual values of the potential and its derivatives at a given particle separation are then obtained by interpolating between two adjacent grid points.

- **Neighbour lists.**
  The basic concept of a *Verlet neighbour list* [18] may be sketched as follows: to avoid calculating the distances of each particle to all the others for each configuration, a list of neighbours in a sphere of radius r_l larger than r_c is created for every particle. This list enables us to keep book over those neighbouring particles for which an interaction is likely to occur. Its entries remain unchanged during a few simulation steps, which results in a considerable speed-up of the potential evaluation.

  The frequency by which the neighbour lists are updated can be fixed at the outset of the simulation. Preferably, this is done automatically by keeping track of the displacement of all particles: as soon as the sum of the largest particle displacements exceeds $r_l - r_c$ the lists are updated in the subsequent step.

- **Linked-cell lists.**
  As a refinement of the neighbour list method, or an alternative to it, the main simulation box is divided into subcubes of side length larger than r_c. The particles are assigned to these cells, a procedure that is repeated on a regular basis during the simulation. For the update of the neighbour lists only the distances to those particles are checked that are located in the surrounding cells.[4]
  The exact name of the method "*linked*-cell lists" stems from an implementational detail. Each cell is addressed by the identification number of one particle called "head-of-chain", which refers to the next particle in the same cell. In turn, all particles belonging to one cell are addressed, one after the other.

As mentioned before, the purpose of all these methods is to speed up a molecular simulation. In particular, by the joint use of neighbour lists and linked-cell lists, a substantial reduction of the computational effort for the interaction evaluation is achieved, i.e. from order $\mathcal{O}(N^2)$ to $\mathcal{O}(N)$.

---

[4]In *three* dimensions, each cell is surrounded by 27 neighbouring cells.

2.2 Monte Carlo simulations

The *Monte Carlo* method [18] is a sampling technique that is particularly suitable for high-dimensional systems treated in statistical physics. In its core part the method relies on a stochastic algorithm that explores the configurational part of phase space of such a system by repeated random sampling, making extensive use of random numbers. Going far beyond simulating multi-particle systems, Monte Carlo simulations apply to a large variety of other problems reaching from the computation of multi-dimensional definite integrals in mathematics over risk analysis in finance to the exploration of oil fields.

2.2.1 Conventional Monte Carlo simulations

In the canonical ensemble, the ensemble average of an arbitrary *static* quantity $\mathcal{A}(\boldsymbol{r}^N)$ is given by

$$\langle \mathcal{A} \rangle = \frac{\int \mathcal{A}(\boldsymbol{r}^N) \exp(-\beta \mathcal{U}(\boldsymbol{r}^N)) \, \mathrm{d}\boldsymbol{r}^N}{\int \exp(-\beta \mathcal{U}(\boldsymbol{r}^N)) \, \mathrm{d}\boldsymbol{r}^N}. \tag{2.5}$$

Here, the integration is carried out over the entire, $3N$-dimensional configuration space, and β is the inverse temperature defined in Appendix A.1, eq. (A.2). For practical purposes, eq. (2.5) is intractable, if we aim at its evaluation by (numerical) integration over a regular grid of points $\{\boldsymbol{r}^N\}$.

The basic solution to this problem suggested by the MC method is to take a random sampling of points instead of a regular array of points to calculate the average quantity $\langle \mathcal{A} \rangle$ [29]. In its simplest version, system configurations, represented by the positions and momenta of all particles, are created randomly and independently. For the calculation of the ensemble average of $\mathcal{A}$, eq. (2.5) is rewritten as

$$\langle \mathcal{A} \rangle = \sum_{\tau} \mathcal{A}_{\tau} \, p_{\tau}, \tag{2.6}$$

where $\mathcal{A}_{\tau}$ is the instantaneous value of $\mathcal{A}$ for a state τ, and p_{τ} the corresponding equilibrium occupation probability of τ, used as a weight. p_{τ} is given by

$$p_{\tau} = \frac{\exp(-\beta \mathcal{U}_{\tau})}{\int \exp(-\beta \mathcal{U}(\boldsymbol{r}^N)) \, \mathrm{d}\boldsymbol{r}^N} = \frac{e^{-\beta \mathcal{U}_{\tau}}}{Z_N}, \tag{2.7}$$

where Z_N is the configurational part of the canonical partition function. However, since many configurations will be of very low weight, i.e. they will only very weakly contribute to the ensemble average (2.6), this naive approach is computationally very inefficient.

Importance sampling

A more efficient technique is the one based on the concept of *importance sampling* [18, 25]. In this case, we attempt to select a subset of states according to their probability p_τ. The basic idea behind it is to sample many points in a region of space where the Boltzmann factor, $\frac{e^{-\beta \mathcal{U}_\tau}}{Z_N}$, is significantly large. If we succeed in sampling a series of states $\{\tau_1, \tau_2, ..., \tau_M\}$ according to their "importance", the sum in eq. (2.6) may be replaced by

$$\mathcal{A}_M = \sum_{i=1}^{M} \mathcal{A}_{\tau_i}, \tag{2.8}$$

Here, we do not have to include the probabilities p_τ anymore because they are considered implicitly by the way in which we generate the states. The value of $\mathcal{A}_M$ and the average $\langle \mathcal{A} \rangle$, calculated via eq. (2.5), coincide in the limit

$$\lim_{M \to \infty} \mathcal{A}_M = \langle \mathcal{A} \rangle. \tag{2.9}$$

Markov chains

To find a subset of states $\{\tau\}$ in configuration space that complies with the above concept, we make use of *time-homogeneous Markov chains* [18, 25]. Instead of randomly picking out configurations from the entire configuration space, we generate a new state ν of the system from a given state τ with probability $P(\tau \to \nu)$. These *transition* probabilities have to satisfy the following three criteria:

- $P(\tau \to \nu)$ do not vary with time,

- they only depend on the properties of the states τ and ν and not on any state that the system has visited in the past ("process without memory of the past"),

- the sum over the transition probabilities from a state τ to all possible states ν is equal to 1 (sum rule)

$$\sum_{\nu} P(\tau \to \nu) = 1, \tag{2.10}$$

  stating that the system has to end up in *some* state.

Additionally, if we want a Markov chain to produce a sequence of states that appear with the probabilities given in eq. (2.7), two further requirements have to be fulfilled:

- **ergodicity**, which means that each state of the system has to be reachable from any other state within a finite number of steps of the Markov chain (cf. also Section 3.1.1).

- **detailed balance**, expressed by the relation

$$p_\tau P(\tau \to \nu) = p_\nu P(\nu \to \tau), \qquad (2.11)$$

  by which is meant that a system must pass as likely from state τ to ν as, vice versa, from state ν to τ.

If all of the above conditions are satisfied, we will yield a set of M states from the Markov chain, distributed according to the Boltzmann probability distribution p_τ, and will be able to calculate a canonical ensemble average by eq. (2.8).

Metropolis Monte Carlo

So far, we have sketched the track that must be followed, if we want to employ the Monte Carlo method for the calculation of average system properties. What we seek for in the next step is an appropriate translation of the notion of a Markov chain into an algorithm that fulfils all of the aforementioned requirements. The most widespread realisation of such a procedure was suggested by Metropolis *et al.* [28] and is commonly referred to as *Metropolis Monte Carlo* method. The algorithm works as follows:

- From an arbitrary system state $\tau \,\hat{=}\, (\boldsymbol{r}_1, \boldsymbol{r}_2, ..., \boldsymbol{r}_N)$ a particle i is randomly chosen.

- A vector $\boldsymbol{\xi}_i$ is calculated, the components of which are uniformly distributed random numbers in the interval $[-1, 1]$. Particle i is shifted by $\Delta \cdot \boldsymbol{\xi}_i$,

$$\boldsymbol{r}_i \to \boldsymbol{r}_i' = \boldsymbol{r}_i + \Delta \boldsymbol{\xi}_i, \qquad (2.12)$$

  to obtain a new state $\nu \,\hat{=}\, (\boldsymbol{r}_1, ..., \boldsymbol{r}_i', ..., \boldsymbol{r}_N)$. Δ is the maximum allowed displacement, fixed at the outset of an MC simulation.

- The change in the potential energy, $\Delta \mathcal{U} = \mathcal{U}_\tau - \mathcal{U}_\nu$, that is induced by the particle move is calculated. If the particle displacement leads to a decrease in energy, i.e. $\Delta \mathcal{U} < 0$, then the new state ν is accepted. If, on the contrary, the potential energy is increased, i.e. $\Delta \mathcal{U} \geq 0$, the new state ν is accepted with a probability $e^{-\beta \Delta \mathcal{U}}$. In practice, another random number ξ' between 0 and 1 is chosen and compared to $e^{-\beta \Delta \mathcal{U}}$. If this number is smaller, state ν is accepted despite the energy decrease, otherwise state ν is rejected (see Fig. 2.3) and the next trial move is performed with another particle. Irrespective of whether the new state has been accepted or not, the system is considered to be in a new configuration; this is important for the production of states following the intended probability distribution, given by eq. (2.7).
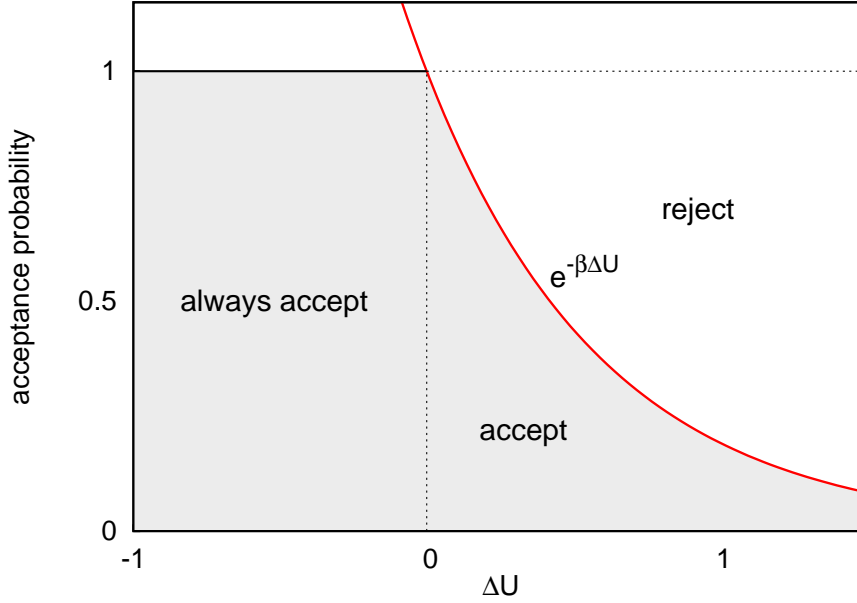
Figure 2.3: Metropolis Monte Carlo: a particle move that leads to a decrease in potential energy is always accepted. If, otherwise, the potential energy is increased by $\Delta\mathcal{U}$, the move is only accepted with probability $e^{-\beta\Delta\mathcal{U}}$.

This procedure is being repeated until the desired simulation length is attained. The "evolution" of the system corresponds to a random walk through a representative region of configuration space such that, from an average taken over all visited states, good estimates of the quantities of interest are obtained via eq. (2.8).

A final remark concerns the choice of the maximum allowed displacement Δ. According to [25], it should be fixed to a value that leads to an *average acceptance ratio* such that the rate of equilibration of system with respect to computational cost is optimised. The average acceptance ratio $\overline{a}$ is defined as

$$\overline{a} = \frac{1}{M} \sum_{i=1}^{M} \min\left[1, e^{-\beta\Delta\mathcal{U}_i}\right], \tag{2.13}$$

where M is again the number of sampled states. Typically, the values of $\overline{a}$ range between 30 and 50 percent.

2.2.2 Lattice Monte Carlo simulations

If we intend to perform long Monte Carlo simulations for systems of large size ($N > 10^3$), we must search for a means of speeding up our simulations even further, going beyond the speed-up techniques presented in Section 2.1. This is particularly important for the study of clustering systems, where we need a considerable amount

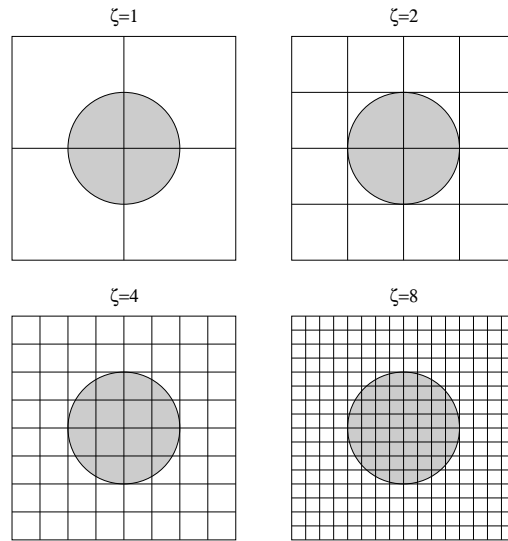Figure 2.4: Discretisation of a two-dimensional system in LMC simulations, illustrated for different values of ζ. The grid resolution (number of grid points per particle diameter) grows as ζ is increased. The figure is taken from [9], Chapter 4.5.

of particles to guarantee a sufficiently large number of clusters in our simulation volume. For this reason, we introduce the concept of *Lattice Monte Carlo* (LMC) simulations, a method originally suggested by Panagiotopoulos [30].

The key idea of LMC simulations is to transform a system where the particle coordinates are continuous quantities into a lattice model by discretising the particle positions to sites of a regular grid. The resolution of the grid is fixed by the choice of a lattice discretisation parameter ζ which specifies the number of grid sites g per particle diameter σ,

$$\zeta = \frac{g}{\sigma}. \tag{2.14}$$

In Fig. 2.4 the grid resolution for different values of ζ is illustrated schematically for a two-dimensional system. To ensure that periodic boundary conditions are respected by the discretisation, ζ must be chosen such that $L \times \zeta$ is an integer; nevertheless, L and ζ may take rational values individually.

The main increase in computational efficiency in LMC simulations results from the discretisation of the particle positions, through which the number of possible distances between two particles of the system is limited. As a consequence, one needs to calculate the interaction energies for all of these separations only once, at the beginning of a simulation, and tabulate them in a look-up table for further use during a simulation run. Depending on the actual shape of the potential under consideration, this brings about an appreciable speed-up for the simulations: for

instance, for the GEM-4 potential, a speed-up factor of about 20 with respect to the conventional MC scheme has been reported in [9].

The price to be paid for the gain in CPU-time is a reduction in numerical accuracy of our calculation. By discretising the available positions in a box, an artificial substructure is imposed on the system which affects structural quantities as well as ensemble averages of observables. Yet, lattice discretisation artefacts are expected to decrease as ζ is increased [30]. For the GEM-4 potential a value of $\zeta = 32$ is reported to be sufficiently large to reproduce the results of standard continuous MC simulations [31, 32].

2.2.3   Auxiliary "Widom-like" MC moves

An additional modification to the LMC simulation technique developed so far can be made, if we want to enhance the equilibration of systems characterised by slow dynamics. This refers in particular to cluster crystals at low temperatures. In our work we opt to employ LMC simulations in a region of the GEM-4 phase diagram (cf. Fig. 1.5), which includes the non-diffusive regime. In this region, it is not possible to reach the equilibrium distribution of cluster sizes (cf. Fig. 4.2), within an MD simulation of reasonable length, as the equilibrating process, i.e. particle hopping between lattice sites, is very slow. In a cluster crystal the potential barriers between lattice sites can attain considerable heights (cf. Section 5.2). That is why configurations where a particle leaves a cluster and hops to a neighbouring lattice site are states of increased energy, compared to a situation in which the same particle stays in its home cluster. Therefore, for low temperatures, such configurations are very likely to be rejected in a standard Metropolis MC algorithm.

To circumvent this problem, we introduce an additional type of MC trial move: if from time to time (say, once out of 100 steps) we allow a particle to be displaced by an arbitrary distance, regardless of the prescribed value of Δ in eq. (2.12), this particle will be shifted directly to another cluster site with a certain probability. In this way, we enable the system to explore a larger region of configuration space. Concomitantly, it will tend much faster to its equilibrium cluster size distribution.

One may call this kind of auxiliary move a "Widom-like" move, due to its similarity to the Widom insertion method [33], in which a particle is (re-)inserted into a system at a random position. It is important to note that, as artificial as Widom-like moves may seem at first sight, they, however, do not lead to unphysical results as long as the requirements formulated for Markov processes are satisfied (cf. Section 2.2.1).

2.3 Molecular dynamics simulations

In contrast to MC simulations, in a *molecular dynamics* simulation we intend to generate a sequence of configurations according to the inherent time-evolution of a system. In many respects an MD simulation is very similar to a real experiment. It serves us to measure not only static but also time-dependent properties of a system, characterising the interesting *dynamics* of the underlying physical processes.

In the following two subsections we will present the integration algorithm for the solution of the equations of motion and will point out the difference between equilibration and production MD simulation runs.

2.3.1 NVE simulations

We first look at an *isolated*, classical system. Its volume is kept constant, the particle number and the energy are conserved. An MD simulation subject to these constraints will sample from the *microcanonical* ensemble.

Equations of motion

The dynamics of the system is governed by the Hamiltonian

$$\mathcal{H} = \sum_{i=1}^{N} \frac{\boldsymbol{p}_i^2}{2m_i} + \mathcal{U}(\boldsymbol{r}^N). \tag{2.15}$$

Particle trajectories are obtained from the solution of Hamilton's equations of motion

$$\begin{cases} \dot{\boldsymbol{r}}_i = \boldsymbol{p}_i \, / \, m_i \\ \dot{\boldsymbol{p}}_i = -\nabla_i \mathcal{U}(\boldsymbol{r}^N) = \boldsymbol{f}_i \end{cases} \tag{2.16}$$

with suitable initial conditions, $(\boldsymbol{r}_i(t = 0), \boldsymbol{p}_i(t = 0))$. In eq. (2.16) $\dot{\boldsymbol{r}}_i$ and $\dot{\boldsymbol{p}}_i$ are the time derivatives of the positions and momenta of particle i and $\boldsymbol{f}_i$ is the force exerted on the same particle by all the others.

Integration Scheme

The core part of an MD simulation is its integration algorithm. It discretises the equations of motion, eqs. (2.16), and solves them numerically via an iterative procedure. Starting from the set of positions and momenta of all particles at a time t, the algorithm calculates the positions and momenta at a later time $t + \delta t$, with δt being the time increment.

The expectations for such an integration scheme are the following:

- it should produce a highly accurate numerical solution of the equations of motion, for the time range on which we investigate time-dependent correlations,

- whereas for the calculation of time-*in*dependent (static) macroscopic averages, in the long term, it is sufficient to sample from a statistical ensemble such that the corresponding phase space density is approximated at the best.

These requirements impose further desirable properties on the algorithm:

- a large time step δt, which at the same time maintains a high degree of accuracy, is preferred,

- energy conservation on a very high level (see below) is essential,

- conceptual simplicity of the algorithm is an asset.

The *Verlet integration algorithm* [34] satisfies all of these requirements. The iterative algorithm is based on the following equation for the particle positions:

$$\boldsymbol{r}_i(t + \delta t) = 2\boldsymbol{r}_i(t) - \boldsymbol{r}_i(t - \delta t) + \frac{\boldsymbol{f}_i(t)}{m_i}\,\delta t^2. \tag{2.17}$$

This expression is easily obtained by adding two second-order Taylor expansions about $\boldsymbol{r}_i(t)$,

$$\boldsymbol{r}_i(t + \delta t) = \boldsymbol{r}_i(t) + \frac{\boldsymbol{p}_i(t)}{m_i}\,\delta t + \frac{\boldsymbol{f}_i(t)}{2m_i}\,\delta t^2,$$
$$\boldsymbol{r}_i(t - \delta t) = \boldsymbol{r}_i(t) - \frac{\boldsymbol{p}_i(t)}{m_i}\,\delta t + \frac{\boldsymbol{f}_i(t)}{2m_i}\,\delta t^2. \tag{2.18}$$

From eq. (2.18) we see that in this integration scheme the momenta are not needed to compute the trajectories. The $\boldsymbol{p}_i(t)$ are given separately by the difference quotient

$$\frac{\boldsymbol{p}_i(t)}{m_i} = \frac{\boldsymbol{r}(t + \delta t) - \boldsymbol{r}(t - \delta t)}{2\delta t}. \tag{2.19}$$

Eq. (2.17) is correct up to $\mathcal{O}(\delta t^4)$, whereas the momenta are affected by an error of $\mathcal{O}(\delta t^2)$. For this reason, the Verlet algorithm allows the use of a relatively large time increment δt. Further, it is time-reversible and shows excellent energy conservation properties.

In our MD code, a modification to the above outlined basic Verlet algorithm has been implemented. It is known as *velocity-Verlet algorithm* [35] and solves the equations of motion via the following Taylor expansions,

$$\boldsymbol{r}_i(t + \delta t) = \boldsymbol{r}_i(t) + \frac{\boldsymbol{p}_i(t)}{m_i}\,\delta t + \frac{1}{2m_i}\boldsymbol{f}_i(t)\,\delta t^2$$
$$\boldsymbol{p}_i(t + \delta t) = \boldsymbol{p}_i(t) + \frac{1}{2m_i}[\boldsymbol{f}_i(t) + \boldsymbol{f}_i(t + \delta t)]\,\delta t. \tag{2.20}$$
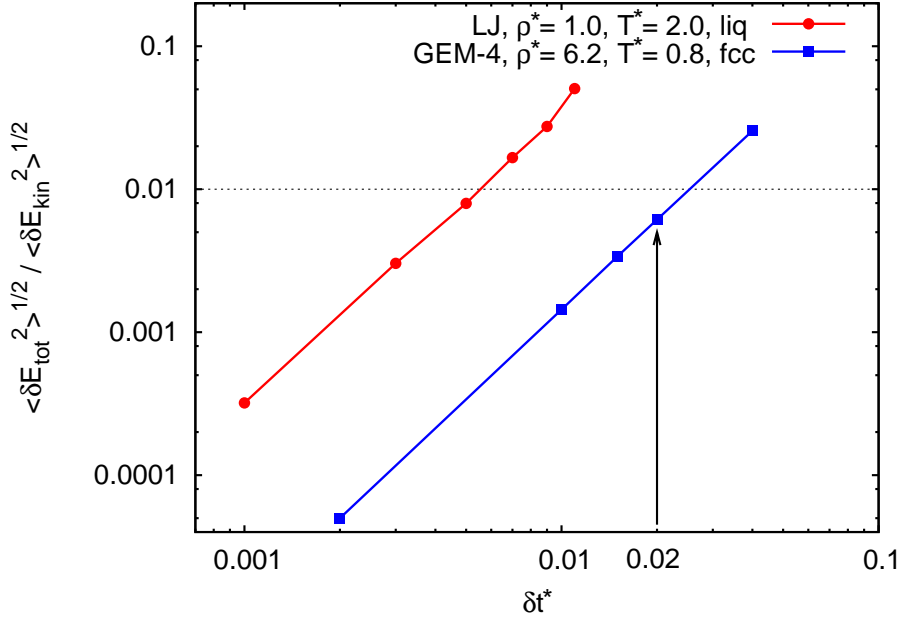
Figure 2.5: A rough guideline for the appropriate choice of the time increment suggests to fix δt^* such that $\sigma(E_{tot})$ represents at most 1% of $\sigma(E_{kin})$. Note that the starred δt, δt^*, indicates the use of reduced units (see Appendix A.2).

Because it minimises round-off errors [25], it is superior to the simple Verlet algorithm due to its better precision [35] and includes the momenta in the calculation in a more natural way, yet it shares all of the aforementioned qualities.

Having now an appropriate algorithm to calculate the particle trajectories at hand, we still need to determine an accurate value of the time increment, δt. In general, this decision involves a trade-off between simulation time and numerical precision. When choosing a value for δt the minimisation of both the energy drift of the system for long times and its fluctuations on a short-time scale must be considered. For this reason, a "good" value of δt also depends on the interaction model and on the state parameters, ϱ and T. As a rule of thumb the fluctuation of the total energy, $\sigma(E_{tot})$, of the system should never exceed one percent of the fluctuation of the kinetic energy, $\sigma(E_{kin})$[5],

$$\frac{\sigma(E_{tot})}{\sigma(E_{kin})} = \frac{\langle(\delta E_{tot})^2\rangle^{1/2}}{\langle(\delta E_{kin})^2\rangle^{1/2}} \leq 0.01. \tag{2.21}$$

As can be seen in Fig. 2.5, for the GEM-4 potential, this criterion suggests a time increment of $\delta t^* = 0.02$.

---

[5]In the microcanonical ensemble the fluctuation of the kinetic energy is equal to the fluctuation of the potential energy, $\sigma(E_{kin}) = \sigma(E_{pot})$.

We note at this point that the star superscript, " * ", is commonly used to indicate that the value of a starred quantity is given in reduced units (see [25], Appendix B). A list of reduced units for all quantities considered in this work is provided in Appendix A.2.

2.3.2   NVT simulations

Frequently, it is necessary to equilibrate a system at a desired temperature T, starting for example from a previous MD simulation at a different temperature T'. To this end, we need to perform simulations at constant temperature T. This is achieved by bringing the system, in the sense of statistical mechanics, into thermal contact with a large heat bath of temperature T. In our MD code, this has been implemented with the aid of a "massive stochastic" version of the *Andersen thermostat* [36]. At equally spaced intervals of time the velocities of all particles are redistributed according to the Maxwell-Boltzmann velocity distribution,

$$\mathcal{P}(v) = \left(\frac{\beta}{2\pi m}\right)^{3/2} \exp\left[-\beta m v^2/2\right], \tag{2.22}$$

which characterises the NVT-ensemble. Once the system is in equilibrium with the heat bath, we switch off the thermostat and continue the simulation in the microcanonical ensemble.

Chapter 3

Data analysis

In general, both Monte Carlo and molecular dynamics simulations must be followed by an extensive data analysis in which the quantities of interest (such as the radial distribution function or the velocity auto-correlation function) are calculated. In principle, this analysis may either be carried out during the simulation, or, once the simulation run is terminated, from a set of single-particle trajectories saved to a data file. As we took benefit from an existing MD simulations code (**atooms**[1]), we opted for the latter choice, i.e. a *post-processing* analysis, which includes a standard, a normal mode and a cluster post-processing analysis to be presented in this chapter.

3.1 Standard post-processing analysis

We restrict our discussion of the post-processing analysis to those static and dynamic quantities which are of most relevance to our work. In an effort to be as concise as possible, we present only their definitions and a few explanations, for further explications we refer to standard books on statistical physics such as [27, 37, 38]. As a starting point, it appears to be helpful to summarise the formalism of taking appropriate thermodynamic averages of the quantities under consideration.

3.1.1 Time averages and ensemble averages

The thermodynamic state of a monatomic system is characterised by a small set of *state variables* (such as temperature T, volume V, or number of particles N). The majority of thermodynamic properties that are of macroscopic interest solely depends on these few parameters. The time evolution of a system consisting of N particles is governed by (Newtonian) equations of motion. From the solution of the latter it is obtained a sequence of configurations in time which share the same set of natural

---

[1] **At**omistic **O**bject-**O**riented **M**olecular **S**imulations, by Daniele Coslovich <coslo@ts.infn.it>

variables. Each configuration is characterised by the positions $\boldsymbol{r}^N = \{\boldsymbol{r}_1, \boldsymbol{r}_2, ..., \boldsymbol{r}_N\}$ and momenta $\boldsymbol{p}^N = \{\boldsymbol{p}_1, \boldsymbol{p}_2, ..., \boldsymbol{p}_N\}$ of all particles in three-dimensional space and can thus be represented by a point in the $6N$-dimensional phase space.

The positions and momenta for all times, t, define the system's trajectory through phase space and are used to calculate the *time average* of any function of phase space $\mathcal{A}(\boldsymbol{r}^N, \boldsymbol{p}^N)$. Denoting a particular point in phase space $(\boldsymbol{r}^N, \boldsymbol{p}^N)$ with $\boldsymbol{\Gamma}(t)$, the time average of an experimentally observable macroscopic property $\mathcal{A}(\boldsymbol{\Gamma})$ is given by

$$\mathcal{A}_{\text{obs}} = \langle \mathcal{A} \rangle_{\text{time}} = \langle \, \mathcal{A}(\boldsymbol{\Gamma}(t)) \, \rangle_{\text{time}} = \lim_{\tau \to \infty} \frac{1}{\tau} \int\limits_0^\tau \mathcal{A}(\boldsymbol{\Gamma}(t)) \, \mathrm{d}t. \tag{3.1}$$

In reality, it is of course impossible to take a measurement over an infinite period of time. In this case, τ is replaced by τ_{obs} which must be greater than the typical relaxation times[2] of $\mathcal{A}$ to obtain a reliable average, which is independent of the initial conditions.

Alternatively, macroscopic quantities can be obtained within the framework of statistical physics via *ensemble averages*. These averages are calculated from an ensemble of imaginary, macroscopically equivalent systems, each of them corresponding to a different point in phase space. These points $\boldsymbol{\Gamma}$ are distributed according to a probability density (*phase space density*), $\varrho_{\text{ens}}(\boldsymbol{\Gamma})$, which is determined by the choice of the state variables, exclusively. The ensemble average reads

$$\mathcal{A}_{\text{obs}} = \langle \mathcal{A} \rangle_{\text{ens}} = \int \mathcal{A}(\boldsymbol{\Gamma}) \, \varrho_{\text{ens}}(\boldsymbol{\Gamma}) \, \mathrm{d}\boldsymbol{\Gamma} = \iint \mathcal{A}(\boldsymbol{r}_N, \boldsymbol{p}_N) \, \varrho_{\text{ens}}(\boldsymbol{r}_N, \boldsymbol{p}_N) \, \mathrm{d}\boldsymbol{r}^N \mathrm{d}\boldsymbol{p}^N. \tag{3.2}$$

Systems in which the time average is identical to the ensemble average,

$$\langle \mathcal{A} \rangle_{\text{time}} = \langle \mathcal{A} \rangle_{\text{ens}}, \tag{3.3}$$

are called *ergodic*. Ergodicity holds if a system passes "sufficiently close" [39] to all phase points for which ϱ_{ens} is non-zero and returns to the point of departure after a finite time[3]. However, for the overwhelming majority of systems this equation cannot be proven rigorously; thus in most cases one has to rely on the mere hope that the system under consideration is ergodic.

For practical purposes, eqs. (3.1) and (3.2) for the time average and the ensemble average respectively have to be modified to be of use in a molecular simulation. For instance, given an MD simulation over a finite time interval τ_{obs} and based on the

---

[2]The relaxation time of a quantity $\mathcal{A}$ is generally considered to be the period of time after which initial fluctuations of $\mathcal{A}$ about its equilibrium value are relaxed.

[3]This time is known as Poincaré recurrence time.

choice of a discrete time step δt, the integral in eq. (3.1) has to be replaced by a sum

$$\mathcal{A}_{\text{obs}} = \langle \mathcal{A} \rangle_{\text{time}} = \frac{1}{\tau_{\text{obs}}} \sum_{t=0}^{\tau_{\text{obs}}} \mathcal{A}(\mathbf{\Gamma}(t)), \tag{3.4}$$

where t now refers to the configurations $\mathbf{\Gamma}(t)$ separated in time by δt. On the other hand, the concept of ensemble averages is taken up in MC simulations. Provided that we manage to generate (somehow) a succession of M configurations $\{\mathbf{\Gamma}_1, \mathbf{\Gamma}_2, ..., \mathbf{\Gamma}_M\}$ reflecting a representative part of phase space, we can make use of the ensemble average to calculate the values of the interesting macroscopic quantities. In this case, eq. (3.2) reduces to a discrete sum

$$\mathcal{A}_{\text{obs}} = \langle \mathcal{A} \rangle_{\text{ens}} = \frac{1}{M} \sum_{i=1}^{M} \mathcal{A}(\mathbf{\Gamma}_i). \tag{3.5}$$

These configurations $\{\mathbf{\Gamma}_i\}$ are not calculated by equations of motion anymore, but by a stochastic algorithm, such as the one presented in Section 2.3.

In the next two subsections we will introduce and define those static and dynamic quantities that are most important for our work. In both cases we deal with *auto-correlation functions*. For a static auto-correlation function we correlate a function of phase space $\mathcal{A}$ at one time to its value at the same time, averaging over many points in time,

$$\langle \mathcal{A}(0)\mathcal{A}(0) \rangle_{\text{time}}. \tag{3.6}$$

To obtain a dynamic auto-correlation function, we correlate the same function at one time to its value at a different time, averaging over many time origins,

$$\langle \mathcal{A}(t)\mathcal{A}(0) \rangle_{\text{time}}. \tag{3.7}$$

In what follows we will stick to standard notation of statistical mechanics, denoting averages by "$\langle \, . \, \rangle$" without specifying whether they are calculated by taking the time or the ensemble average.

3.1.2 Static structural quantities

Radial distribution function $g(r)$

The *pair distribution function*, $g_N(\boldsymbol{r}_1, \boldsymbol{r}_2)$, for a monatomic system consisting of N particles confined in a volume V at temperature T (canonical ensemble) is given by

$$g_N(\mathbf{r}_1, \mathbf{r}_2) = \frac{N(N-1)}{\varrho^2 Z_N} \int ... \int e^{-\beta \mathcal{U}(\mathbf{r}^N)} \, \mathrm{d}\boldsymbol{r}_3 ... \mathrm{d}\boldsymbol{r}_N, \tag{3.8}$$

where ϱ is the density of the system (see Appendix A.1, eq. (A.1)) and Z_N is the configurational integral

$$Z_N = \int e^{-\beta \mathcal{U}(\mathbf{r}^N)} \, \mathrm{d}\boldsymbol{r}^N. \tag{3.9}$$

$g_N(\boldsymbol{r}_1, \boldsymbol{r}_2) \, \mathrm{d}\boldsymbol{r}_1 \mathrm{d}\boldsymbol{r}_2$ is a measure for the probability of finding two particles in the volume element $(\boldsymbol{r}_1 + \mathrm{d}\boldsymbol{r}_1) \times (\boldsymbol{r}_2 + \mathrm{d}\boldsymbol{r}_2)$, irrespective of the positions of all other particles and irrespective of all momenta.

Restricting our considerations to a homogeneous, isotropic system we see that the dependency of $g_N(\boldsymbol{r}_1, \boldsymbol{r}_2)$ reduces to a function of the particle separation $r = |\boldsymbol{r}_1 - \boldsymbol{r}_2|$ and eq. (3.8) becomes an ensemble average of the form

$$g(r) = \frac{V}{N^2} \left\langle \sum_{i \neq j} \delta(\boldsymbol{r} - \boldsymbol{r}_{ij}) \right\rangle. \tag{3.10}$$

This is an expression that can be easily evaluated in computer simulations [25]. $g(r)$ is called *radial distribution function* (RDF) and indicates the probability of finding a pair of particles a distance r apart, compared to the same probability in a completely random system. In this sense, the particle distribution function is a measure of the extent to which the structure of a fluid differs from the structure of an ideal gas [27]. The RDF is an essential ingredient to the formalism of statistical physics as it may be used to express the ensemble average of any pair function $a(\boldsymbol{r}_i, \boldsymbol{r}_j)$ in a very simple and condensed form,

$$\langle a(\boldsymbol{r}_i, \boldsymbol{r}_j) \rangle = \frac{1}{V^2} \int \mathrm{d}\boldsymbol{r}_i \mathrm{d}\boldsymbol{r}_j \, g(r) \, a(\boldsymbol{r}_i, \boldsymbol{r}_j). \tag{3.11}$$

In particular, the knowledge of this function provides a convenient way of calculating thermodynamic properties as well the equation of state of the system.

Furthermore, the RDF contains information about the system's structure. From the positions and relative amplitudes of its peaks it is possible to distinguish unambiguously between different phases, such as the liquid, the body-centred cubic (bcc) and the face-centred cubic (fcc) phase (see Fig. 3.1). Integration of $4\pi r^2 \varrho g(r)$ up to its first minimum serves as an estimate of the nearest-neighbour *coordination number*, which is the number of particles in the first shell of nearest-neighbours. For instance, for the bcc and fcc phase, the coordination number takes characteristic values of 8 and 12, respectively. Interestingly enough, for a clustering system, the same measure yields the average occupation number of lattice sites $\langle n_{\mathrm{c}} \rangle$, which is to be discussed in Section 3.3 in more detail.
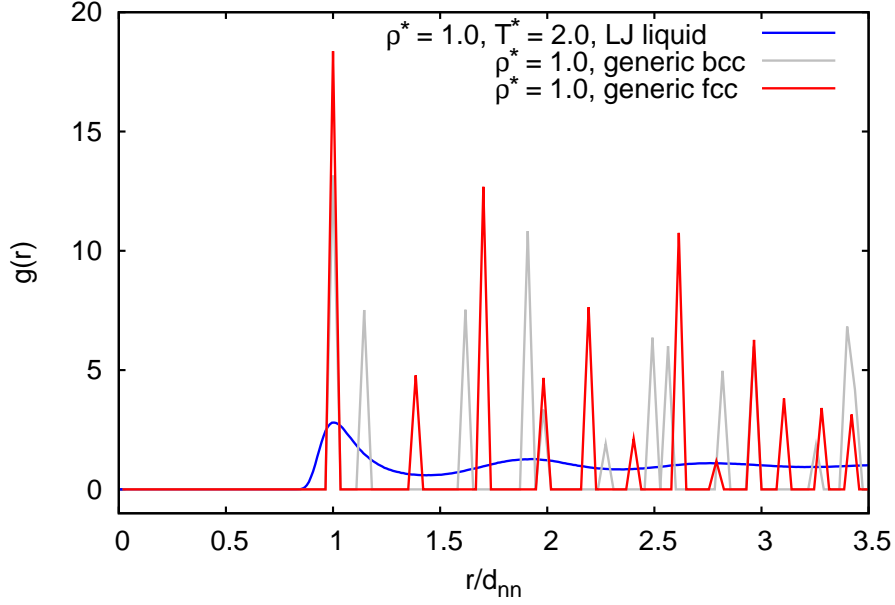
Figure 3.1: Typical shape of the radial distribution function, $g(r)$, of monatomic liquid and crystalline systems with spherically symmetric interactions. $g(r)$ of a Lennard-Jones liquid and of two generic crystal structures is shown. The peak structure is characteristic to every phase (liquid, body-centred cubic (bcc) and face-centred cubic (fcc)). r is scaled in units of the nearest-neighbour distance, d_{nn}, of the respective structures.

Static structure factor $S(\boldsymbol{k})$

The *static structure factor*, $S(\boldsymbol{k})$, is defined as

$$S(\boldsymbol{k}) = \frac{1}{N} \langle\, \varrho(\boldsymbol{k})\, \varrho(-\boldsymbol{k}) \,\rangle, \tag{3.12}$$

where $\varrho(\boldsymbol{k})$, the spatial Fourier transform of the number density $\varrho(\boldsymbol{r}) = \sum_{i=1}^{N} \delta(\boldsymbol{r} - \boldsymbol{r}_i)$, is given by

$$\varrho(\boldsymbol{k}) = \sum_{i=1}^{N} e^{i\boldsymbol{k}\cdot\boldsymbol{r}_i}. \tag{3.13}$$

For homogeneous, isotropic systems the static structure factor reduces to a function $S(k)$ of the modulus of the wave vector $\boldsymbol{k}$. In this case, it is related to $g(r)$ through the Fourier transform

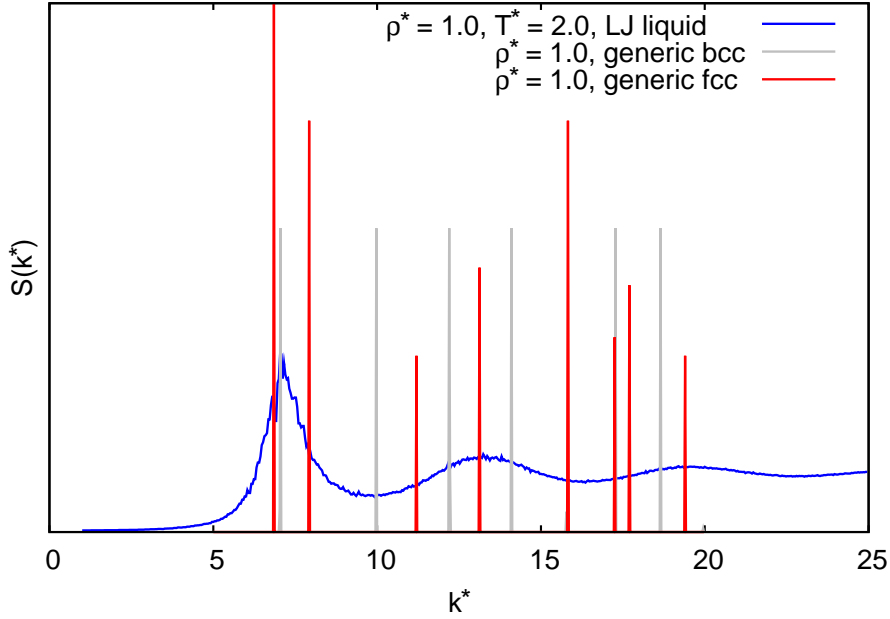$$S(|\boldsymbol{k}|) = 1 + 4\pi\varrho \int_{0}^{\infty} r^2 \frac{\sin kr}{kr}\, g(r)\, \mathrm{d}r. \tag{3.14}$$

Figure 3.2: Typical shape of the static structure factor, $S(k^*)$, of monatomic, liquid and crystalline systems with spherically symmetric interactions. $S(k^*)$ of a Lennard-Jones liquid and of two generic crystal structures is shown. Similarly to the RDF, $g(r)$, the peak structure in $S(k^*)$ is characteristic to every phase (liquid, bcc and fcc). The vertical axis is scaled arbitrarily to enhance the visibility of the peaks.

$S(\boldsymbol{k})$ is a measure of the response of a system in equilibrium to a density fluctuation of wavelength $2\pi/k$. Again, the order and relative amplitudes of its peaks can be used to identify the crystal structure (see Fig. 3.2).

3.1.3 Dynamic quantities

Velocity auto-correlation function $c_v(t)$

The *velocity auto-correlation function* (VACF), $c_v(t)$, is one of the simplest but most important examples of a time-correlation function. It is defined as

$$c_v(t) = \frac{1}{3} \left\langle \boldsymbol{v}_i(t)\,\boldsymbol{v}_i(0) \right\rangle, \tag{3.15}$$

which is the ensemble averaged projection of the velocity $\boldsymbol{v}_i(t)$ of a particle i at time t onto its initial velocity $\boldsymbol{v}_i(0)$. Its value at $t = 0$ is given by

$$c_v(t = 0) = \frac{1}{3} \left\langle \boldsymbol{v}^2 \right\rangle = \frac{k_B T}{m}, \tag{3.16}$$
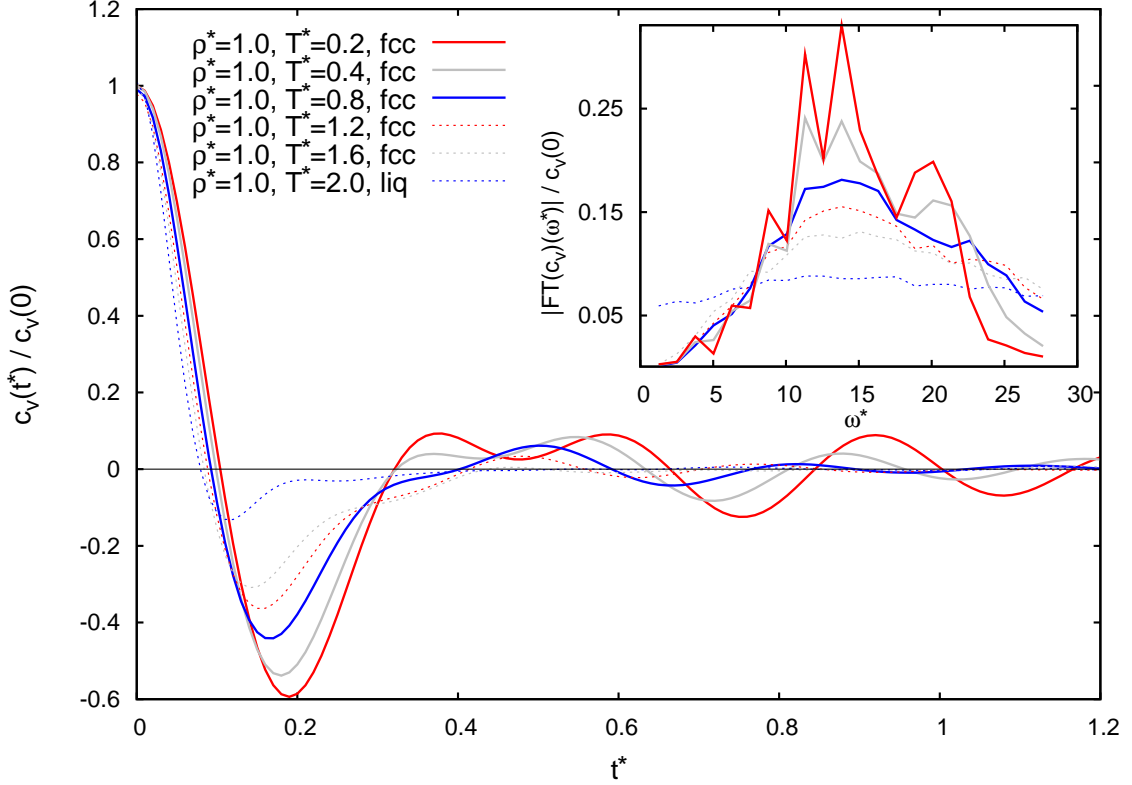
Figure 3.3: VACF, $c_v(t^*)$, of a Lennard-Jones system at density $\varrho^* = 1.0$ and different temperatures. Note that the decay time of the VACF depends on T^*. In the inset the Fourier transform of the VACF, $\tilde{c}_v(\omega^*)$, for the same state points is shown.

where the latter equivalence is given by the equipartition theorem [37]. $c_v(t)$ (see Fig. 3.3) vanishes at times sufficiently large compared to typical microscopic relaxation times, i.e. where initial and final velocities will be completely uncorrelated,

$$c_v(t \to \infty) = 0. \tag{3.17}$$

The Fourier transform of the VACF,

$$\tilde{c}_v(\omega) = \frac{1}{2\pi} \int_{-\infty}^{\infty} c_v(t)\, e^{i\omega t}\, \mathrm{d}t, \tag{3.18}$$

gives us a hint to the spectrum of vibrations present in the system (see the inset of Fig. 3.3). In addition, in a liquid the value $\tilde{c}_v(\omega = 0)$ is a signature of diffusion in the system by virtue of the *Green-Kubo* formula [27]

$$D = \frac{1}{3} \int_{0}^{\infty} \left\langle |\boldsymbol{v}_i(t) \cdot \boldsymbol{v}_i(0)|^2 \right\rangle \mathrm{d}t. \tag{3.19}$$
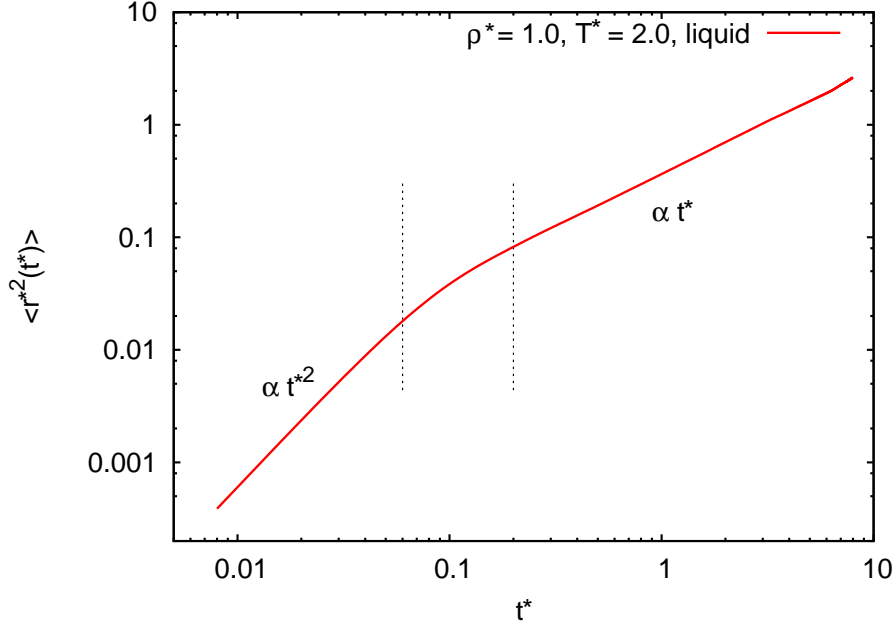
Figure 3.4: Mean square displacement of particles in a Lennard-Jones liquid at $\varrho^* = 1.0$ and $T^* = 2.0$ in double log scale. For short times, $\langle r^{*2}(t^*) \rangle$ grows with t^{*2}, which is known as "ballistic" regime. After an intermediate crossover region (corresponding to typical collision times) it scales linearly with t^* for times such that the root of the MSD exceeds one interparticle separation.

Mean square displacement $\langle r^2(t) \rangle$

The *mean square displacement* (MSD), $\langle r^2(t) \rangle$, measures the square of the displacement of a tagged particle i from an initial configuration, averaged over independent time origins. It is given by

$$\langle r^2(t) \rangle = \langle |\boldsymbol{r}_i(t) - \boldsymbol{r}_i(0)|^2 \rangle. \tag{3.20}$$

The MSD ranges among the most important quantities characterising the thermodynamic properties of a system. It is linked to the time-*in*dependent diffusion coefficient, D, by the Einstein relation

$$D = \lim_{t \to \infty} \frac{1}{6t} \langle |\boldsymbol{r}_i(t) - \boldsymbol{r}_i(0)|^2 \rangle. \tag{3.21}$$

Typically, for a fluid system this linear behaviour is met for times such that the root of the MSD exceeds one interparticle separation (see Fig. 3.4).

Van Hove correlation function $G(\boldsymbol{r}, t)$

The *van Hove correlation function*, $G(\boldsymbol{r}, t)$, is a space and time-dependent correlation function, defined as

$$G(\boldsymbol{r}, t) = \left\langle \frac{1}{N} \sum_{i=1}^{N} \sum_{j=1}^{N} \int \delta[\boldsymbol{r} - \boldsymbol{r}_j(t) + \boldsymbol{r}_i(0)] \right\rangle =$$
$$= \frac{1}{\varrho} \langle \varrho(\boldsymbol{r}, t)\, \varrho(\boldsymbol{0}, 0) \rangle, \tag{3.22}$$

where $\varrho(\boldsymbol{r}, t)$ is the time-dependent number density,

$$\varrho(\boldsymbol{r}, t) = \sum_{i=1}^{N} \delta(\boldsymbol{r} - \boldsymbol{r}_i(t)). \tag{3.23}$$

The last term in eq. (3.22) shows that the van Hove correlation function is a density-density correlation function. $G(\boldsymbol{r}, t)\mathrm{d}\boldsymbol{r}$ measures the number of particles j located in a volume element $\mathrm{d}\boldsymbol{r}$ around a point $\boldsymbol{r}$ at time t, given that at time $t = 0$ a particle i was located at the origin, $\boldsymbol{0}$. The van Hove correlation function can be split up into two terms, usually called the "self" (s) and the "distinct" (d) part,

$$G(\boldsymbol{r}, t) = G_{\mathrm{s}}(\boldsymbol{r}, t) + G_{\mathrm{d}}(\boldsymbol{r}, t), \tag{3.24}$$

which takes into account that i and j may be the same particle or different ones [27]. The "self" part, defined as

$$G_{\mathrm{s}}(\boldsymbol{r}, t) = \left\langle \frac{1}{N} \sum_{i=1}^{N} \delta[\boldsymbol{r} - \boldsymbol{r}_i(t) + \boldsymbol{r}_i(0)] \right\rangle, \tag{3.25}$$

is the one which is most relevant for our work, as we will see in the analysis of the diffusive behaviour of a cluster crystal (cf. Chapter 5). Similarly to the RDF, $g(r)$, for *isotropic* systems $G_{\mathrm{s}}(\boldsymbol{r}, t)$ reduces to $G_{\mathrm{s}}(r, t)$, a function of the particle separation $r = |\boldsymbol{r}_1 - \boldsymbol{r}_2|$.

Intermediate scattering function $F(\boldsymbol{k}, t)$

The Fourier transform of the van Hove correlation function,

$$F(\boldsymbol{k}, t) = \int G(\boldsymbol{r}, t)\, e^{-i\boldsymbol{k}\cdot\boldsymbol{r}}\, \mathrm{d}\boldsymbol{r}, \tag{3.26}$$

is called *intermediate scattering function* and represents the time-dependent auto-correlation of density fluctuations of wave vector $\boldsymbol{k}$,

$$F(\boldsymbol{k}, t) = \frac{1}{N} \langle \varrho(\boldsymbol{k}, t)\, \varrho(-\boldsymbol{k}, 0) \rangle. \tag{3.27}$$

Here, $\varrho(\boldsymbol{k})$ is given by eq. (3.13), where we replaced $\boldsymbol{r}_i$ by a time-dependent $\boldsymbol{r}_i(t)$. In the same way as the van Hove correlation function it may be separated into a "self" and a "distinct" part, as becomes clear when inserting eq. (3.24) into eq. (3.26). The self intermediate scattering function $F_{\mathrm{s}}(\boldsymbol{k}, t)$ describes the "self dynamics" of a system, related to single-particle motion.

Dynamic structure factor $S(\boldsymbol{k}, \omega)$

For the sake of completeness, we mention the *dynamic structure factor*, $S(\boldsymbol{k}, \omega)$, given by the time Fourier transform of $F(\boldsymbol{k}, t)$,

$$S(\boldsymbol{k}, \omega) = \frac{1}{2\pi} \int\limits_{-\infty}^{\infty} F(\boldsymbol{k}, t) \, e^{i\omega t} \, \mathrm{d}t. \tag{3.28}$$

Integrating $S(\boldsymbol{k}, \omega)$ over all frequencies leads to the static structure factor,

$$\int\limits_{-\infty}^{\infty} S(\boldsymbol{k}, \omega) \, \mathrm{d}\omega = F(\boldsymbol{k}, 0) = S(\boldsymbol{k}). \tag{3.29}$$

3.2 Normal mode analysis

In Section 3.1.3 we have mentioned that the Fourier transform of the VACF allows a first insight into the vibrational spectrum of a system. A more direct route, however, to determine the "true" vibrational density of states is provided by *normal mode analysis* (NMA). The latter can be achieved by a two-step procedure [40]:

- Minimisation of the total potential energy of one or more instantaneous configurations taken out of a simulation run, to locate the nearest local minimum of the potential energy surface.

- NMA of these minimised configurations by diagonalising the *dynamical matrix* in real space.

Both steps will be explained in the following.

3.2.1 Minimisation

Stated in general terms, a minimisation technique aims at minimising a generic function $\mathcal{F}(x)$, where x stands for a large number of variables, for instance a point $x = \{\boldsymbol{r}^N\}$ in configuration space. Today, a broad range of minimisation algorithms

of different complexity and effectiveness exists [41], spanning from the "steepest descent" minimisation over the "conjugate gradient" method to the BFGS algorithm.

In the present work, we employ a so-called *limited-memory quasi-Newton* method for the minimisation of the potential energy $\mathcal{U}$. It is known as l-BFGS algorithm, **l**imited **B**royden-**F**letcher-**G**oldfarb-**S**hanno algorithm, in the implementation of Liu and Nocedal [42]. The attribute "limited-memory" ("l-"BFGS) refers to the fact that the algorithm memory requirements can be controlled by the user. For this reason, the l-BFGS algorithm is particularly suitable for large scale problems involving a considerable number of degrees of freedom [40, 42].

3.2.2 Calculation of normal modes

In the framework of classical theory of harmonic crystals [24] the total potential energy of a crystal is written as

$$\mathcal{U} = \frac{1}{2} \sum_{\boldsymbol{R},\boldsymbol{R}'} \phi(\boldsymbol{r}(\boldsymbol{R}) - \boldsymbol{r}(\boldsymbol{R}')). \tag{3.30}$$

In this expression $\boldsymbol{r}(\boldsymbol{R})$ denotes a particle's position $\boldsymbol{r}$ displaced from its original position $\boldsymbol{R}$ in a Bravais lattice, which is characterised by the primitive lattice vectors $\boldsymbol{a}_i$ ($i = 1, 2, 3$). In what is called *harmonic approximation*, $\mathcal{U}$ is approximated by the sum of two terms, $\mathcal{U}^{\text{eq}}$ and $\mathcal{U}^{\text{harm}}$, which are retained from a full Taylor series expansion of $\mathcal{U}$ about the equilibrium configuration $\{\boldsymbol{R}\}$. Adopting the commonly approved notation of [24], these terms are given by

$$\begin{aligned}
\mathcal{U}^{\text{eq}} &= \frac{1}{2} \sum_{\boldsymbol{R},\boldsymbol{R}'} \phi(\boldsymbol{R} - \boldsymbol{R}') \\
\mathcal{U}^{\text{harm}} &= \frac{1}{2} \sum_{\boldsymbol{R},\boldsymbol{R}'} \boldsymbol{u}(\boldsymbol{R})\, \boldsymbol{D}(\boldsymbol{R} - \boldsymbol{R}')\, \boldsymbol{u}(\boldsymbol{R}')
\end{aligned} \tag{3.31}$$

with $\boldsymbol{u} = \boldsymbol{r}(\boldsymbol{R}) - \boldsymbol{R}$ being the particle displacement from the respective lattice sites, and

$$\boldsymbol{D}(\boldsymbol{R} - \boldsymbol{R}') = \left.\frac{\partial^2 \mathcal{U}}{\partial \boldsymbol{u}(\boldsymbol{R})\, \partial \boldsymbol{u}(\boldsymbol{R}')}\right|_{\boldsymbol{u}=\boldsymbol{0}}. \tag{3.32}$$

Considering a three-dimensional system consisting of N particles of mass m, the formalism leads to $3N$ equations of motion:

$$m\ddot{\boldsymbol{u}}(\boldsymbol{R}) = -\frac{\partial \mathcal{U}^{\text{harm}}}{\partial \boldsymbol{u}(\boldsymbol{R})} = -\sum_{\boldsymbol{R}'} \boldsymbol{D}(\boldsymbol{R} - \boldsymbol{R}')\, \boldsymbol{u}(\boldsymbol{R}'). \tag{3.33}$$

From an ansatz to solve these equations we yield their eigenfunctions, which take the form of simple plain waves

$$\boldsymbol{u}(\boldsymbol{R}, t) = \boldsymbol{\epsilon}\, e^{i(\boldsymbol{k}\boldsymbol{R} - \omega t)}, \quad \boldsymbol{\epsilon} \in \mathbb{R}^3. \tag{3.34}$$

By the use of periodic boundary conditions (cf. Section 2.1.2) the number of all possible wave vectors $\boldsymbol{k}$ in eq. (3.34) is reduced to a set of N nonequivalent values.

Upon inserting eq. (3.34) into eq. (3.33) and including the symmetry properties of $\boldsymbol{D}$ [24] we obtain the eigenvalue problem for $\boldsymbol{\epsilon}$,

$$m\omega^2\boldsymbol{\epsilon} = \boldsymbol{D}(\boldsymbol{k})\boldsymbol{\epsilon}, \tag{3.35}$$

where

$$\boldsymbol{D}(\boldsymbol{k}) = \sum_{\boldsymbol{R}} \boldsymbol{D}(\boldsymbol{R})\, e^{-i\boldsymbol{k}\boldsymbol{R}} \tag{3.36}$$

is called *dynamical matrix*. One finds that for each of the N values of $\boldsymbol{k}$ there exist three solutions $\boldsymbol{\epsilon}_i(\boldsymbol{k})\,(i = 1, 2, 3)$ to eq. (3.35), leading to $3N$ normal modes. They are obtained by diagonalisation of the $3N \times 3N$ dimensional dynamical matrix $\boldsymbol{D}$. Whether we diagonalise $\boldsymbol{D}$ in its k-representation, $\boldsymbol{D}(\boldsymbol{k})$, or its representation in real space, $\boldsymbol{D}(\boldsymbol{R})$, is not of any importance for the final result, as long as we are interested in the vibrational density of states only. Due to eq. (3.36) both matrices share an equivalent spectrum of eigenvalues and eigenvectors and the same symmetries hold – they are positive semidefinite symmetric matrices.[4,5]

In our work, we choose to diagonalise $\boldsymbol{D}(\boldsymbol{R})$, which is more straight-forward with the Hessian matrix at hand. By virtue of eq. (3.35), from the diagonalisation of $\boldsymbol{D}(\boldsymbol{R})$ we obtain a set of $3N$ normalised eigenvectors and $3N$ corresponding real eigenvalues

$$\boldsymbol{\epsilon}_\alpha \quad \text{and} \quad \omega_\alpha \quad (\alpha = 1, ..., 3N). \tag{3.37}$$

For each normal mode α the $3N$-dimensional vector $\boldsymbol{\epsilon}_\alpha$ contains the vector displacements $\boldsymbol{e}_\alpha^i\,(i = 1, ..., N)$ of every particle on the mode.

From our results we gain the vibrational density of states (VDOS) [43] by

$$\mathcal{D}(\omega) = \left\langle \frac{1}{3N} \sum_{\alpha=1}^{3N} \delta(\omega - \omega_\alpha) \right\rangle, \tag{3.38}$$

---

[4]The eigenvalues of a positive semi-definite matrix are all greater or equal to zero.

[5]We stress that this is only true for a configuration $\{\boldsymbol{R}\}$ corresponding to a (local) minimum of $\mathcal{U}$. At this minimum, the potential energy surface is positively curved in all directions. In contrast to this, the normal mode spectrum evaluated at a saddle point or an "instantaneous" configuration [40, 43] will contain a finite fraction of negative eigenvalues.
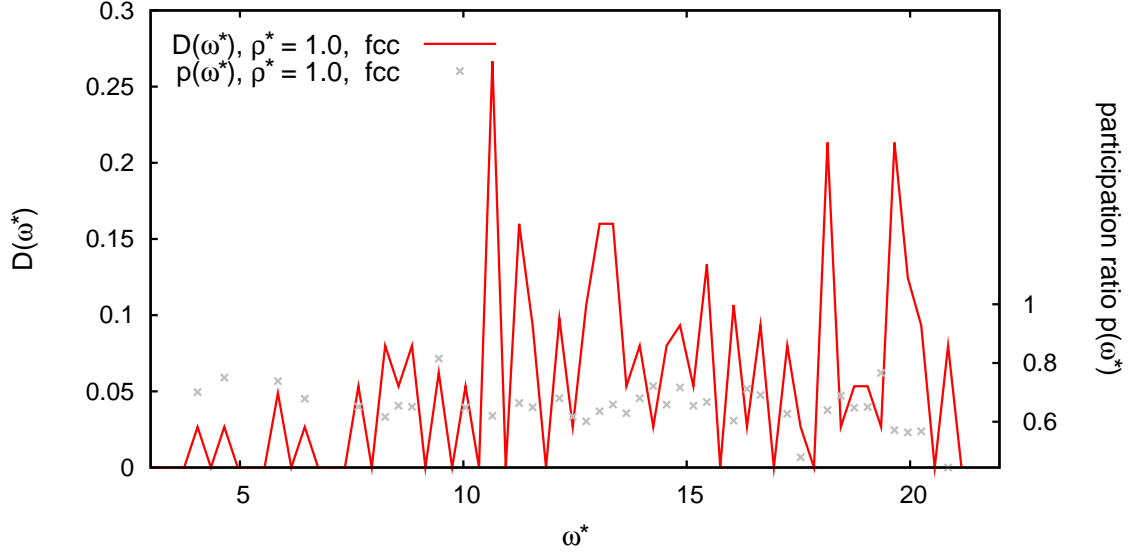
Figure 3.5: Vibrational density of states, $\mathcal{D}(\omega^*)$, and the participation ratio, $p(\omega^*)$, for the fcc phase of a Lennard-Jones system. A small value of $p(\omega^*)$ corresponds to high localisation, a high value of $p(\omega^*)$ to low localisation of normal modes lying in a frequency interval $\mathrm{d}\omega^* = 0.3$ around ω^*.

where the angular brackets refer to taking the average over all analysed configurations. A standard measure of the localisation of a normal mode α is its *participation ratio* defined as

$$p_\alpha = \left[N \sum_{i=1}^{N} (\boldsymbol{e}_\alpha^i \cdot \boldsymbol{e}_\alpha^i) \right]^{-1}. \tag{3.39}$$

This quantity is of particular interest when characterising the spectrum of vibrations in a cluster crystal, since it will enable us to distinguish between collective and single-particle vibrational motion in a clustering system (cf. Chapter 4). The vibrational density of states and the participation ratio are illustrated in Fig. 3.5 for a Lennard-Jones fcc crystal.

Aiming at a deeper understanding of the spectrum of vibrations in a cluster crystal it is worth discussing the generalisation of our previous considerations to a three-dimensional lattice with a basis. The NMA of such a system will yield two different kinds of eigenfrequencies and eigenvectors. Let N_c be the number of lattice sites and n_b the number of particles in the basis for a system of $N = N_\mathrm{c} n_\mathrm{b}$ particles. Then, three out of $3n_\mathrm{b}$ vibrational branches are called *acoustic branches*, which essentially consist of vibrations of the lattice sites. The remaining $3(n_\mathrm{b} - 1)$ branches are known as *optical branches*, which contain normal modes associated with

the motion of particles relative to the motion of lattice sites. In Chapter 4 we will learn that, interestingly enough, a connection between acoustic and optical branches and collective and individual motion of particles can be established.

3.3   Cluster post-processing analysis

Investigating the dynamics of a cluster crystal requires a thorough analysis of its cluster objects. First of all we must decide on a criterion for what we call a *cluster object*. From Fig. 3.6 we see that $g(r)$ of cluster crystals shows a characteristic rise as r tends to zero. The position of the first minimum in $g(r)$, $r_{\min}$, may serve as a measure of a cluster's spatial extent and allow us to determine the average cluster size, $\langle n_{\mathrm{c}} \rangle$, as well,

$$\langle n_{\mathrm{c}} \rangle = 1 + 4\pi\varrho \int\limits_0^{r_{\min}} \mathrm{d}r\, r^2 g(r). \tag{3.40}$$

This definition has been suggested in [9]. However, clusters do not have well-defined boundaries – $g(r)$ does not vanish completely at $r_{\min}$ (see the inset of Fig. 3.6). This means that this quantity should be rather only used as a rough estimate that provides a first insight into the underlying distribution of cluster sizes. If we want to go beyond the calculation of static cluster properties we must analyse clusters individually, using a radius of the order of $r_{\min}$ as a threshold to group particles together.

As a starting point, we pick up the basic ideas developed in [9].[6] We realise however that, for our purposes, it is necessary to considerably refine the technique of assigning particles to clusters. In view of the fact that we want to measure *dynamic* properties of our system we have to distinguish between different clusters unambiguously at each single step in time, otherwise taking the risk of losing track of their identities.

In the following we will present a 5-step strategy of identifying clusters.

3.3.1   From single-particle to cluster trajectories

As mentioned above, the only estimate of a cluster's spatial extent available at the moment is given by the position $r_{\min}$ of the first minimum in $g(r)$. We shall make use of this criterion in Step 1 of our analysis.

---

[6]In contrast to [9], we opted for not including the analysis in the MD simulations, but implementing it as a post-processing tool in our code. In this way, we keep the data analysis well separated from the simulations. This route is more comfortable from the programmer's point of view since it makes code debugging and code maintenance easier.
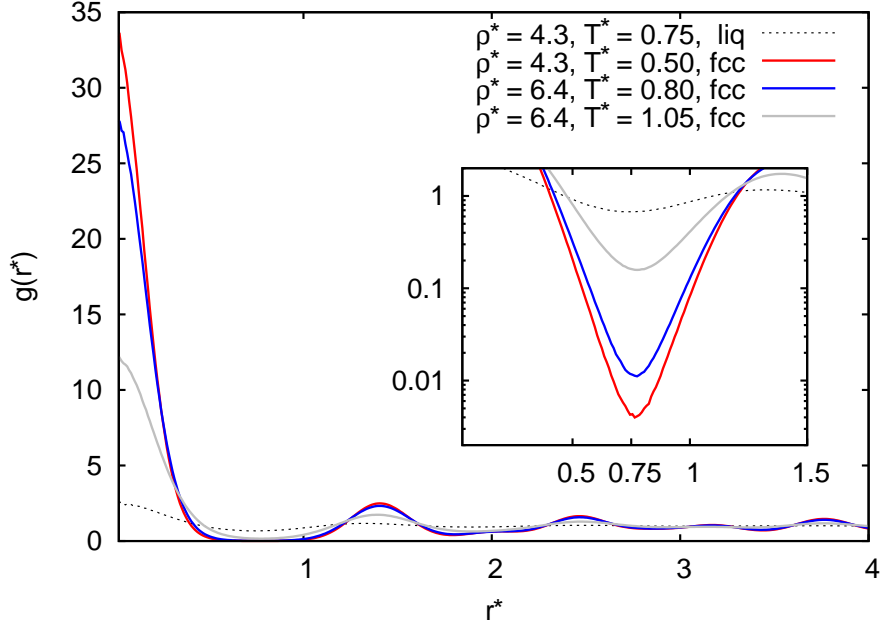
Figure 3.6: Radial distribution function, $g(r^*)$, of a GEM-4 cluster crystal as a function of r^* for two different densities ϱ^* and temperatures T^*. From the inset we see that $g(r^*)$ does not vanish completely at its first minimum, $r^*_{\min} = 0.75$.

Step 1 - Searching for neighbours.

We start with the first particle (particle 1) and calculate its distance from all other particles in the system. As a *neighbour* of particle 1 we regard all particles which lie within a sphere of *cutoff radius* r_c. Every particle that satisfies this criterion will be added to the set of neighbours of particle 1. Then we proceed to particle 2 and in a similar manner with all particles. We end up with an array of size N, containing the sets of neighbours of each particle. As a first guess the value of $r_{\min}$ is used for r_c. In Step 3 we will see that we still have to elaborate on this choice in order to optimise the algorithm in terms of speed.

Step 2 - Grouping particles to clusters.

With the sets of neighbours for all particles at hand, we head for the composition of the clusters. Starting again with particle 1, we label all its neighbours and their respective neighbours[7] with an identity number (ID), which in turn will be identified with a cluster. Then we proceed to the next particle that has not been labelled yet and finally arrive at a point where all particles have been assigned an identity. In the end, each ID corresponds to a cluster.

---

[7]To form a cluster we have to join overlapping sets of neighbours.

Step 3 - Separating merged clusters.

At this stage, using the algorithm described so far, we manage to reproduce the results obtained in [9] on the cluster size distribution (see Fig. 3.7, left panel). However, from the fact that $g(r)$ remains finite at its first minimum one concludes that, occasionally, the distance of a particle from the centre of mass (CM) of its cluster exceeds $r_{\min}$. This is the case if, at sufficiently high temperatures, particles hop from one cluster to another. The cluster analysis algorithm developed up to this point risks to fail in that case; particles of both the old and the new home cluster might be counted to the set of neighbours of the hopping particle, thereby merging the two clusters (see Fig. 3.8 (a)).

One may well think that these troubles can be overcome by reducing the r_{c} to small enough a fraction of $r_{\min}$; but, empirically, we realised that this choice does not solve the problem. On the one hand, in a cluster crystal of high density, situations occur in which, simultaneously, two or three particles are hopping to/from a cluster from/to clusters in its nearest surrounding. This means that taking a smaller value for r_{c} would not solve the problem of one particle merging two clusters. One can easily imagine an arrangement of two or more particles connecting two clusters or even three. On the other hand, decreasing the cutoff radius drastically brings about the problem that particles remain without any neighbours in their surrounding and are subsequently believed to be clusters on their own.

For these reasons, we have to develop a more sophisticated procedure to separate merged clusters, which does not rely on the mere reduction of r_{c}. To this end, we need to introduce three additional parameters in the cluster analysis procedure.

- $n_{\mathrm{c}}^{\min}$ and $n_{\mathrm{c}}^{\max}$, the minimum and maximum cluster size present in our system. Both of them are roughly estimated from the cluster size distribution calculated after Step 1 and 2 (see Fig. 3.7, left panel).

- N_{c}, the number of lattice sites in our system, which is expected to be equal to the amount of clusters in the crystal phase. Its value is known from the beginning of the molecular simulation. (Remember, for each point in the phase diagram, we start from a system configuration minimised in terms of its free energy F by varying total particle number N and volume V but keeping the number of lattice sites, N_{c}, constant.)

With these three parameters at hand, the algorithm aiming at separating merged clusters proceeds in the following way.

1. All clusters that have just been identified are reconsidered. If the size of one of them exceeds $n_{\mathrm{c}}^{\max}$, the collection of particles is isolated from the rest of the system (see Fig. 3.8 (a)).
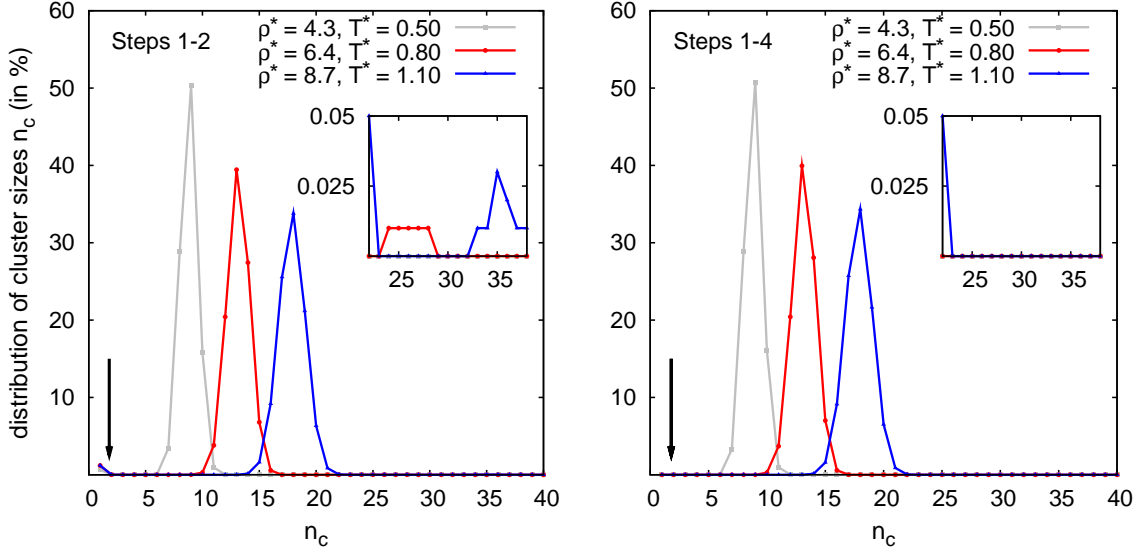
Figure 3.7: Distribution of cluster sizes n_c. Left panel, distribution calculated after Step 2 of the cluster analysis. From the inset it can be seen that there are still cases in which the algorithm merges two or three different clusters. Right panel, distribution calculated after Step 4. In the inset we see no signature of merged clusters anymore.

2. The search for neighbours is repeated just within the remaining set of particles (Fig. 3.8 (b)).

3. Those particles with the lowest number of neighbours are excluded from the others (Fig. 3.8 (c)). The reason for doing so is that particles at the boundaries of a cluster have a number of neighbours that is small compared to the average cluster population. We assume that these particles are responsible for merging the clusters.

4. Once again the neighbours are identified, ignoring now the excluded particles.

5. Step 2 is performed for the updated sets of neighbours, giving disjoint clusters (Fig. 3.8 (d)).

6. All particles excluded during the last two steps are reassigned to those clusters with the nearest centre of mass position (Fig. 3.8 (e) and (f)).

7. As a last point, the following checks are made: (i) Does the size of all newly derived clusters lie within n_c^{min} and n_c^{max}? (ii) Is the number of clusters identified in the system equal to the number of lattice sites, N_c? If one of these two conditions is not satisfied, the current procedure is iterated, reducing the cutoff radius r_c at each iteration.
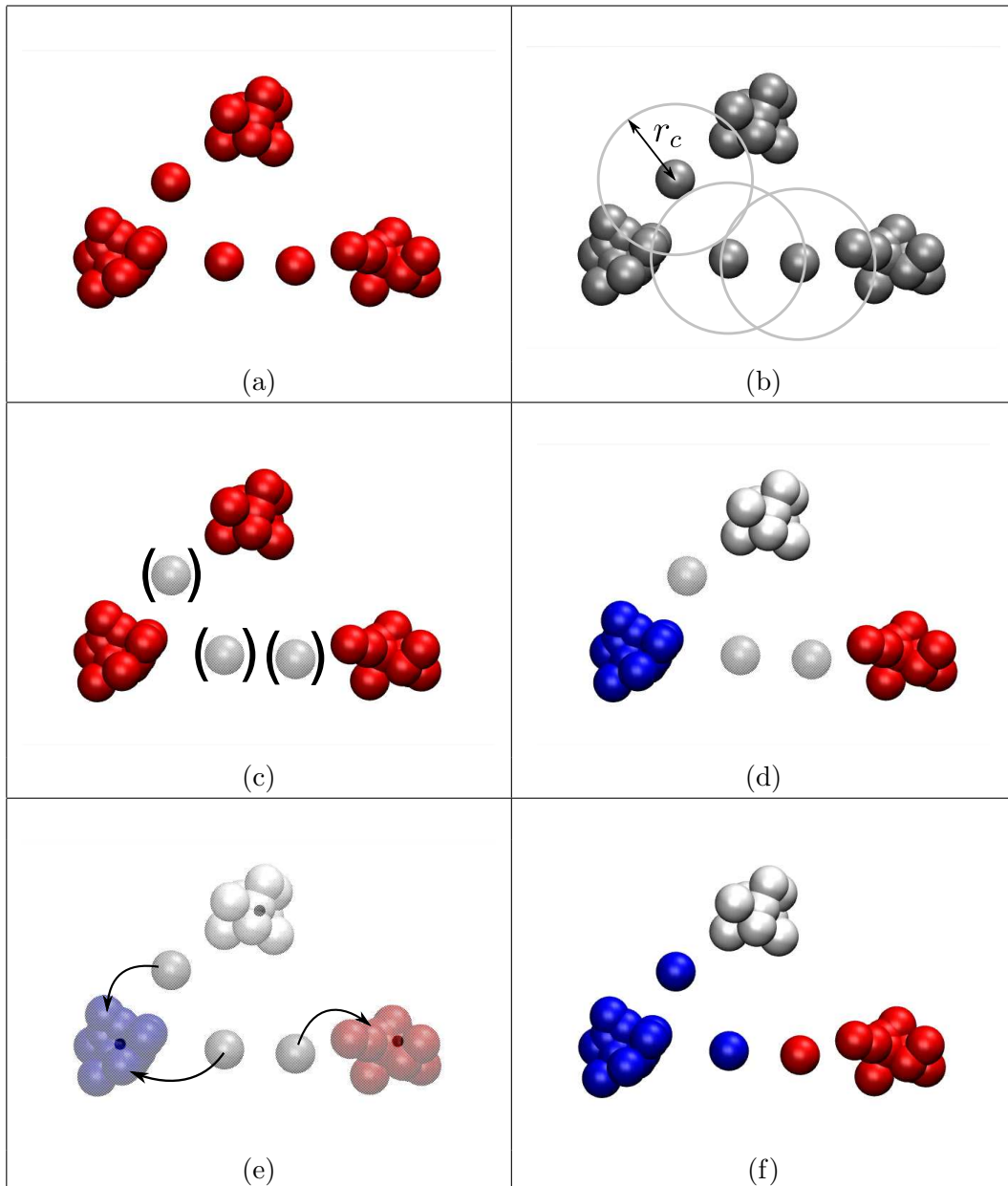
Figure 3.8: Separating merged clusters step by step. (a) Clusters have been merged by hopping particles. All particles in red are erroneously believed to belong to one cluster. (b) The search for particle neighbours is repeated. (c) Merging particles (grey spheres) have a small number of neighbours, they are temporarily excluded. (d) After identifying the particles' neighbours once again, new, separated clusters are set up. (e) Excluded particles are reintroduced and reassigned to the nearest cluster. (f) Procedure accomplished, yielding three disjoint clusters.

Steps 4 - Reassigning remaining particles to clusters.

In order to be as flexible as possible in the choice of the cutoff radius r_c, we opted for implementing a final check on the cluster sizes at that point. If, by accident, there are still remaining particles or small collections of particles which have not yet been assigned to one of the clusters, we label them with the ID of the cluster with the nearest centre of mass. The outcome of our efforts made to distinguish unambiguously between clusters becomes obvious when we reconsider the cluster population distribution (see Fig. 3.7, right panel). Peaks due to single particles and merged clusters have vanished, reflecting correctly the distribution of cluster sizes in the system.

From MD simulations we obtain a set of configurations which contain single-particle trajectories. Having performed Steps 1 to 4 for all configurations available we still need to ensure that the cluster IDs remain unique to each cluster in time as well.

Step 5 - Matching cluster IDs in time.

Remember that, for the sake of simplicity, we started our search for particle neighbours always with particle 1 and then continued up to particle N. Yet, in the diffusive regime of a clustering system we encounter a substantial number of particles hopping around and changing their cluster identities, which raises the following question: What if, in the course of the simulation, particles hop to other clusters? In this case, the IDs of clusters would be exchanged and we would lose track of the individual clusters in no time. This has to be avoided, since it is crucial for the analysis of dynamic properties of a cluster to ensure that the cluster identity is fixed at all points in time.

To overcome this problem, we can benefit from the assumption that, as long as we carry out the cluster analysis in the crystal phase, the centres of mass of the clusters are bound to their respective lattice sites. To be more specific, the root mean square displacement of the centres of mass, $\sqrt{\langle r_{\mathrm{cm}}^2(t) \rangle}$, does not exceed ten percent of the nearest-neighbour distance between clusters, d_{nn}, at any state point in the fcc region of the phase diagram,

$$\sqrt{\langle r_{\mathrm{cm}}^2(t) \rangle} \leq 0.10 \, d_{\mathrm{nn}}, \ \forall \ (\varrho, T)_{\mathrm{fcc}}. \tag{3.41}$$

It is thus possible to match each cluster CM with itself by identifying it with the nearest cluster CM in the next time step. In this way, it is guaranteed that, once a cluster ID has been chosen, we address the same cluster object in each configuration computed in the simulation.

By the successful accomplishment of Step 5 we finish the cluster analysis. It supplies us with the information necessary for the calculations of dynamic properties that are related to the motion of particles with respect to their cluster's CM or the cluster motion itself (for example, the VACF of the cluster CM or their MSD). It is worth summarising the relevant parameters used:

- r_c, the cutoff radius defining the sphere in which we search for neighbouring particles. In our work its optimal value was empirically found to be $r_c^* \approx 0.5$, which is smaller than the position of the first minimum in $g(r)$, $r_{\min}^* \approx 0.75$, for the GEM-4 potential.

- $n_c^{\min}$ and $n_c^{\max}$, the minimum and maximum cluster size, used to check whether two or more clusters have been erroneously merged by the algorithm.

- N_c, the number of lattice sites in the simulation box, necessary to check if separating the merged clusters has been successful.

The cluster analysis procedure is designed to treat a crystalline system. We want to stress, however, that it perfectly applies to disordered phases as well. In this case, we have to restrict the analysis to Steps 1 and 2, since neither the number of clusters is preserved nor are their centres of mass bound to lattice sites anymore.

3.3.2   An alternative cluster analysis method

The way of calculating cluster objects from single-particle trajectories presented in this work is not the only one one can think of. An alternative approach to it would be to start from the calculation of the single-particle potential energy surface. After the minima of the latter have been identified, particles are labelled with the IDs of the nearest potential energy minimum around, thereby forming the clusters. By the use of this method difficulties arising from merged clusters might be circumvented in an elegant manner. Still, the analysis relies on parameters such as the number of lattice sites or a definition of what to consider a sufficiently deep local minimum on the potential energy surface.

Chapter 4

Vibrations in cluster crystals

In recent years, *static* properties of cluster crystals have been extensively studied [3, 15, 20, 21]. In Chapter 1 we have presented the outcome of these studies. The *dynamic* properties [22, 23] of cluster crystals, however, have been considered to a lesser extent. One main part of our work is dedicated to the investigation of *vibrations* in cluster crystals. In an effort to understand how particles behave within a cluster on a very short-time scale, we reconsider the GEM-4 potential. From previous works [9], data of equilibrium system configurations for this representative member of the GEM-n, $n > 2$, class are available. These will serve as a starting point for our MC and MD simulations.

In Section 4.1 we give a detailed protocol of the simulations that we perform, which shall enable the reader to retrace the numerical part of our work with ease. Our results on single-particle and collective motion in cluster crystals will take centre stage in Section 4.2.

4.1 Simulation protocol

For the characterisation of the vibrational properties of a cluster crystal, we perform both MC and MD simulations for a GEM-4 system. We choose the fcc phase for our investigations because, for a GEM-4 system, the fcc crystal structure remains stable for all densities beyond a certain temperature-dependent threshold density (cf. Section 1.3). The explicit region of the GEM-4 phase diagram that we explore is illustrated in Fig. 4.1. At each state point we run simulations for ten independent realisations of the system and take the average of the dynamic quantities of interest (such as the VACF for example). In this way, we enhance the statistical significance of our results and reduce their possible dependence on initial conditions or on the cluster size distribution in the system.
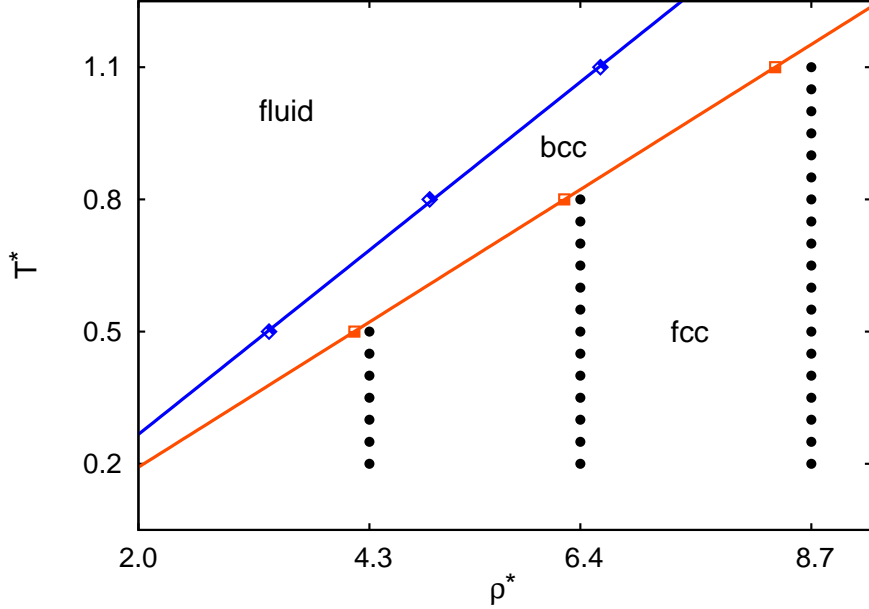
Figure 4.1: GEM-4 phase diagram. The blue and the red line depict the fluid-bcc and the bcc-fcc coexistence line, respectively. Both of these lines have been fitted to the data presented in [9], depicted by the blue and red squares. In our work, we investigate the vibrational properties in the fcc phase. Simulations are performed for densities $\varrho^* = 4.3$, 6.4, and 8.7 in the range of temperatures indicated by the full black circles.

ϱ^*	$\langle n_c \rangle$	a_{fcc}^*	N_c	N
4.3	8.824	2.0	256	2259
6.4	13.152	2.0	256	3367
8.7	17.883	2.0	256	4578

Table 4.1: Important parameters for setting up MC and MD simulations. We perform simulations for an fcc cluster crystal at three different densities, ϱ^*, for which the average cluster occupation number, $\langle n_c \rangle$, was obtained in the work of Mladek *et al.* [9]. The fcc lattice constant, a_{fcc}^*, is prescribed to the value predicted by DFT, the number of lattice sites in the system, N_c, is constant. Accordingly, the number of particles in the system, N, varies with density.

System setup

Before starting MC and MD simulations, we have to set up a cluster crystal corresponding to an equilibrium configuration at a given density ϱ. As mentioned in Chapter 1, these equilibrium configurations have been determined by Mladek *et al.* [9] for a large region of the GEM-4 phase diagram by the use of the DFT formalism. In this formalism the free energy functional, $\mathcal{F}$, is minimised with respect to the average cluster occupation number, $\langle n_c \rangle$. For our purposes, we take advantage of the data obtained from these calculations (see Tab. 4.1) and choose an equilibrium number of particles N in our system appropriate for each state point. The explicit value of the density-independent lattice constant, a, for the GEM-4 system is provided by GA- and DFT-calculations (cf. Chapter 1.2). To be more specific, $a^* \cong 2.0$ in the entire fcc region of the GEM-4 phase diagram.

With this information at hand, we set up a cluster crystal with four fcc unit cells per box side at a lattice spacing of $a^* = 2.0$, leading to $N_c = 4 \cdot 4^3 = 256$ lattice sites in a box of side length $L^* = 8.0$. For a given density we choose the appropriate number of particles from Tab. 4.1 and uniformly distribute $N_c \cdot \mathrm{INT}(\langle n_c \rangle)$ [1] of these particles onto the lattice sites. The $N - N_c \cdot \mathrm{INT}(\langle n_c \rangle)$ remaining particles are then assigned randomly to the lattice sites.

MC simulation runs

In the next step we perform MC simulations[2] to allow the cluster crystal, initially set up at zero temperature, to find its equilibrium distribution of cluster sizes, corresponding to the equilibrium degree of polydispersity in the cluster occupancy, at temperature T. The dependence of cluster size polydispersity on density and temperature has been described in [15]: according to this work, the width of the cluster size distribution changes, above all, with T, which is well reproduced in our MC simulations (see Fig. 4.2).

As soon as the cluster size distribution has reached equilibrium in the MC simulation runs, we can proceed with the MD simulation runs.

MD simulation runs

From MC simulations, we obtain configurations equilibrated in terms of the particle *positions* in the crystal. We now make use of NVT simulations, as described in

---

[1] Here, the function INT(x), familiar to any computational physicist, truncates the decimal digits of a real number x and returns the next lower integer n.

[2] The reason why we use MC simulations instead of MD simulations for the equilibration of the system has already been pointed out in Section 2.2.3. In the non-diffusive region of the fcc phase it is not possible to reach the equilibrium cluster size distribution within reasonable simulation length.
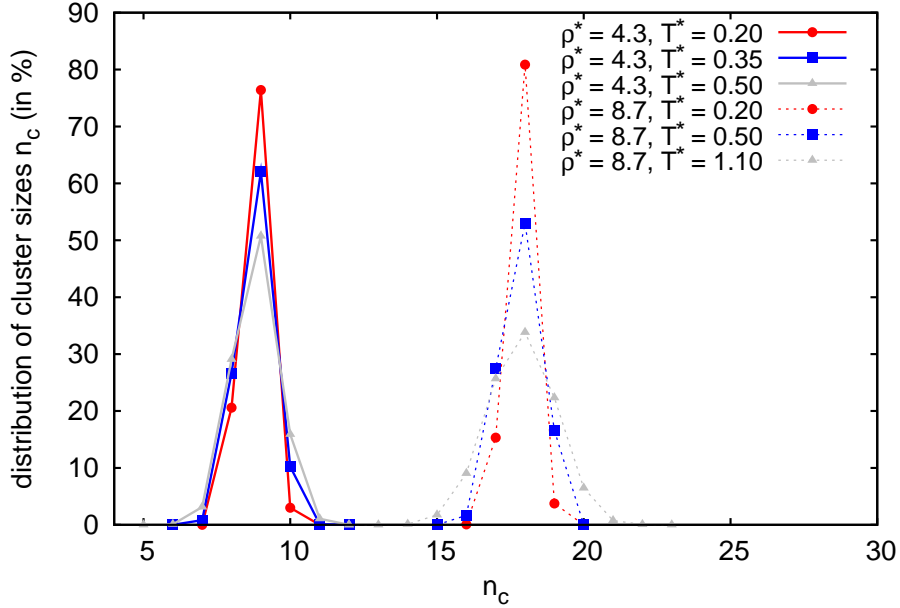
Figure 4.2: Distribution of cluster sizes at two different densities, $\varrho^* = 4.3$ and 8.7. The width of the distribution, a measure of the degree of polydispersity present in a cluster crystal, grows as the temperature, T^*, is increased.

Section 2.3.2, to equilibrate the particle *velocities* according to the Boltzmann velocity distribution, eq. (2.22), at the desired temperature T. Before starting the MD "production runs" (NVE simulations (cf. Section 2.3.1)) the simulation parameters that we employ have to be fixed. These are, for example, the time step, δt, the time interval of configuration printout, Δt, or the simulation length, $t_{\max}$. The choice of the values of the respective parameters primarily rests upon the quantities that we intend to calculate from the trajectories and the required numerical accuracy.

Aiming at characterising the spectrum of vibrations in a cluster crystal, the time step, δt, and the configuration printout interval, Δt, must be chosen such that particle oscillations can be resolved with sufficient precision in the VACF and enough simulation time steps, n, are available for the calculation of its Fourier transform (FT). In fact, the finest possible resolution in frequency, $\Delta\omega$, in the spectrum of the VACF is determined by the equation

$$n\Delta t\Delta\omega = 2\pi. \tag{4.1}$$

This relation is imposed by the formalism of the discretised FT and inverse FT of any time-dependent correlation function (see [25], Appendix D). These considerations lead us to the first type of production runs (see Tab. 4.2 – third column). These runs are characterised as relatively short MD simulations ("short" runs), with many system configurations written out for the ensuing post-processing analysis.

MD production run		"short"	"long"
time step	δt^*	0.02	0.02
configuration printout interval	Δt^*	0.02	500
number of simulation steps	n	8000	500 000
simulation length	$t_{\max}^* = n \cdot \delta t^*$	160	10 000
potential cutoff scheme		"cut & shift"	"cut & shift"
speed-up scheme		Verlet list	Verlet list

Table 4.2: Specific simulation parameters characterising the MD production runs (NVE simulations) used for i) calculating the VACF and its FT ("short" run), and ii) the normal mode analysis ("long" run). For explanations on potential cutoff and speed-up scheme see Sections 2.1.3 and 2.1.4.

We perform separate MD simulation runs for the normal mode analysis (NMA). Starting again from an MC-equilibrated system we run relatively long simulations, "long" runs (see Tab. 4.2 – forth column), in which particles are offered the possibility to hop and diffuse over several lattice sites. In this way, we are able to cancel out the influence of different cluster occupancy configurations in the crystal on the vibrational spectrum, by selecting system configurations sufficiently separated in time for the NMA.

Post-processing data analysis

For the short runs, the MC and MD simulations that we have just outlined are performed for ten different cluster crystal realisations at each state point, (ϱ, T). The difference in these realisations results from the random assignment of particles to cluster sites when setting up the system, and the stochastic development of particle positions in the MC equilibration run. For the calculation of the VACF and its FT from the short simulation runs, we average over these independent realisations.

Finally, we mention the great computational effort made in the NMA of the present clustering systems. For the highest density, $\varrho^* = 8.7$, for instance, a $(3N \times 3N) = (3 \cdot 4578) \times (3 \cdot 4578) = 13734 \times 13743$ dimensional matrix has to be diagonalised, a procedure that takes up to around 14 hours on an Intel Core 2 Duo CPU at 3.00 GHz, for 15 system configurations at each temperature.
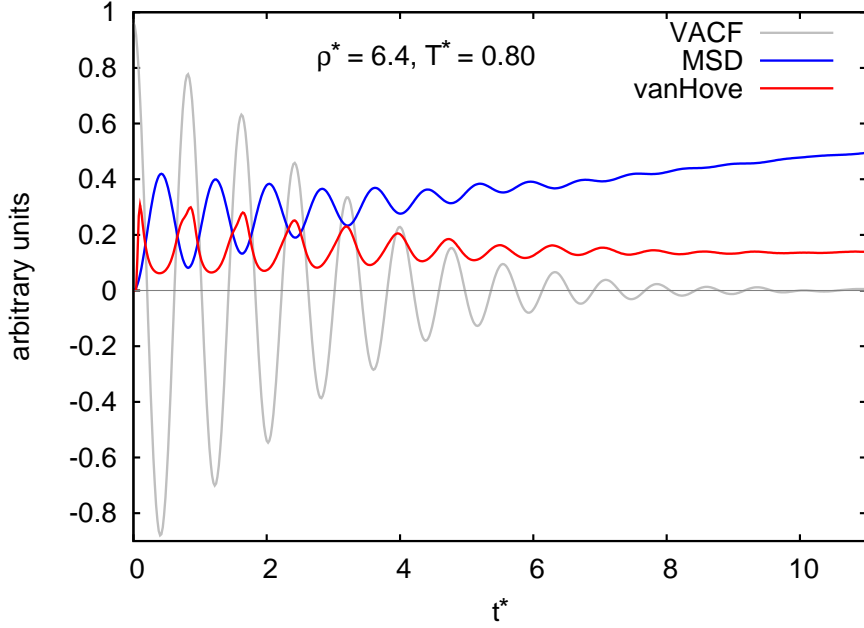
Figure 4.3: For short times, t^*, the VACF, the MSD and the van Hove correlation function of a cluster crystal exhibit oscillations of the same frequency.

4.2 Single-particle and collective motion in a cluster crystal

In Section 1.3.4 we briefly reported on the predictions on acoustic and optical branches in the phonon spectrum of a cluster crystal made by Likos *et al.* [2]. A connection between these two different kinds of phonon excitations, on the one hand, and collective and individual motion of particles in the system, on the other hand, has been established. In our work, we carry out more profound investigations on particle vibrations in cluster crystals in order to understand how these determine the shape of the vibrational density of states in the system.

First insight into the particles' motion is provided by a comparison of the oscillation frequencies of the VACF, the MSD and the van Hove correlation function (cf. Section 3.1.3) for short times (see Fig. 4.3). Interestingly, on this timescale all of these three dynamic quantities exhibit oscillations which share the essentially equal frequency. Obviously, such similarities point towards a common origin of the oscillations, to be found in the particles' motion. Indeed, in [22, 23] this particular behaviour of the MSD for short times was attributed to the *oscillatory motion* of particles *around the lattice sites*.

4.2.1   The spectrum of vibrations obtained from the VACF

Having a suitable cluster analysis tool (as the one presented in Section 3.3.1) at our disposal we are now able to take a further step in the description of vibrations in a cluster crystal. To understand how particles behave within a cluster, we will analyse the motion of individual particles and cluster centres of mass separately. This task necessitates the decomposition of the particle positions and velocities into components associated with the CM motion and components describing the motion of a particle relative to the cluster CM. The position and velocity of a cluster CM is given by

$$\boldsymbol{r}_{\mathrm{cm}} = \frac{1}{M} \sum_{i=1}^{n_{\mathrm{c}}} m_i \, \boldsymbol{r}_i = \frac{1}{n_{\mathrm{c}}} \sum_{i=1}^{n_{\mathrm{c}}} \boldsymbol{r}_i \tag{4.2}$$

$$\boldsymbol{v}_{\mathrm{cm}} = \frac{1}{M} \sum_{i=1}^{n_{\mathrm{c}}} m_i \, \boldsymbol{v}_i = \frac{1}{n_{\mathrm{c}}} \sum_{i=1}^{n_{\mathrm{c}}} \boldsymbol{v}_i \,. \tag{4.3}$$

Here, n_{c} indicates the instantaneous cluster size, $M = \sum_{i=1}^{n_{\mathrm{c}}} m_i$ is the cluster mass, and $\boldsymbol{r}_i$ and $\boldsymbol{v}_i$ are the positions and velocities of a cluster's particles. The second equivalence in eqs. (4.2) and (4.3) follows from our initial assumption that all particles have the same mass, $m_i = m$ (cf. Section 2.1.1). Dropping the index i, the relative coordinates and velocities of a particle with respect to the CM of its home cluster are given by

$$\boldsymbol{r}_{\mathrm{rel}} = \boldsymbol{r} - \boldsymbol{r}_{\mathrm{cm}} \tag{4.4}$$

$$\boldsymbol{v}_{\mathrm{rel}} = \boldsymbol{v} - \boldsymbol{v}_{\mathrm{cm}} \,. \tag{4.5}$$

Furthermore, as illustrated in Fig. 4.4, we decompose the relative particle velocity, $\boldsymbol{v}_{\mathrm{rel}}$, into a radial and a tangential part,

$$\boldsymbol{v}_{\mathrm{r}} = (\boldsymbol{v}_{\mathrm{rel}} \cdot \boldsymbol{e}) \, \boldsymbol{e} \tag{4.6}$$

$$\boldsymbol{v}_{\mathrm{t}} = \boldsymbol{v}_{\mathrm{rel}} - \boldsymbol{v}_{\mathrm{r}} \,, \tag{4.7}$$

where $\boldsymbol{e}$ is a unit vector pointing into the direction of $\boldsymbol{r}_{\mathrm{rel}}$,

$$\boldsymbol{e} = \boldsymbol{e}_{\boldsymbol{r}_{\mathrm{rel}}} = \frac{\boldsymbol{r}_{\mathrm{rel}}}{|\boldsymbol{r}_{\mathrm{rel}}|}. \tag{4.8}$$

The typical shape of the auto-correlation function for all velocity components is displayed in Fig. 4.5. For the range of temperatures we consider, the VACFs of the total and the relative particle velocity, $c_v(t)$ and $c_{v_{\mathrm{rel}}}(t)$, normalised to $c_v(0)$, are almost indistinguishable. The VACF of the cluster CM motion, $c_{v_{\mathrm{cm}}}(t)$, is characterised by a very small amplitude and a decay in time that is different from the one of the
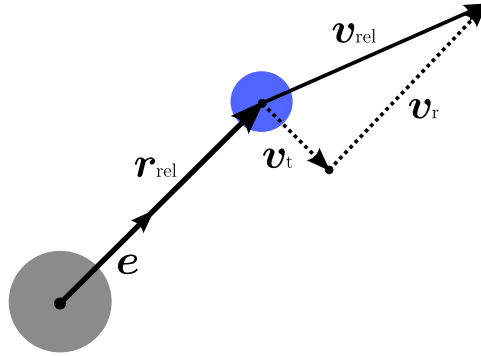
Figure 4.4: For the analysis of the VACF of different components of the particle velocity we decompose $\boldsymbol{v}_{\mathrm{rel}}$, defined in eq. (4.5), into a radial and a tangential part, $\boldsymbol{v}_{\mathrm{r}}$ and $\boldsymbol{v}_{\mathrm{t}}$. The large, full grey circle depicts the cluster CM, the smaller, full blue circle indicates a particle in the cluster.

other velocity components. The radial and the tangential velocity components show amplitudes that remarkably differ from each other. Their distinct amplitudes reflect the number of degrees of freedom associated with each of the components. While the radial motion of a particle can be described by its radial separation from the cluster CM, r_{rel} (one degree of freedom), the tangential motion is associated with two angles, ϑ and φ (two degrees of freedom). By virtue of the equipartition theorem [37] this leads to the average ratio $\langle v_{\mathrm{r}}^2 \rangle : \langle v_{\mathrm{t}}^2 \rangle = 1 : 2$. The two ensemble-averaged squared velocities, $\langle v_{\mathrm{r}}^2 \rangle$ and $\langle v_{\mathrm{t}}^2 \rangle$, are the $t = 0$ limits of their corresponding VACFs.

The vibrational spectrum obtained from the FT of the VACF of the total particle velocity, $\tilde{c}_v(\omega)$, displays the characteristic shape shown in Fig. 4.6. The spectrum is markedly dominated by a main peak, the position of which exclusively depends on density. Though very weak in amplitude, the rich peak structure in the remainder of the spectrum is no less remarkable (see the inset of Fig. 4.6). Indeed, the FT of the VACF of the relative particle velocity and of the cluster CM velocity, $\tilde{c}_{v_{\mathrm{rel}}}(\omega)$ and $\tilde{c}_{v_{\mathrm{cm}}}(\omega)$, reveal that the spectrum may be understood as consisting of two contributions, as illustrated in Fig. 4.7. The main peak is associated with *individual* motion of particles within the cluster, i.e. relative to the cluster CM, whereas the small peak structure is related to *coherent* motion of particles within a cluster, i.e. the motion of the cluster CM itself.

4.2.2   The vibrational density of states obtained from NMA

The calculation of the FT of the VACF of different velocity components is a very straight-forward approach leading to the spectrum of vibrations in a crystal. Nonetheless, it is worthwhile calculating the *vibrational density of states* (VDOS) by NMA
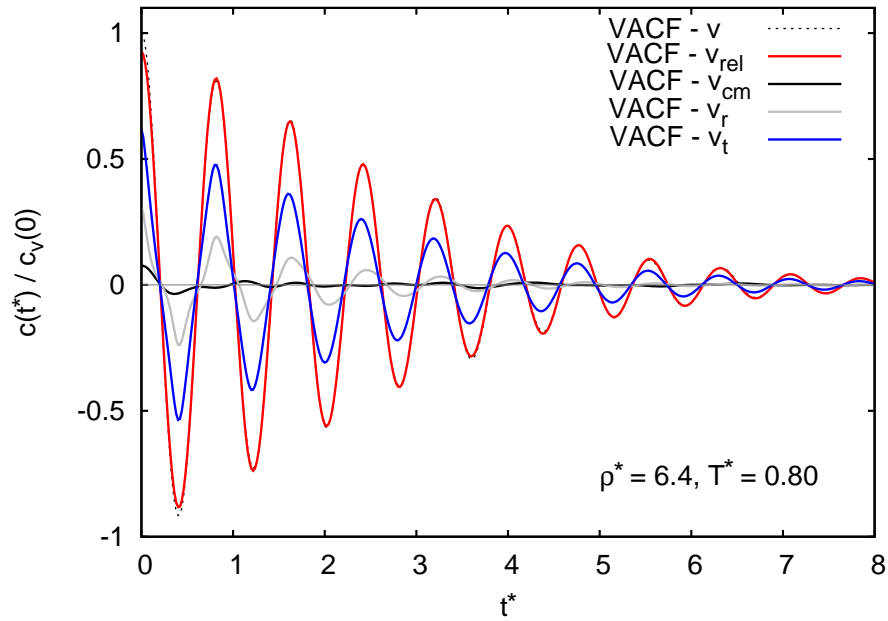
Figure 4.5: Auto-correlation function, $c(t^*)$, of different components of the particle velocity ($\boldsymbol{v}$, $\boldsymbol{v}_{\rm rel}$, $\boldsymbol{v}_{\rm cm}$, $\boldsymbol{v}_{\rm r}$, and $\boldsymbol{v}_{\rm t}$) as a function of time, t^*, normalised to $c_v(0)$.
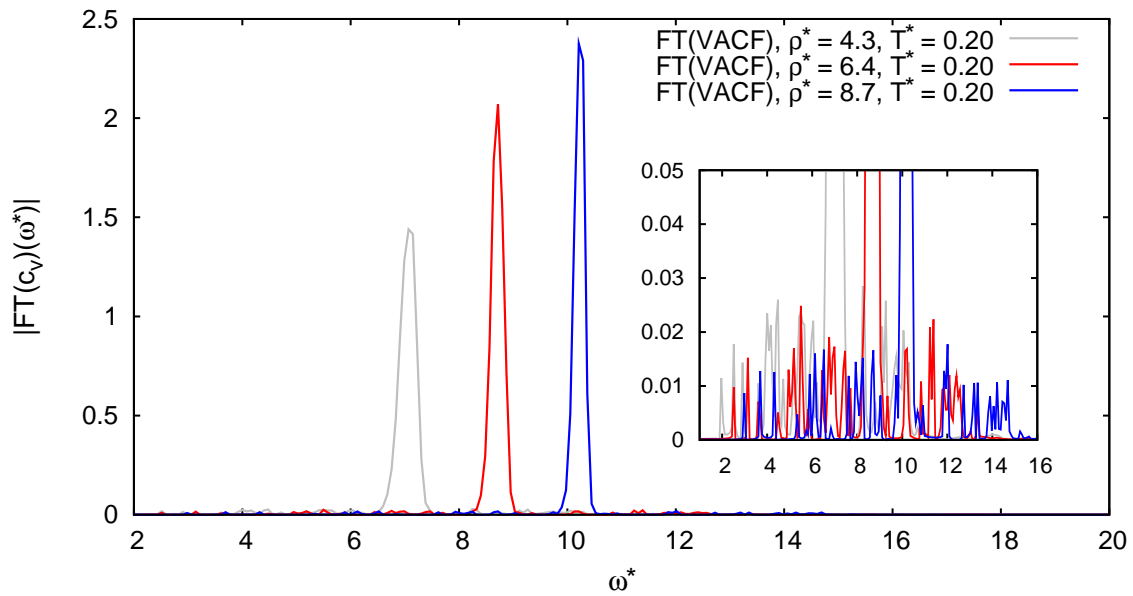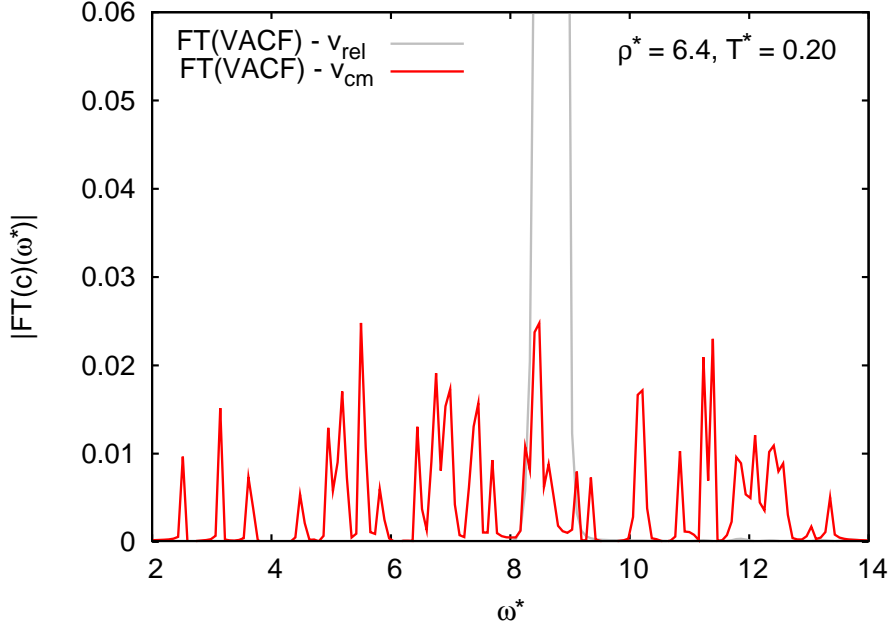

Figure 4.6: FT of the VACF, $\tilde{c}_v(\omega^*)$, as a function of ω^*, for different densities. The vibrational spectrum of a cluster crystal is characterised by a main peak and a rich variety of peaks of smaller amplitude (shown in the inset).

Figure 4.7: FT of the VACF of the relative particle velocity and the cluster CM velocity, $\tilde{c}_{v_{\mathrm{rel}}}(\omega^*)$ and $\tilde{c}_{v_{\mathrm{cm}}}(\omega^*)$. The spectrum separates into two parts: the main peak, associated with individual motion of particles within a cluster, and numerous small peaks, related to coherent motion of particles within a cluster.

as well, as it perfectly complements and confirms the picture of vibrations gained from the FT.

In general, the FT of a VACF contains more than just the information about vibrations. It also takes into account anharmonic effects that come into play at high temperatures and may serve as a measure of diffusion in the system (cf. eq. (3.19)). NMA, on the other hand, provides a route to an even more profound understanding of the vibrational spectrum. It yields not only the "true" VDOS, $\mathcal{D}(\omega)$, via eq. (3.38), but also the eigenvectors of the dynamical matrix of the system from which the participation ratio, $p(\omega)$, of particles on a normal mode can be calculated via eq. (3.39). In Section 3.2 we mentioned that the NMA requires a preceding minimisation of the total potential energy of the system. In Fig. 4.8 an untreated cluster crystal configuration is opposed to a minimised configuration, in which all particles of a cluster sit on top of each other.

From Fig. 4.9 we obtain a first impression of the VDOS and the origin of its different contributions which agrees very well with the one established via Fig. 4.7. Again, a large main peak dominates the spectrum and the surrounding peak structure persists. The participation ratio, $p(\omega)$, takes low values in the region of the main peak, indicating high localisation of normal modes. For the rest of the spectrum, $p(\omega)$
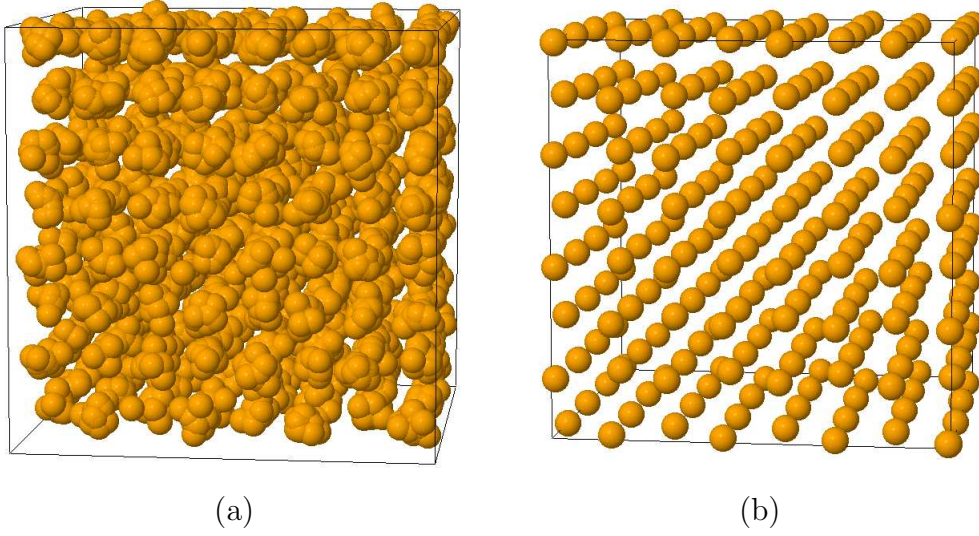
Figure 4.8: Simulation snapshots of a cluster crystal at $\varrho^* = 6.4$ and $T^* = 0.80$, (a) before minimising the total potential energy, and (b) after the minimisation procedure has been carried out (cf. Section 3.2.1). The minimum of the total potential energy in a cluster crystal corresponds to a configuration in which all particles of a cluster sit right on top of each other. In a polydisperse system, the positions of the clusters will not exactly coincide with the lattice sites of a perfect fcc crystal, since inter-cluster interactions depend on the (non-uniform) cluster sizes. These deviations are, however, too small to be discernible in (b).

takes considerably larger values, which suggests the presence of delocalised normal modes, i.e. modes which involve a large fraction of particles throughout the crystal. This type of vibrations corresponds to collective motion of particles, as anticipated in Section 4.2.1. In Fig. 4.10 the VDOS and the participation ratio are displayed for two different densities. These results give further evidence that the position of the main peak in the VDOS exactly coincides with the region of high normal mode localisation, corresponding to small values of $p(\omega)$.

As pointed out in Section 3.2.2, NMA also provides information on the displacement vectors $\boldsymbol{e}_\alpha^i$ of each particle i on a mode α. Thus, we may directly look at intra-cluster and collective modes in real space. From Fig. 4.11 the character of localised and delocalised modes becomes obvious. For frequencies ω chosen from the centre of the main peak in the spectrum, only particles belonging to one single cluster have a significant vector displacement on the corresponding normal modes (Fig. 4.11 (a), (b)). For frequencies located in the region of delocalised vibrations in the VDOS, on the other hand, particles all over the crystal contribute to the mode in a *collective* motion (Fig. 4.11 (c), (d)).

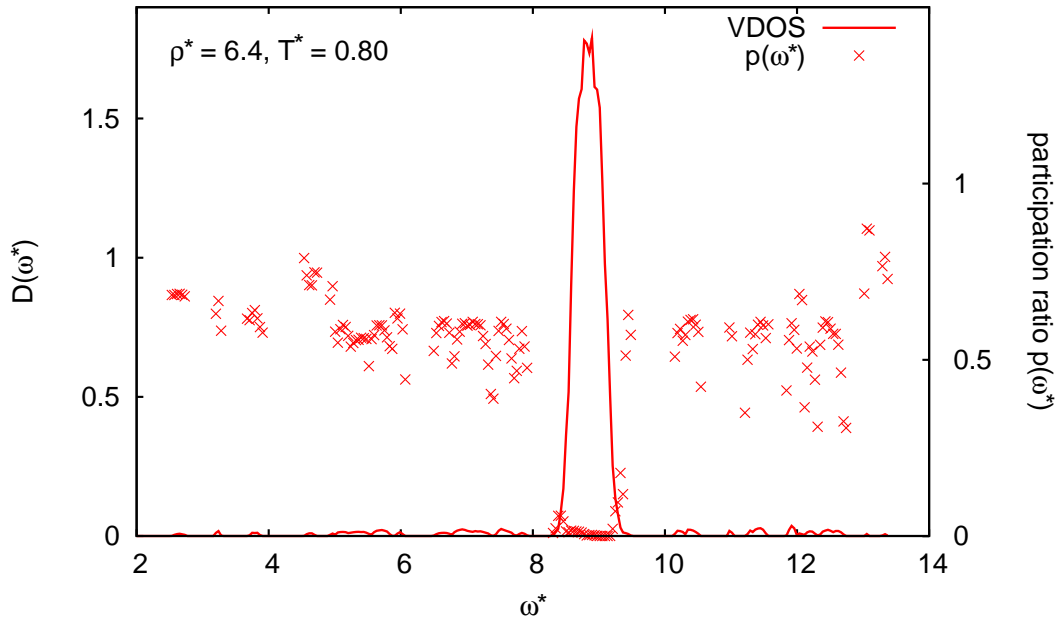A final remark concerns the shape of the main peak in the VDOS. Apart from the

Figure 4.9: VDOS, $\mathcal{D}(\omega^*)$, and participation ratio, $p(\omega^*)$, in a cluster crystal at $\varrho^* = 6.4$ and $T^* = 0.80$. In the region of the main peak $p(\omega^*)$ attains small values – normal modes are highly localised. For the remaining, relatively small peak structure $p(\omega^*)$ takes large values, which indicates that many particles contribute to these normal modes.
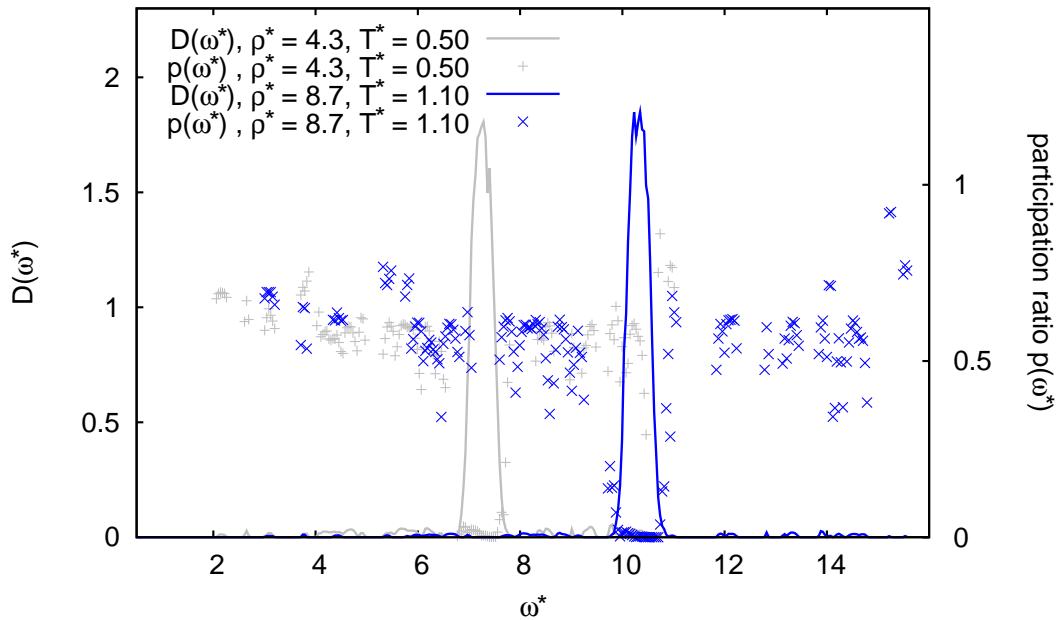

Figure 4.10: VDOS, $\mathcal{D}(\omega^*)$, and participation ratio, $p(\omega^*)$, for $(\varrho^*, T^*) = (4.3, 0.50)$ and $(\varrho^*, T^*) = (8.7, 1.10)$. Equivalently to the results shown in Fig. 4.9, the region of high localisation of normal modes coincides with the position of the main peak.
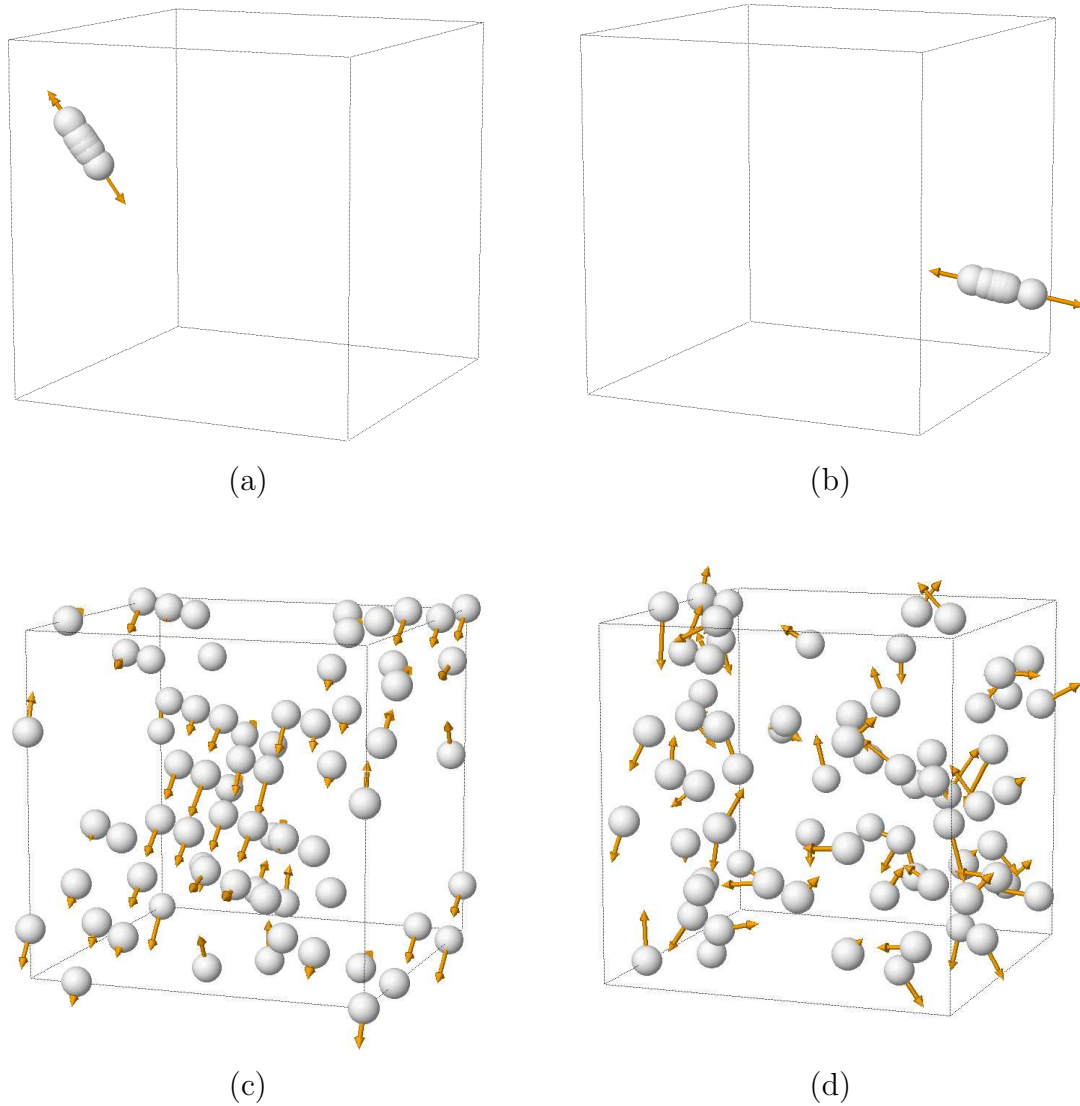
Figure 4.11: Localised and delocalised normal modes in real space for a cluster crystal at $\varrho^* = 6.4$ and $T^* = 0.80$. The orange vectors indicate the direction of the displacement $\boldsymbol{e}_\alpha^i$ of a particle i on a mode α. The vector length $|\boldsymbol{e}_\alpha^i|$ is arbitrarily scaled to enhance visibility. In (a) and (b) two localised normal modes corresponding to intra-cluster motion are shown; only particles with non-zero displacement, $|\boldsymbol{e}_\alpha^i| > 0$, are drawn. The frequencies and participation ratios are (a) $\omega^* = 8.54$, $p = 0.0012$ and (b) $\omega^* = 8.75$, $p = 0.0008$. In (c) and (d) two representative delocalised normal modes are displayed; only particles with a displacement $|\boldsymbol{e}_\alpha^i| \geq 0.14$ are shown. At each lattice site, all cluster particles sit on top of each other participating "collectively" in the oscillation of the cluster CMs. The frequencies and participation ratios are (c) $\omega^* = 2.72$, $p = 0.68$ and (d) $\omega^* = 12.43$, $p = 0.62$.
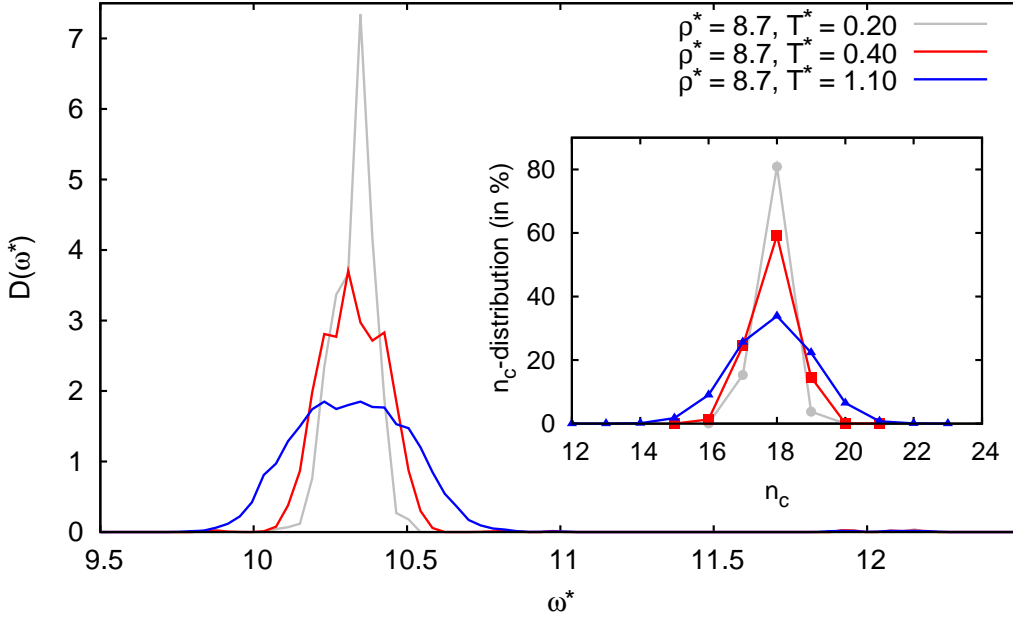
Figure 4.12: VDOS, $\mathcal{D}(\omega^*)$, for different temperatures at density $\varrho^* = 8.7$. The width of the main peak in the VDOS is correlated to the degree of polydispersity present in the cluster crystal. In the inset, the distribution of cluster sizes, n_c, is shown for the same density and temperatures.

fact that its position is independent of temperature we find a correlation between the width of the main peak and the degree of cluster size polydispersity present in the system, which can be seen from Fig. 4.12. The question arises how the distribution of cluster sizes can possibly influence the spectrum of vibrations in a cluster crystal. An explanation of this effect will be given in the following subsections.

4.2.3   Effectively harmonic one-particle motion

From Fig. 4.6 and Fig. 4.10 we conclude that the position of the main peak in the VDOS depends on density, ϱ. This behaviour can be understood within the concept of a harmonic approach to the single-particle motion, as suggested in [2]. In that work, the oscillation of a single particle with respect to all its peer particles in a cluster is considered, in order to derive an expression for the effective site potential, $\Phi_{\text{site}}(r_{\text{rel}})$. The latter is obtained from a Taylor series expansion of the single-particle potential energy around a lattice site and by exploiting the symmetry properties of a cubic lattice. $\Phi_{\text{site}}(r_{\text{rel}})$ then takes the form

$$\Phi_{\text{site}}(r_{\text{rel}}) = \Phi_{\text{site}}(0) + \left[\frac{(\langle n_c \rangle - 1)}{6} \sum_{\boldsymbol{R} \neq 0} \phi''(R) \right] r_{\text{rel}}^2. \tag{4.9}$$

ϱ^*	$\langle n_{\mathrm{c}} \rangle$	ω_0^* [VDOS]	ω_0^* [Φ_{site}]	ω_0^* [fit]
4.3	8.824	7.3	7.7	6.5
6.4	13.152	8.8	9.6	7.9
8.7	17.883	10.3	11.3	9.2

Table 4.3: Oscillation frequency, ω_0^*, of individual particle motion for different densities. Estimates of ω_0^* are obtained from the position of the main peak in the VDOS, eq. (4.11) derived from an expression for the effective site potential Φ_{site}, and a fit to the single-particle potential well calculated from MD simulation data.

Here, r_{rel} is given by eq. (4.4), $\boldsymbol{R}$ are the lattice site vectors, and the pair potential $\phi(r)$ can be any representative of the GEM-n, $n > 2$, class defined in eq. (1.1). From eq. (4.9) it follows that $\Phi_{\mathrm{site}}(r_{\mathrm{rel}})$ can be considered as a harmonic potential well in which the single particle is trapped. Thus, the corresponding effective, one-particle Hamiltonian, $\mathcal{H}_1$, [2] can be written in the form

$$\mathcal{H}_1 = \frac{p^2}{2m} + \frac{m\omega_0^2}{2} r_{\mathrm{rel}}^2, \tag{4.10}$$

where the two terms on the right-hand side represent the kinetic and the potential energy, respectively. Comparison of the prefactors of r_{rel}^2 in eqs. (4.9) and (4.10) allows the oscillation frequency to be expressed as

$$\omega_0 = \sqrt{\frac{(\langle n_{\mathrm{c}} \rangle - 1)}{3m} \sum_{\boldsymbol{R} \neq 0} \phi''(R)}. \tag{4.11}$$

Since the nearest-neighbours contributions dominate by far the sum in eq. (4.11), it is sufficient to take into account only the nearest-neighbour sites for the evaluation of this expression, i.e. 12 sites in an fcc lattice, a distance $d_{\mathrm{nn}}^* = a_{\mathrm{fcc}}^*/\sqrt{2} \cong \sqrt{2}$ apart from the central site. From Tab. 4.3 we see that, despite the substantial simplifications made when deriving the effective site potential, $\Phi_{\mathrm{site}}(r_{\mathrm{rel}})$, the results for ω_0 obtained from eq. (4.11) for different densities match the positions of the main peak in the VDOS (cf. Figs. 4.9 and 4.10) quite well. In addition, the density dependence of the VDOS can be easily explained: for $\langle n_{\mathrm{c}} \rangle \gg 1$ eq. (4.11) suggests a linear dependence of ω_0^2 on $\langle n_{\mathrm{c}} \rangle$, which translates into a linear scaling of ω_0^2 with ϱ,

$$\omega_0^2 \propto \langle n_{\mathrm{c}} \rangle \propto \varrho, \tag{4.12}$$

due to eq. (1.17) (see Fig. 4.13).

The above results encourage us to calculate the shape of the single-particle potential well from our simulation data. To this end, we simply evaluate the single-particle
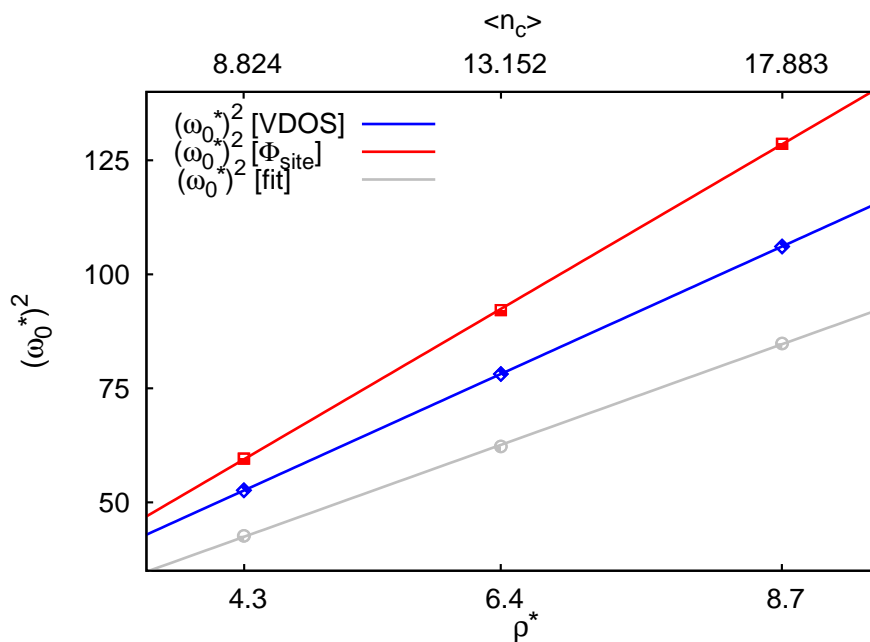
Figure 4.13: The square of the frequency of the main peak in the vibrational spectrum, ω_0^{*2}, scales linearly with $\langle n_c \rangle$ and ϱ^*. The data for ω_0^* obtained via the VDOS, eq. (4.11), and a fit to the single-particle potential well are displayed.
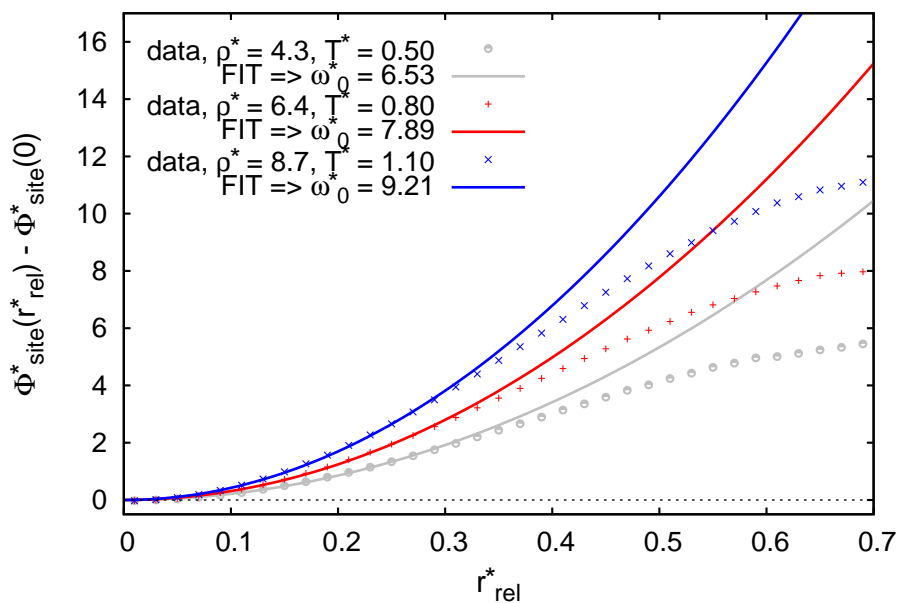

Figure 4.14: Single-particle potential well, $\Phi_{\mathrm{site}}^*(r_{\mathrm{rel}}^*)$, calculated from the single-particle potential energy within a cluster, for different densities. The centre of the well is approximately harmonic, thus a parabolic function of the form $\Phi_{\mathrm{site}}^*(0) + \omega_0^{*2}/2 \; r_{\mathrm{rel}}^{*2}$ can be fitted to the data between $r_{\mathrm{rel}}^* = 0$ and $r_{\mathrm{rel}}^* = 0.3$.
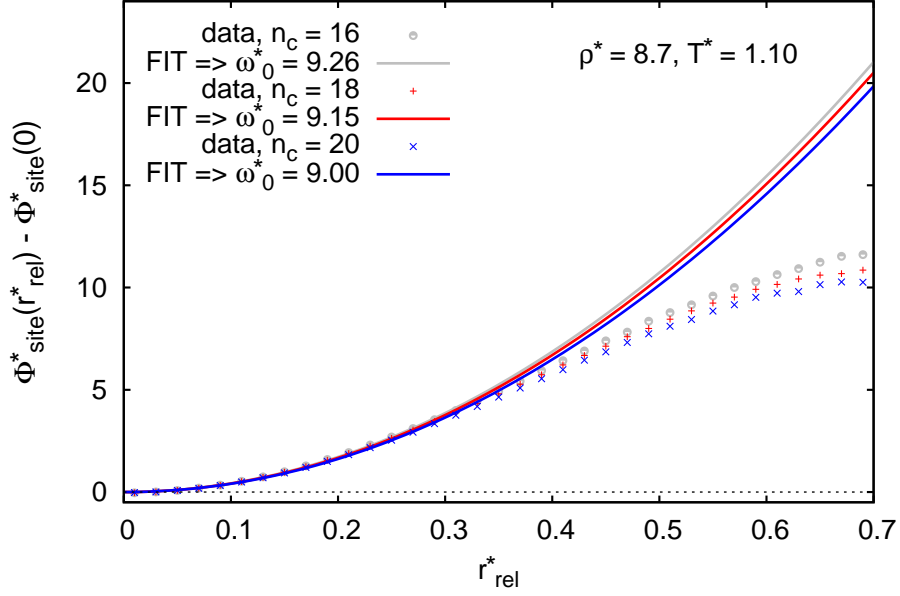
Figure 4.15: Single-particle potential well, $\Phi^*_{\text{site}}(r^*_{\text{rel}})$, for clusters of different size, $n_c =16$, 18 and 20. The fits in the harmonic central part of the potential wells reveal a very weak dependence of the oscillation frequency ω^*_0 on n_c.

potential energy at those separations from the cluster CM which occur naturally in the course of a particle's oscillation at finite temperature. We then fit a parabolic function to the effective site potential, $\Phi_{\text{site}}(r_{\text{rel}})$, calculated in this way, and extract its curvature $\omega_0^2[\text{fit}]$ (see Fig. 4.14). From the fifth column of Tab. 4.3 we see that the so-obtained frequencies $\omega_0[\text{fit}]$ match the ones calculated from the VDOS and via eq. (4.11) quite well.

Exploiting our simulation data even further we are also able to determine the shape of the effective site potentials for clusters of different occupancy n_c. The results are shown in Fig. 4.15 and suggest that the average curvature, ω_0^2, of the harmonic potential well depends only very weakly on n_c. Above all, ω_0^2 is determined by the contributions of the nearest-neighbour clusters to the potential energy, which correspond to the contributions to the sum in eq. (4.9). The force on a particle exerted by its neighbour particles within the same cluster is very small because of the functional shape of the GEM-4 potential, for which $\phi'(r \approx 0) \approx 0$. This can also be seen in Fig. 4.16, where two representative single-particle trajectories are illustrated. The particles' oscillatory motion is not deflected or distorted by the interaction with the other particles that occupy the same cluster.

The above considerations certainly give a qualitatively correct picture of how particles behave in a cluster. However, the deviations of $\omega_0[\text{fit}]$ and $\omega_0[\Phi_{\text{site}}]$ from
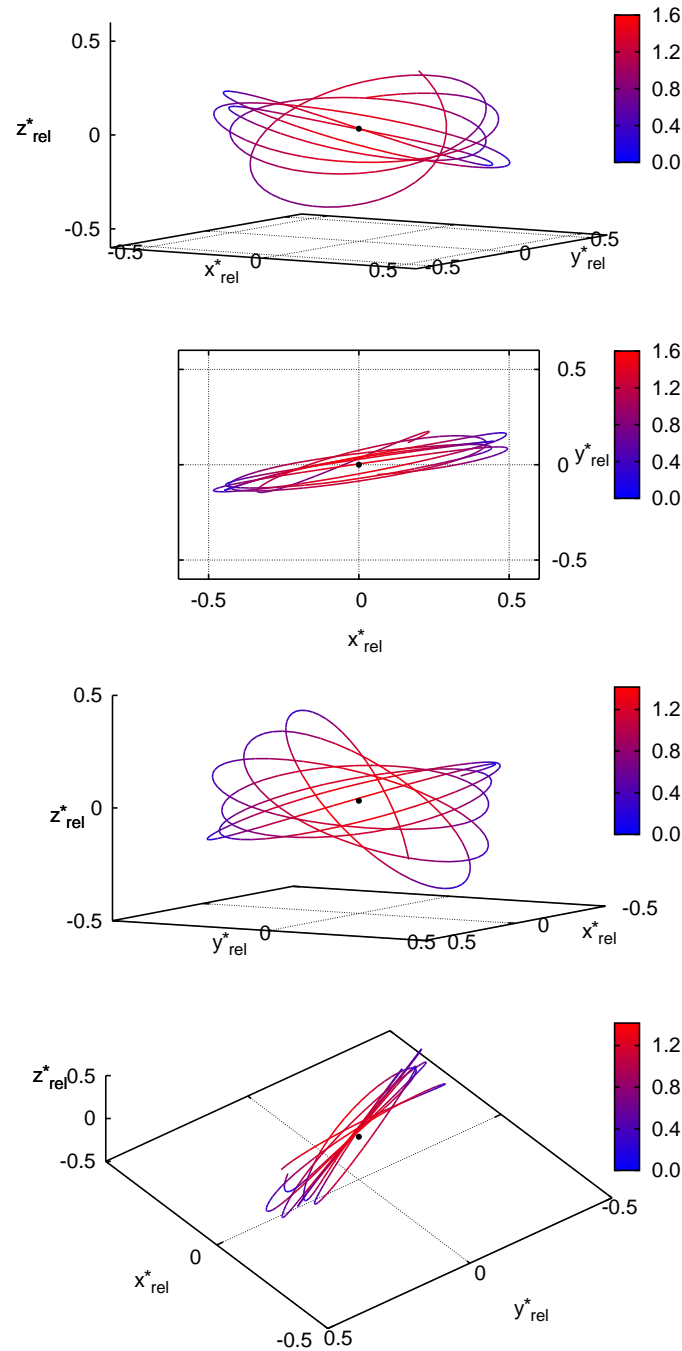
Figure 4.16: Two representative trajectories of a particle oscillating in its home cluster. Red and blue colour stand for high and low values of the modulus of the relative particle velocity, respectively (cf. colour palettes). We look at each trajectory from two different points of view, the first one perpendicular to the plane defined by the particle's motion around the cluster CM (first and third panel from the top), the second one lying in this plane (second and forth panel). The cluster CMs are depicted by small black spheres. The two trajectories occur as regular orbits around the cluster CM and the particles' motion is almost constrained to a plane (second and forth panel), indicating that there is little to no correlation to the motion of other particles in the same cluster.

ω_0[VDOS] in Tab. 4.3 indicate that the assumption of one-particle motion must not be fully trusted. One must not ignore the fact that, in reality, the dynamics of a clustered system takes place on a high-dimensional potential energy surface.

4.2.4 Phonon spectra of monodisperse and polydisperse cluster crystals

Recently, we became aware of further investigations on the phonon spectrum of cluster crystals that are currently under way [44]. Diagonalising the dynamical matrix in k-space in an analytical approach, these studies are expected to yield phonon dispersions which feature 3 acoustic and and $3(n_c - 1)$ optical branches, as has been mentioned in Section 1.3.4. Since only monodisperse systems are considered, i.e. crystals with fixed integer occupation number, n_c, for all lattice sites, all optical branches will be degenerate.

In an effort to render the results of [44] comparable to our data, we perform additional MD simulations for a monodisperse system at $\varrho^* = 6.32$ with a uniform, integer cluster size $n_c = 13$, and for a polydisperse system at the same density. In Fig. 4.17 we see that, in the monodisperse case, all intra-cluster normal modes are degenerate, with a single frequency, $\omega^* \cong 8.79$, which complies well with the analytical predictions [44]. For the polydisperse system, the degree of degeneracy in frequency is considerably reduced but not entirely removed. In fact, from the NMA we can also extract the number of modes of the same frequency ω_0, which provides information that the oscillation of all particles at a cluster site is associated with precisely three frequencies, one for each direction in real space. The three frequencies are n_c^{inst}-fold degenerate, with n_c^{inst} being the instantaneous occupation number of the cluster. As mentioned above, these frequencies are determined not by the particles that occupy this cluster themselves but by the nearest-neighbour clusters and their respective occupancy. Hence, there exist many different frequencies, contributing to the broad main peak in the VDOS of a polydisperse system, which originate from the numerous possible arrangements of clusters of different size around a central site.

As a final point it is worth mentioning that, even though the spectrum of normal modes that characterise intra-cluster motion in a polydisperse system differs from the monodisperse case, the basic principle that the phonon spectrum is separated into acoustic and optical branches remains valid. Remarkably, a signature of acoustic and optical branches can be observed even in the FT of the VACF.
This can be seen by calculating the ratio of the integral over the spectrum of the relative particle velocities, $\tilde{c}_{v_{\text{rel}}}(\omega)$, and the integral over the spectrum of the cluster
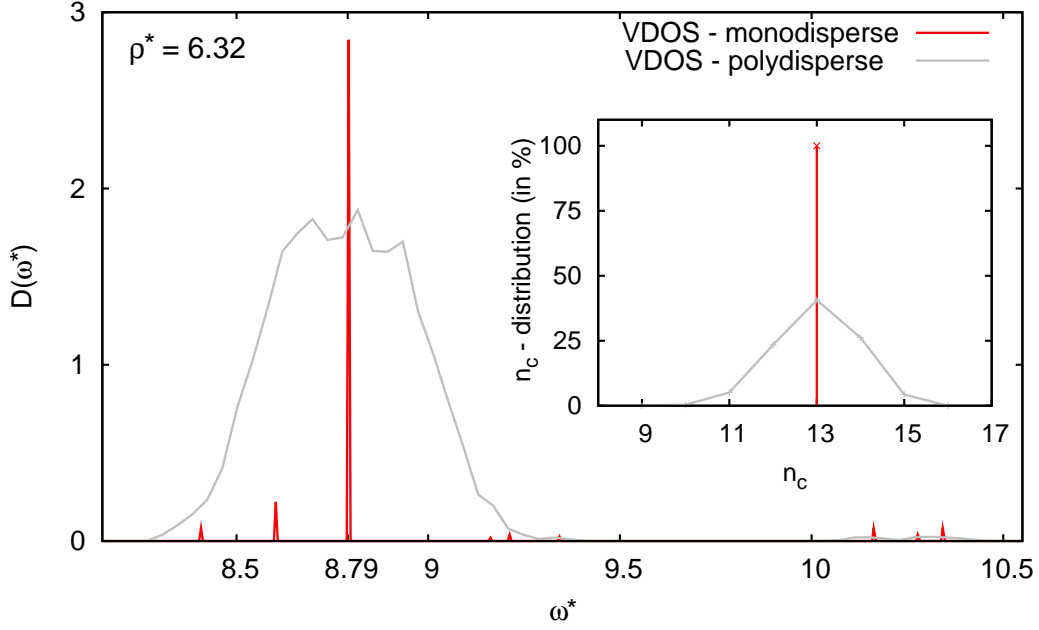
Figure 4.17: VDOS of a cluster crystal for systems of monodisperse and polydisperse cluster sizes n_c. In the monodisperse system, all frequencies of the main peak coincide at one single frequency, $\omega_0^* = 8.79$. The main peak and the small peaks in the VDOS of the monodisperse system have been scaled down by a factor of 65 and 6.5, respectively, to enhance visibility. In the inset, the cluster size distribution for the polydisperse and the monodisperse system is shown.

CM velocities, $\tilde{c}_{v_{cm}}(\omega)$ (cf. Fig 4.7). This ratio yields an estimate of $(\langle n_c \rangle - 1)$,

$$\frac{\int_0^\infty \tilde{c}_{v_{rel}}(\omega)\,\mathrm{d}\omega}{\int_0^\infty \tilde{c}_{v_{cm}}(\omega)\,\mathrm{d}\omega} \cong \frac{3\,(\langle n_c \rangle - 1)}{3} = (\langle n_c \rangle - 1). \tag{4.13}$$

Eq. (4.13) is fulfilled very well in the entire range of densities and temperatures that we consider, as shown in Tab. 4.4.

ϱ^*	$\langle n_{\mathrm{c}} \rangle$	T^*	$(\langle n_{\mathrm{c}} \rangle - 1)$
4.3	8.824	0.20	7.826
		0.35	7.855
		0.50	7.835
6.4	13.152	0.20	12.288
		0.50	12.108
		0.80	12.011
8.7	17.883	0.20	16.848
		0.80	17.040
		1.10	17.044

Table 4.4: Evaluation of eq. (4.13) for a range of densities and temperatures, yielding an estimate of $(\langle n_{\mathrm{c}} \rangle - 1)$.

Chapter 5

Diffusion in cluster crystals

The second part of the present work is dedicated to the description of diffusion processes in cluster crystals. Unlike perfect single-occupancy crystals, such systems exhibit an appreciable degree of long-time diffusivity by so-called particle *hopping* processes. Concerning this mechanism, two of the most interesting questions are *why* and *how* particles are given the possibility to move from one cluster to another.

In Section 5.1 we focus on the most important parameters that characterise our simulations. The results of our investigations of the diffusive behaviour of particles in a cluster crystal will be presented in Section 5.2.

5.1   Simulation protocol

To explore the features of diffusion processes in a cluster crystal we perform MD simulations in a GEM-4 system. For these simulations we choose those state points in the fcc region of the GEM-4 phase diagram (cf. Fig. 4.1) for which a measurable degree of diffusivity can be expected within reasonable simulation length (see Tab. 5.1). The procedure to set up ten independent realisations of a cluster crystal for every state point and the MC equilibration runs are identical to the ones presented in Section 4.1 (cf. Tab. 4.1).

MD simulation runs

As in the MD simulations that were run to characterise the vibrational spectrum of a cluster crystal, the choice of the configuration printout interval, Δt, depends on the timescale on which the physical processes of interest take place. Δt has to be small enough to resolve the particles' diffusive motion in the crystal, i.e. hopping processes between lattice sites. In contrast to the MD simulations in Chapter 4, we are free to choose the number of simulation steps, n, as we now need not calculate

ϱ^*	T^*	D^*
4.3	0.45	$9.978 \cdot 10^{-5}$
	0.50	$3.948 \cdot 10^{-4}$
6.4	0.65	$7.046 \cdot 10^{-5}$
	0.70	$2.109 \cdot 10^{-4}$
	0.75	$4.447 \cdot 10^{-4}$
	0.80	$1.119 \cdot 10^{-3}$
8.7	0.90	$8.007 \cdot 10^{-5}$
	0.95	$1.707 \cdot 10^{-4}$
	1.00	$3.283 \cdot 10^{-4}$
	1.05	$7.045 \cdot 10^{-4}$
	1.10	$1.272 \cdot 10^{-3}$

Table 5.1: MD simulations are performed in the region of the GEM-4 phase diagram where the fcc phase is stable at those state points (ϱ^*, T^*) for which diffusion can be observed within reasonable simulation length. The corresponding diffusion coefficient, D^*, obtained via eq. (3.21), is included in the table.

time-dependent correlation functions over long times. Therefore, we perform MD production runs (NVE simulations) that comply best to the abilities of the subsequent post-processing analysis, i.e. we generate data files of relatively small size which are easy to process. At every state point and for each of the ten system realisations we carry out ten successive simulation runs of that kind, in this way guaranteeing that our results are based on sufficiently rich statistics. In Tab. 5.2 a full characterisation of these MD simulations of medium length is given.

MD production run		"medium length"
time step	δt^*	0.02
configuration printout interval	Δt^*	10
number of simulation steps	n	20 000
simulation length	$t^*_{\max} = n \cdot \delta t^*$	400
potential cutoff scheme		"cut & shift"
speed-up scheme		Verlet list

Table 5.2: Specific simulation parameters characterising the MD production runs (NVE simulations), from which the diffusive behaviour of particles in a cluster crystal is determined.

Post-processing data analysis

Having finished the MD simulations for a given state point (ϱ, T) we analyse the generated system configurations by employing our cluster analysis algorithm (cf. Section 3.3.1). The latter provides the necessary information to which clusters the particles belong in the course of a simulation. This enables us to keep track of the diffusion of each particle in the system and to calculate relevant quantities (such as the distribution of the distances travelled by diffusing particles). These quantities are then averaged over the ten successive simulation runs mentioned above and ten independent system realisations, for each point in the diffusive part of the fcc region of the phase diagram (cf. Tab. 5.1).

In addition, for the characterisation of long-time diffusion in a cluster crystal, we take advantage of the "long" MD simulations performed in Chapter 4 (cf. Tab. 4.2), from which we calculate, for instance, the MSD and the van Hove correlation function.

5.2 Diffusive behaviour of particles in a cluster crystal

The most direct way to gain insight into diffusion processes in a cluster crystal is provided by the MSD. In Fig. 5.1 the MSD for a range of densities and temperatures is shown as a function of $\varrho^{1/2}t$. In [22, 23] this quantity was calculated for a GEM-8 system (cf. Fig. 1.1). Its behaviour was described as consisting of basically three different regimes in time: the quadratic increase of the MSD in t, called "ballistic" regime, takes place for very short times, i.e. when a particle is not yet interacting with surrounding particles. The following crossover regime ("plateau" regime) is associated with the temporary trapping of particles within the clusters. For long times, the diffusive regime is reached, for which the MSD scales linearly with t. In this region, every particle moves beyond the nearest-neighbour distance between the lattice sites, d_{nn}. From visual inspection of simulation snapshots we realise that, even though particles are able to diffuse in the crystal, the fcc lattice structure is maintained during the entire simulation. This situation is in sharp contrast to the one observed in single-occupancy crystals, where diffusion is impossible as long as there are no interstitials or vacant lattice sites. For the cluster crystal it means that, without the clusters being decomposed themselves, particles can jump between neighbouring clusters, a phenomenon which has been referred to as *"hopping"* [20]. These hopping processes lead to clusters that are composed of locally ever-changing particle populations, while the average cluster population, $\langle n_{\mathrm{c}} \rangle$, and the number of lattice sites in the system, N_{c}, remain unaffected [23].
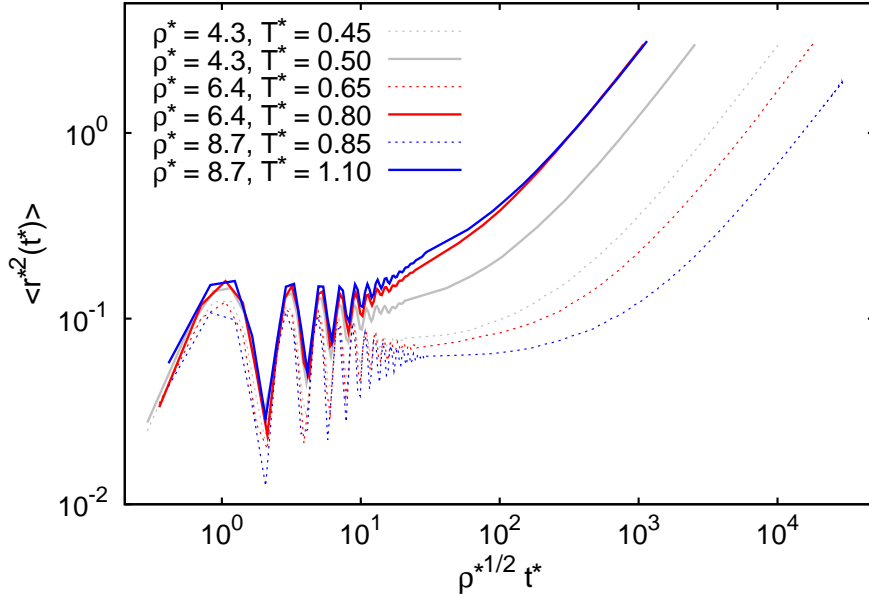
Figure 5.1: MSD of a GEM-4 cluster crystal for different densities and temperatures. The time axis is scaled with $\varrho^{*1/2}t^*$, in which case the short-time oscillations in the MSD have identical frequencies due to eq. (4.12). Essentially, three different regimes can be identified: the initial ballistic regime (not shown in the plot) is followed by a plateau regime for intermediate times ($10^0 \lesssim \varrho^{*1/2}t^* \lesssim 2 \cdot 10^1$), corresponding to the particles being trapped in the clusters. In this regime, the oscillations in the MSD are of the same frequency as in the VACF (cf. Fig. 4.3). For long times ($\varrho^{*1/2}t^* \gtrsim 2 \cdot 10^1$), the diffusive regime is reached, for which the MSD grows linearly with t.

5.2.1   Characteristic features of particle hopping

Aiming at a deeper understanding of this hopping mechanism we consider the van Hove self correlation function, $G_s(r, t)$, introduced in Section 3.1.3. Again, Moreno and Likos [23] discussed this quantity for the case of a GEM-8 system for the first time. In Fig. 5.2 $G_s(r, t)$ is shown for $\varrho^* = 4.3$ and $T^* = 0.50$ for different times t. The presence of a sequence of well-defined peaks, located at distinct r-values, points to the fact that the motion of particles between clusters is of discrete nature. With increasing time, the first peak in $G_s(r, t)$ decreases while peaks located at larger distances grow progressively, corresponding to particles moving away from their original home clusters. The black arrows in Fig. 5.2 indicate the distances to the n-th nearest neighbours in the fcc crystal structure, $\sqrt{n}d_{nn}$ ($n = 1, 2, 3, 4$). The second maximum in $G_s(r, t)$ at $r/d_{nn} \approx 1$ originates from the hopping of a particle to the first shell of nearest neighbours of its home cluster. The fact that $n = 2$ and $n = 3$ correspond to a local minimum and a local maximum of $G_s(r, t)$, respectively, suggests
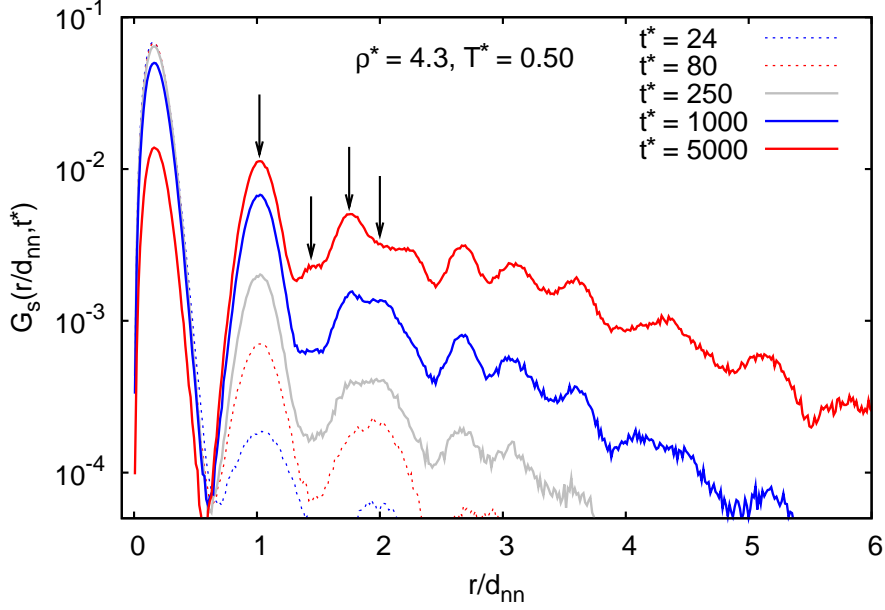
Figure 5.2: Van Hove self correlation function, $G_{\mathrm{s}}(r/d_{\mathrm{nn}}, t^*)$, at $(\varrho^*, T^*) = (4.3, 0.50)$ as a function of r/d_{nn} for different times t^*, as indicated in the key. With increasing time, peaks at larger distances arise in $G_{\mathrm{s}}(r/d_{\mathrm{nn}}, t^*)$ due to hopping of particles to neighbouring lattice sites. The black arrows indicate the distances to the first four nearest-neighbour shells, $r/d_{\mathrm{nn}} = \sqrt{n}$, with $n = 1, 2, 3, 4$.

a preferential directionality for the motion between neighbouring sites. This can be understood by considering a particle involved in two successive jumps connecting three distinct lattice sites. The four possible angles of such consecutive hops, $60°$, $90°$, $120°$, and $180°$ are associated with the distances $r/d_{\mathrm{nn}} = 1, \sqrt{2}, \sqrt{3}$, and $\sqrt{4}$, respectively (see Fig. 5.3). Thus, one concludes that during the hopping process angles of $120°$ are more likely to occur than angles of $90°$.

To push our analysis of particle hopping to an even deeper level, we consider the trajectories of hopping particles individually and introduce a thorough distinction between the following two categories of hopping events:

(i) *uncorrelated* hopping events, in which particles hop to one of the clusters located in the first shell of nearest-neighbours ($r/d_{\mathrm{nn}} = 1$) and are thermally equilibrated in this new cluster. This means that a subsequent hop takes place after a time longer than a certain threshold time t_{th}, which is of the order of the characteristic vibrational period of the intra-cluster particle oscillations described in Section 4.2.
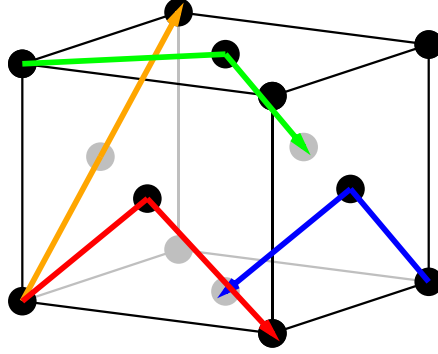
Figure 5.3: Unit cell of the fcc crystal structure. The full black and grey circles indicate fcc lattice sites. The coloured arrows correspond to possible consecutive jumps of particles to the n-th nearest-neighbour shell. Blue arrow: 60°, $r = d_{\mathrm{nn}}$. Red arrow: 90°, $r = \sqrt{2}d_{\mathrm{nn}}$. Green arrow: 120°, $r = \sqrt{3}d_{\mathrm{nn}}$. Orange arrow: 180°, $r = \sqrt{4}d_{\mathrm{nn}}$.

(ii) *correlated* hopping events, in which particles pass several clusters consecutively and are not thermally equilibrated in any of the passed clusters. Those particles can be identified by the condition that their residence time in each of these clusters is shorter than t_{th}.

In our work, a value of $t_{\mathrm{th}}^* = 3.2$ was empirically found to allow to reliably distinguish between uncorrelated and correlated hopping events.

In Fig. 5.4 we show the distribution of angles between consecutive jumps, $\mathcal{P}_{\mathrm{angle}}(\theta)$, of particles performing correlated hops (hops of category (ii)). It is important to note that the state points for which our data are presented are characterised by the approximately same diffusion coefficient and same ratio ϱ/T (cf. Tab. 5.1). For the evaluation of angles, θ, we use the relative vectors connecting the CMs of the different clusters that are visited, one after the other, by a hopping particle. To calculate $\mathcal{P}_{\mathrm{angle}}(\theta)$ we take into account the angles between each pair of consecutive jumps of a hopping particle. For instance, a particle that performs five hops will contribute four angles to the distribution. While confirming the relative preference of angles of 120° to angles of 90°, Fig. 5.4 reveals the occurrence of a global maximum in the angle distribution at 180°. This maximum gives evidence that, if particles hop more than once, they preferentially keep moving in the direction defined by their initial momentum when leaving their home cluster. We note that this feature cannot be detected by mere inspection of $G_{\mathrm{s}}(r,t)$. Further, we emphasise that this effect, while being almost independent of temperature within the range of state parameters explored in this work, is even more pronounced for higher densities, since the momentum required to overcome the potential barrier grows, together with the barrier height itself, with ϱ.
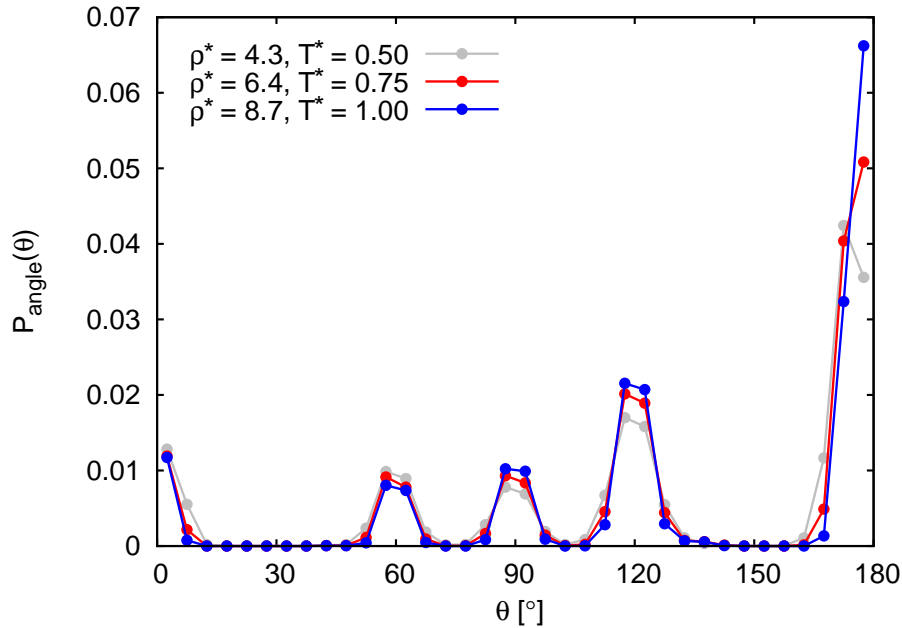
Figure 5.4: Distribution of angles between consecutive jumps, $\mathcal{P}_{\mathrm{angle}}(\theta)$, of particles performing correlated hops (hops of category (ii), see text). Data are shown for three different state points that share the essentially same diffusion coefficient and same ratio ϱ^*/T^* (cf. Tab. 5.1). With increasing density, the probability of hopping at angles of 180° becomes higher, as the momentum of a particle required to overcome the potential barrier grows with density. The height of the error bars in our data is comparable to the symbol size. $\mathcal{P}_{\mathrm{angle}}(\theta)$ is normalised such that its integral over the full range of angles is equal to 1.

Another interesting aspect concerning the hopping mechanism is how far hopping particles are able to travel through the crystal until they are trapped again and thermally equilibrated in another cluster. To find an answer to this question, we calculate the following two quantities: first, the *distribution of accumulated distances*, $\mathcal{P}_{\mathrm{acc}}(r)$, which measures how often hopping particles jumps, counting also distances accumulated by a particle that jumps back to its home cluster. Second, the *distribution of net hopped distances*, $\mathcal{P}_{\mathrm{net}}(r)$, which provides information on how far particles can propagate in the crystal, starting from their initial cluster. The travelled distances are given by the moduli of the relative vectors between the CMs of the clusters that are visited. For the calculation of the two distributions we take into account both categories (i) and (ii) of hopping events.

In Fig. 5.5 the distribution of accumulated distances, $\mathcal{P}_{\mathrm{acc}}(r)$, for different state points is shown. These results provide evidence that particles are able to perform hops over a wide range in the number of visited clusters. We note that it is, however, not possible to describe the envelope of the maxima of $\mathcal{P}_{\mathrm{acc}}(r)$ by a single exponential
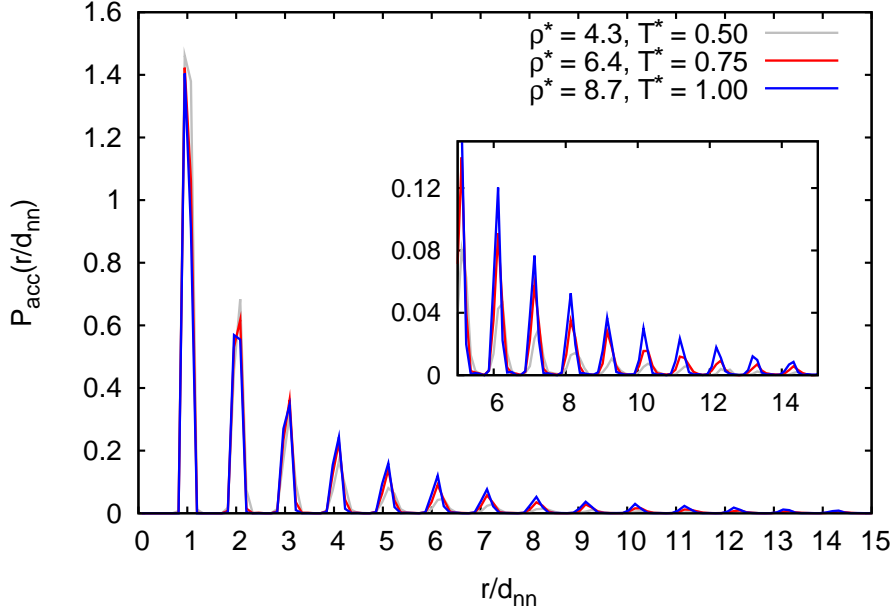
Figure 5.5: Distribution of accumulated distances, $\mathcal{P}_{\mathrm{acc}}(r/d_{\mathrm{nn}})$, taking into account category (i) and (ii) of hopping events (see text), for three different state points. From the inset we see that higher numbers of jumps per hopping particle become more probable with growing density. $\mathcal{P}_{\mathrm{acc}}(r/d_{\mathrm{nn}})$ is normalised such that its integral over the full range of distances is equal to 1.

function or a simple inverse power law. A weak dependence of $\mathcal{P}_{\mathrm{acc}}(r)$ on density can be seen from the inset of Fig. 5.5. The fact that larger-distance peaks grow with increasing ϱ corroborates the tendency mentioned already when discussing Fig. 5.4: the higher the potential barriers that must be overcome to break out of a cluster, the higher is the momentum of a hopping particle and the farther it can hop until it finally gets trapped again. As pointed out before, at the state points considered in Fig. 5.5, the different values of T compensate for the larger potential barriers at higher ϱ such that the diffusion coefficient, D, takes the approximately same values. Nevertheless, as the ability of a particle to gain momentum is triggered by temperature, it is possible to observe a weak dependence of $\mathcal{P}_{\mathrm{acc}}(r)$ on T for fixed density as well. The T dependence is, however, considerably smaller compared to the dependence on ϱ and therefore negligible.

The distribution of net distances, $\mathcal{P}_{\mathrm{net}}(r)$, evaluated for both category (i) and (ii) of hopping events, is shown in Fig. 5.6. $\mathcal{P}_{\mathrm{net}}(r)$ lends itself very well to a comparison with the long-time van Hove self correlation function (cf. Fig. 5.2). The first peak of the distribution at $r/d_{\mathrm{nn}} = 1$ corresponds to single hops of particles to nearest-neighbour clusters. The side peak observed between $r/d_{\mathrm{nn}} = 1$ and $r/d_{\mathrm{nn}} = 2$ for
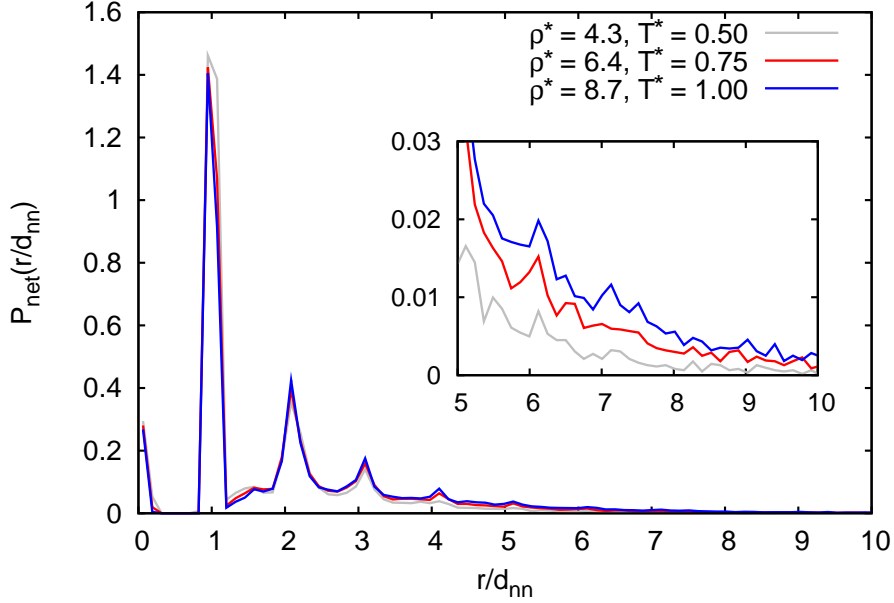
Figure 5.6: Distribution of net distances, $\mathcal{P}_{\mathrm{net}}(r/d_{\mathrm{nn}})$, travelled by hopping particles, for three different state points. The dominant peaks, located at multiple integers of the nearest-neighbour distance, are associated to jumps at a preferred angle of 180°. The small peak between $r/d_{\mathrm{nn}} = 1$ and $r/d_{\mathrm{nn}} = 2$ originates from consecutive hops at angles of 90° and 120°. Note the small probability of returning to the initial cluster, reflected by a small peak at $r/d_{\mathrm{nn}} = 0$. In the inset, an enlarged view of the distribution at large distances is shown to highlight the dependence on density. $\mathcal{P}_{\mathrm{net}}(r/d_{\mathrm{nn}})$ is normalised such that its integral over the full range of distances is equal to 1.

all densities, is due to consecutive jumps of both angles of 90° and of 120°. The larger-distance peaks, located at multiples of d_{nn}, originate from hopping particles of higher momentum that tend to hop through the crystal at a preferred angle of 180° (cf. Fig. 5.4). This behaviour can also be seen in the correlation of angles between consecutive jumps and the net distance travelled, shown in Fig. 5.7. Despite considerable scattering of possible angles for all distances (Fig. 5.7 (a)), this correlation confirms the aforementioned tendency to conserve the direction of the initial momentum for hopping particles that travel farther away from their home cluster (Fig. 5.7 (b)). In Fig. 5.8 two representative trajectories of hopping particles are illustrated. The left panel shows a particle's hopping path connecting many lattice sites throughout the crystal. The right panel shows a particle hopping to the fourth nearest-neighbour shell.

A possible way of interpreting our results on how far particles can travel in a cluster crystal is to put them in the context of different kinds of diffusion mechanisms present in such a system. We presume that, in a cluster crystal, there might exist two
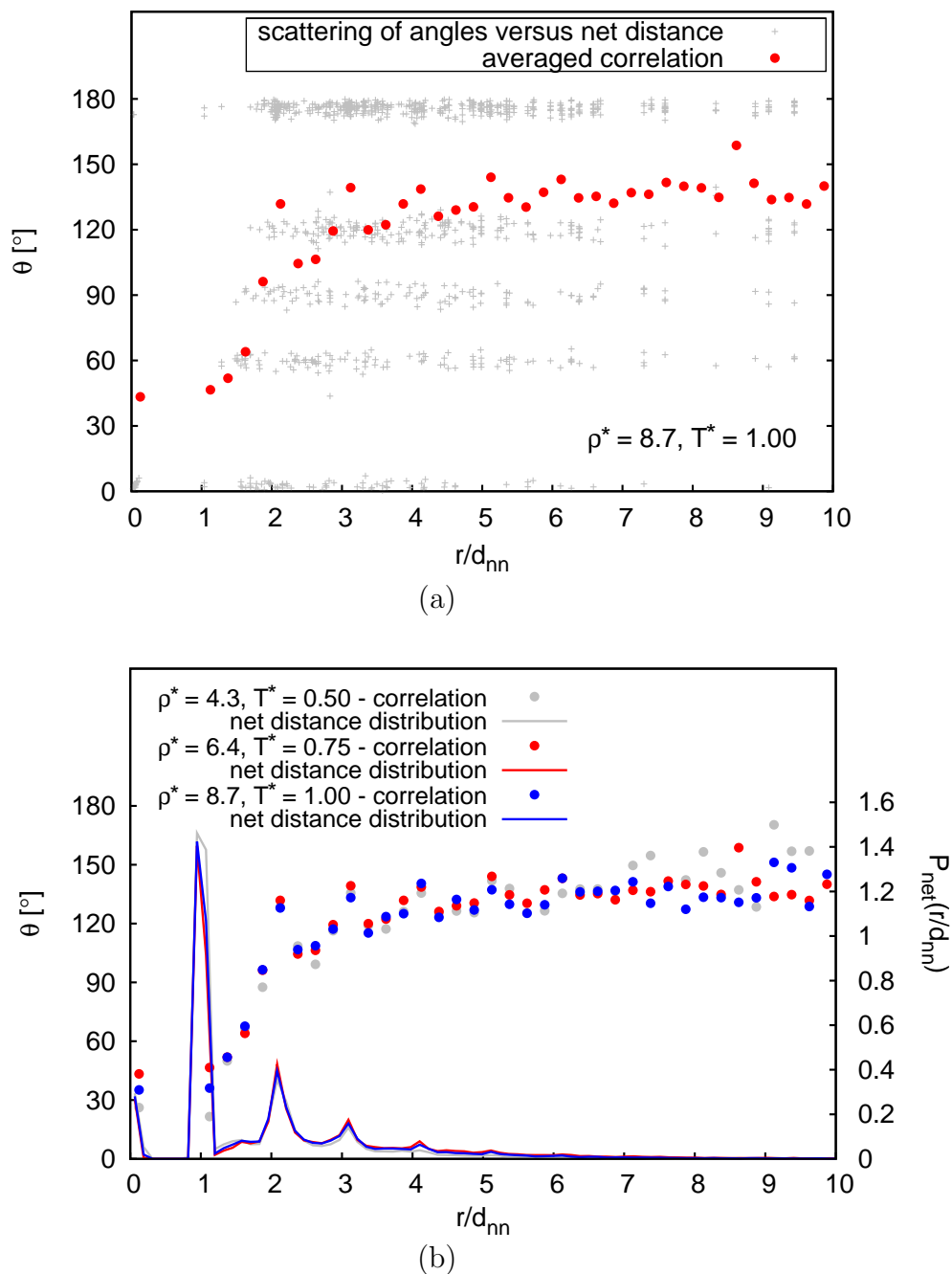
(a)

(b)

Figure 5.7: Correlation of the angle between consecutive jumps, θ, and the net distance travelled by a hopping particle. In (a) the scattering of angle versus net distance is compared to the correlation between angle and net distance obtained from averaging the angle over many hopping particles. For all net distances, in principle all angles (concentrated around 60°, 90°, 120°, and 180°) are possible. Nevertheless, the averaged correlation reveals a preference of angles of 180° for large net distances. In (b) the angle-distance correlation is shown for three different state points. For comparison, the distribution of net distances, $\mathcal{P}_{\mathrm{net}}(r/d_{\mathrm{nn}})$, of Fig. 5.6 is redrawn.
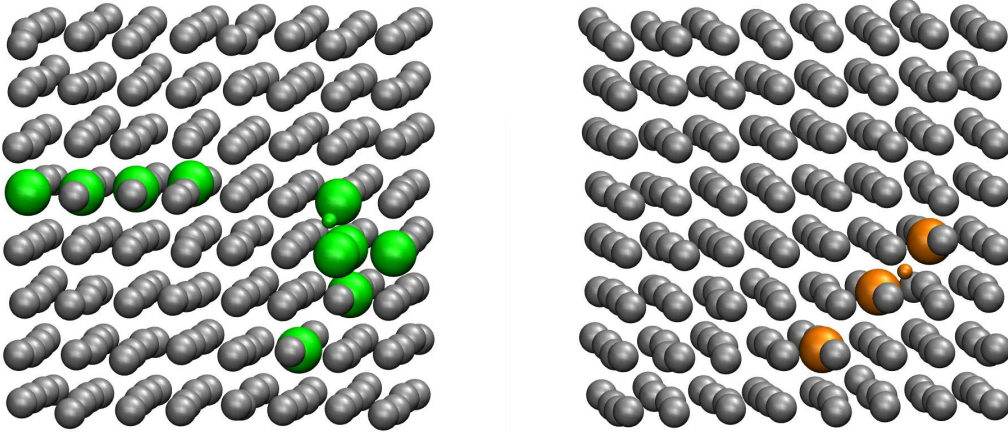
Figure 5.8: Two representative trajectories of particles performing correlated hops. The real clusters, each of them consisting of many particles, have been replaced by grey spheres located at the cluster CMs which occupy the positions of an fcc lattice. The hopping particles are drawn as small, coloured spheres. Coloured large spheres represent clusters visited by the particle on its trajectory. Left panel: hopping over large distances, involving ten clusters ($r_{acc}/d_{nn} = 9$). On its path, the hopping particle leaves the periodic simulation cell on the right edge and re-enters on the left side. Right panel: short-distance hopping, involving only three clusters ($r_{acc}/d_{nn} = 2$).

different kinds of diffusion: hopping and "effectively ballistic" motion of particles[1]. The first one corresponds to particles that perform uncorrelated hops from one cluster to another, the second one is associated to particles diffusing through the crystal in a correlated way, virtually irrespective of its lattice structure. Similarly, in [22] the question was raised *"whether hopping amounts to local particle moves or takes the form of diffusive migration of particles across macroscopically large distances"*. In the distribution of net distances, $\mathcal{P}_{net}(r)$, we see pronounced peaks for a broad range of distances. While the first peak, corresponding to uncorrelated hops, is especially marked, the heights of the larger-distance peaks decrease monotonically, but still contribute significantly to the overall distribution. To measure the relative contributions of the different categories of hops to the diffusion coefficient, D, we split the range of distances into three sections, corresponding to hops back to the initial cluster ($r/d_{nn} < 0.5$), uncorrelated hops to nearest-neighbour clusters ($0.5 \leq r/d_{nn} \leq 1.25$) and correlated hops over a sequence of clusters ($r/d_{nn} > 1.25$). Then, we calculate the integrals (I_{back}, I_{uncorr}, and I_{corr}) over $\mathcal{P}_{net}(r)$ for these r-ranges. Tab. 5.3 contains the results of these calculations for the same three state points as displayed in Fig. 5.6. We see that both categories (i) and (ii) of hopping events contribute signif-

---

[1]We thank D. Frenkel and B. M. Mladek for enlightening discussions on this topic.

ϱ^*	T^*	I_back	I_uncorr	I_corr
4.3	0.50	0.06	0.52	0.42
6.4	0.75	0.05	0.45	0.50
8.7	1.00	0.05	0.42	0.53

Table 5.3: To measure the relative contributions of hopping events of categories (i) and (ii) to the diffusion coefficient in a cluster crystal, we split the r-range of the distribution of net distances, $\mathcal{P}_\text{net}(r)$, (cf. Fig. 5.6) into three sections: $(r/d_\text{nn} < 0.5)$, $(0.5 \leq r/d_\text{nn} \leq 1.25)$, and $(r/d_\text{nn} > 1.25)$. Then we calculate the integrals (I_back, I_uncorr, and I_corr) over $\mathcal{P}_\text{net}(r)$ in these ranges.

icantly to $\mathcal{P}_\text{net}(r)$. We think that this provides the first evidence of the existence of the two diffusion mechanisms conjectured above.

5.2.2 Relaxation of cluster occupancy fluctuations

We now focus on the physical mechanisms that are responsible for the particle hopping processes. In [22] it was stated that, in a stable, polydisperse cluster crystal, incessant hopping processes must exist to maintain the mechanical stability of the crystal by guaranteeing the equality of the time-averaged site occupancy, $\langle n_\text{c} \rangle$, for all lattice sites. This leads to perceiving particle hopping processes as a relaxation mechanism which equilibrates fluctuations in the cluster occupancy. This approach can be confirmed by a comparison of the cluster size distributions of clusters from which hopping particles are kicked out and of clusters by which these particles are absorbed (or, caught) again at the end of their hopping path. For the sake of brevity, we shall refer to these distributions as "kicking" and "catching" distributions in the following.

From Fig. 5.9 we see that the kicking and the catching distributions are shifted to the right and to the left with respect to the equilibrium cluster size distribution, respectively. On the one hand, this provides evidence that indeed particles belonging to large clusters are more likely to leave their home cluster than particles occupying small clusters. On the other hand, the overlap between the kicking and the catching distribution is still considerable, meaning that the reverse situation, i.e. particle hopping from small to large clusters, is less probable but not impossible. Thus, the tendency to relax an unbalanced cluster occupancy is superposed by substantial occupancy fluctuations in which particles start hopping from their cluster at random, without being induced by any external influence.

In Fig. 5.10 the single-particle potential energy, $\mathcal{U}_{(1)}$, of two tagged hopping particles is followed before, during, and after the particles hop to another cluster, on

two different timescales. The upper panel shows $\mathcal{U}_{(1)}$ over long times covering several hundreds of vibrational periods of the particles' intra-cluster oscillation. Before the hopping event takes place, a progressive increase of the particle's average potential energy is observed. In the lower panel of Fig. 5.10, $\mathcal{U}_{(1)}$ is shown on a very short time scale, corresponding to 10-15 oscillation periods. During the hopping process, every local minimum of $\mathcal{U}_{(1)}$ is associated with a new cluster being visited by the hopping particle. On closer inspection, we realise that the exact mechanism that causes hopping remains unclear. In fact, no significant increase of $\mathcal{U}_{(1)}$ can be seen short before the particle leaves the cluster. This more subtle behaviour suggests that our level of description, which takes into account only single-particle potential energies, may be oversimplified. In principle, a full description of the system's total potential energy as a function of the coordinates of all particles would uncover the exact circumstances under which a particle can gather sufficient energy to leave its cluster. This high-dimensional problem may be hard to grasp at first, but methods apt to deal with it have been developed [45, 46].

In the following subsection we will see that, in spite of all its shortcomings, our simple, single-particle picture can be very useful, if we are interested in describing the effects of hopping processes by a macroscopic diffusion law.

5.2.3 Particle hopping viewed as an activated mechanism

In [23] a simple model description of diffusion in cluster crystals was put forward, in which diffusion is interpreted as an activated process. In this picture, particles are regarded as independent thermal oscillators in harmonic potential wells separated by barriers of height $\Delta\mathcal{U}$. Taking into account the contact with the heat bath of temperature T, the probability of a particle to have a total energy $E > 0$ is then given by

$$p(E) = \frac{\beta^3 E^2}{2}\, e^{-\beta E}. \tag{5.1}$$

In this expression, the first factor in the product on the right-hand side represents the density of states in an energy shell of width $\mathrm{d}E$ around E, whereas the second term is the Boltzmann factor. By the use of eq. (5.1) it is possible to obtain the probability $P_>(\Delta\mathcal{U})$ that the energy of the oscillator, E, exceeds the height of the potential barrier, $\Delta\mathcal{U}$, as

$$P_>(\Delta\mathcal{U}) = \int_{\Delta\mathcal{U}}^{\infty} p(E)\,\mathrm{d}E = e^{-\beta\Delta\mathcal{U}}\left[(\beta\Delta\mathcal{U})^2/2 + \beta\Delta\mathcal{U} + 1\right]. \tag{5.2}$$

A particle with $E > \Delta\mathcal{U}$ is assumed to hop to a neighbouring site, thus $P_>(\Delta\mathcal{U})$ may be regarded as a hopping probability. To estimate the density-dependent barrier
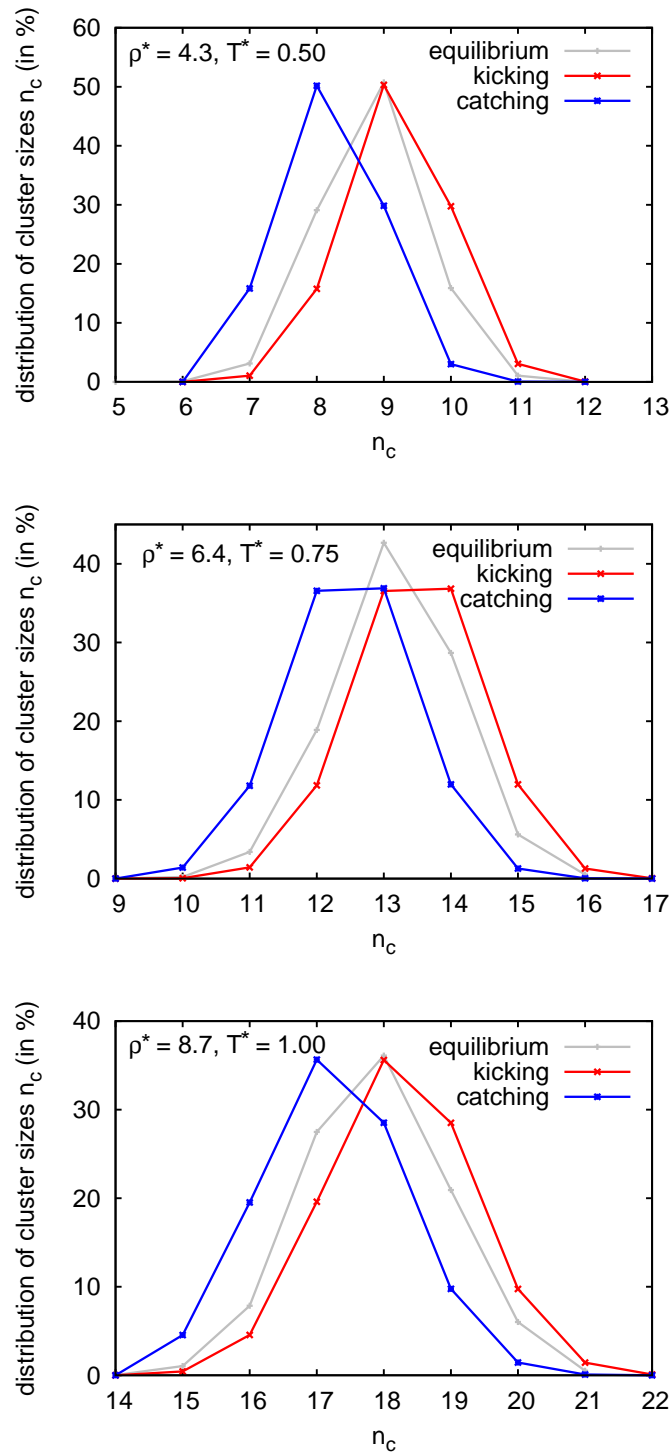
Figure 5.9: Distribution of cluster sizes, n_c, on average (grey), for "kicking" clusters (red), and for "catching" clusters (blue). The kicking and catching distributions are shifted to the right and to the left of the equilibrium cluster size distribution, respectively, indicating the tendency of hopping processes to relax cluster occupancy fluctuations in the crystal.
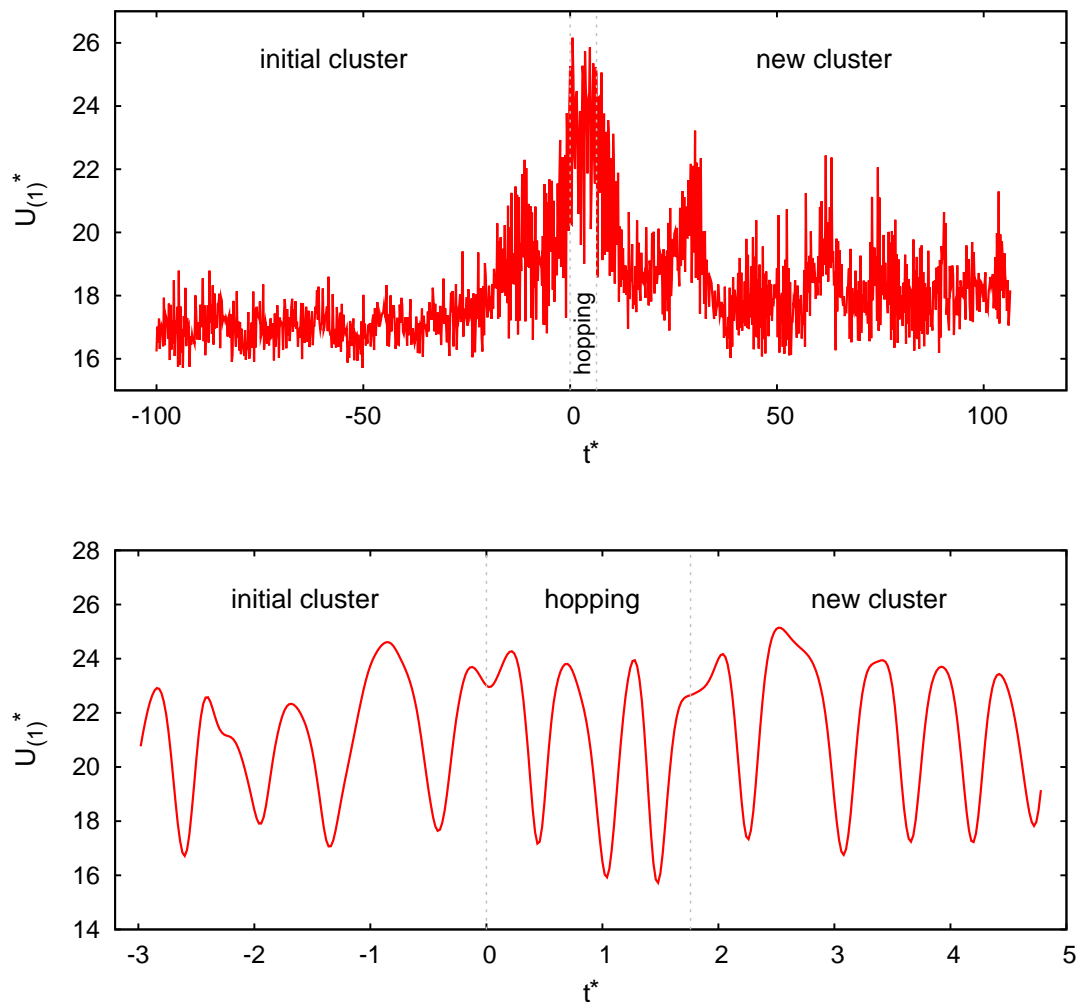
Figure 5.10: Typical time evolution of the single-particle potential energy, $\mathcal{U}_{(1)}^*$, of a hopping particle, illustrated for one state point $(\varrho^*, T^*) = (6.4, 0.80)$. The time window of the hopping event, as identified through our cluster analysis tool (cf. Section 3.3.1), is indicated by dotted vertical lines. In the upper panel we see how a hopping particle's potential energy is accumulated before and released after the hopping event. The displayed range in time comprises several hundreds of vibrational periods. The lower panel demonstrates that, on a shorter timescale, it is completely impossible to predict when and where a particle will start hopping to a new cluster. Every local minimum of $\mathcal{U}_{(1)}^*$ in the hopping time window is associated to a new cluster being visited by the hopping particle.

height $\Delta\mathcal{U}$, we benefit from the the single-particle potential energy wells that were used to measure the particle oscillation frequency in Chapter 4 (cf. Fig. 4.14). By averaging over the data available for densities $\varrho^* = 4.3$, 6.4, and 8.7 we obtain

$$\Delta\mathcal{U}^* \approx 1.30 \, \varrho^*. \tag{5.3}$$

From the standard theory of random walks [22, 23] the long-time diffusion coefficient in reduced units, D^*, then follows from eqs. (5.2) and (5.3) as

$$D^* = \gamma_0 \left[\frac{1.30}{2} \left(\frac{\varrho^*}{T^*} \right)^2 + 1.30 \, \frac{\varrho^*}{T^*} + 1 \right] e^{-1.30 \, \varrho^*/T^*}, \tag{5.4}$$

where γ_0 is a numerical coefficient introduced in [23] that is supposed to be related to the average distance that hopping particles travel through the crystal. The fact that D is solely dictated by the ratio ϱ/T was considered in [22, 23] as a dynamical extension of the scaling properties of $\langle n_\mathrm{c} \rangle$ and ϱ that had previously been found for the statics of clustering systems. In Fig. 5.11 our simulation data for the diffusion coefficient (presented in Tab. 5.1) are compared to eq. (5.4), using a numerically determined value of $\gamma_0 = 0.38$. Despite the considerable simplifications made to derive an expression for the diffusion coefficient, the agreement of simulation data and theoretical prediction is good.

It should be noted, however, that the $\Delta\mathcal{U}^*$ extracted from the data by a fitting function of the form of eq. (5.4) is appreciably larger than the one obtained by measuring the potential well barriers from Fig. 4.14. This is an indication of the limited validity of the simple diffusion model introduced in this subsection. On the one hand, this model describes hopping as a Markovian process, since the diffusion path is described as a random walk [23], and thus implicitly assumes that successive hops are uncorrelated. This is clearly not always the case, as we have demonstrated in our investigations of the length of hopping paths (cf. Fig. 5.6) and the distribution of angles between consecutive jumps (cf. Fig. 5.4) for correlated hopping events. On the other hand, the assumption of the harmonic shape of the potential well does not hold, as we can see from Fig. 5.12. Here, a refinement of eq. (5.4) might be achieved by including an anharmonic term in the effective site potential, $\Phi_\mathrm{site}(r_\mathrm{rel})$, which would model the actual shape of the well more accurately. This would correspond to describing the effective cluster site potentials as double well potentials. In this case, the probability distribution in eq. (5.1) has to be reconsidered and recalculated numerically, which will be part of future work on this subject.
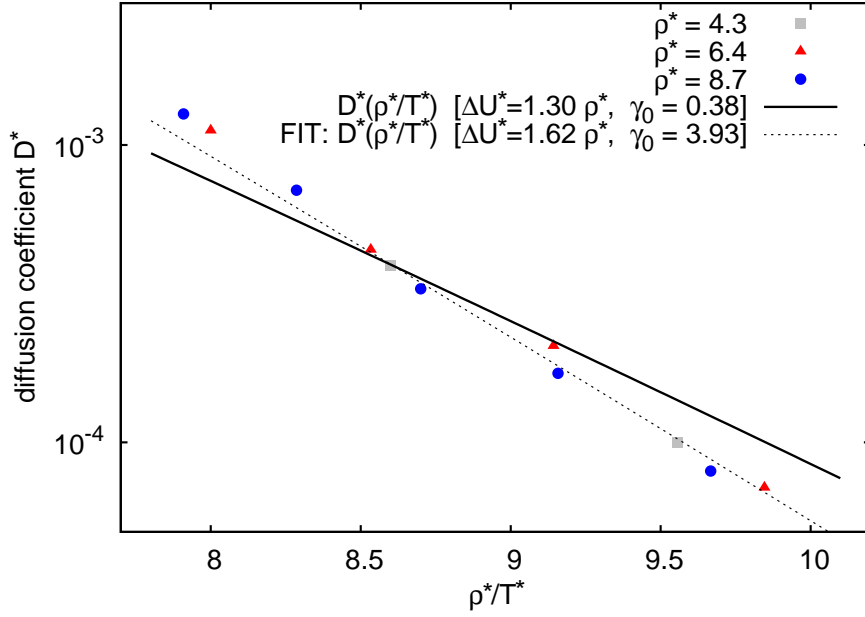
Figure 5.11: Diffusion coefficient D^* as a function of ϱ^*/T^* for different densities, ϱ^*, (coloured symbols). The black solid line represents data obtained via eq. (5.4) using $\gamma_0 = 0.38$. The black dashed line is a fit to the simulation data (cf. Tab. 5.1) using the same function, allowing to find the proportionality constant between $\Delta\mathcal{U}^*$ and ϱ^* from simulation data.
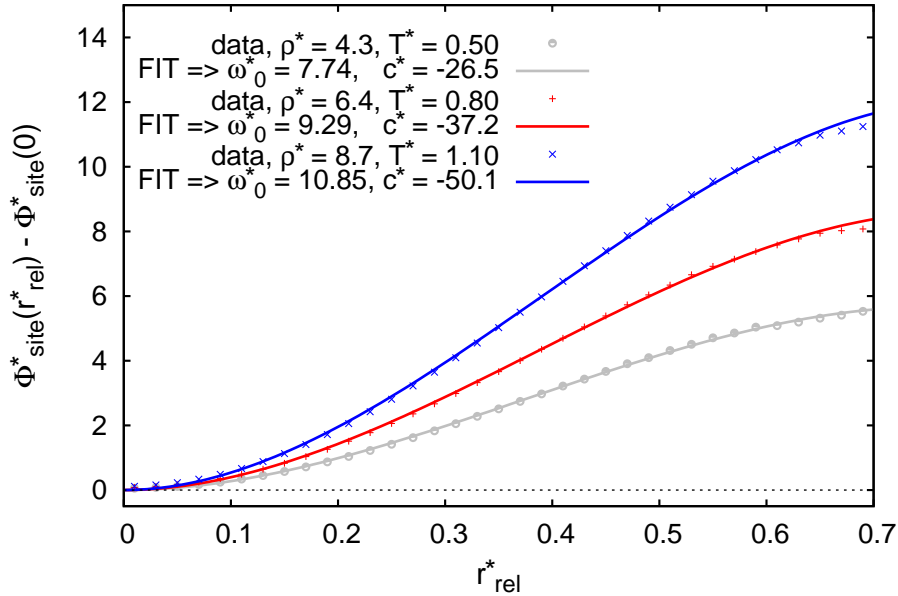

Figure 5.12: Description of the single-particle potential well in terms of an anharmonic well. The solid lines indicate fits to MD simulation data (represented by coloured symbols). The fitting function includes a cubic term in the effective site potential: $\Phi^*_{\text{site}}(0) + \omega_0^{*2}/2 \, r^{*2}_{\text{rel}} + c^* r^{*3}_{\text{rel}}$.

Conclusion

In this work, we have investigated the dynamics of cluster crystals formed by particles interacting via bounded, purely repulsive effective potentials. In recent years, this novel kind of soft matter system has attracted the interest of a broad scientific community, as these crystals were found to exhibit astonishing new features, such as a density-independent lattice constant, an unconventional way of responding to compression, or a remarkable diffusive behaviour [2, 3, 23].

We have characterised several aspects of vibrations and diffusion in cluster crystals by employing advanced molecular simulation techniques. Extensive Lattice Monte Carlo and molecular dynamics simulations have been carried out for a representative interaction model, the GEM-4 potential, in the region of the phase diagram where the fcc phase is stable. To analyse the system configurations generated in the simulations we have developed a cluster analysis tool which is capable of identifying cluster objects in an unambiguous manner and makes it possible to analyse particle trajectories with respect to the cluster centres of mass in time.

In the first part of our work, we focused on the spectrum of *vibrations* in a cluster crystal. We obtained the vibrational density of states both from the Fourier transform of the velocity auto-correlation function as well as from normal mode analysis. By the former approach we were able to separate the vibrational spectrum into a contribution of the particle velocity relative to the cluster centres of mass and a contribution of the centre of mass velocity. In this way, we demonstrated that there exists a fundamental difference between *single*-particle and *collective* vibrations in the system. The former corresponds to the motion of particles inside a cluster (*intra-cluster* motion), the latter to the motion of cluster centres of mass (*inter-cluster* motion). Normal mode analysis allowed us to further examine the properties of the main peak in the vibrational spectrum, which originates from single-particle motion. We detected high localisation of normal modes in the region of this peak and high *de*localisation in the remainder of the spectrum. The square of the main frequency of the peak was found to scale linearly with density, which has been anticipated in the description of particle oscillations as effectively harmonic one-particle motion, put forward in previous works [2]. Finally, we considered cluster crystals with both

monodisperse and polydisperse cluster occupancy numbers, in order to establish a connection to recent analytical, zero-temperature calculations of phonon dispersion relations in the system [44].

The second part of our work was dedicated to the diffusive behaviour of particles in a cluster crystal. We studied the particle *hopping* mechanism, which is responsible for diffusion in the system while maintaining the underlying lattice structure. We discovered that a significant contribution to the diffusivity in the system results from highly correlated particle hops connecting lattice sites separated by large distances. This points to the existence of two different diffusion mechanisms in cluster crystals: mere particle hopping from one cluster to one of its nearest neighbours, and "effectively ballistic" motion. When investigating the physical mechanism that leads to hopping processes, we demonstrated that particles tend to hop from overpopulated clusters to clusters of smaller size. This effect is, however, strongly superposed with cluster occupancy fluctuations that occur at random, regardless of the occupancy of kicking and catching clusters. In recent related works [22, 23], the diffusion coefficient in a cluster crystal was predicted to solely depend on the ratio between density and temperature, ϱ/T, in an exponential law. While this simple model already provides a reasonable first description, our analysis revealed two main shortcomings. First, the assumption that particle hopping processes may be regarded as uncorrelated does not hold in the case of long, correlated hops of particles over many lattice sites. Second, the single-particle potential energy well is in fact not harmonic. To describe its shape correctly, at least a cubic term in the effective cluster site potential has to be included. These last two findings call for a reconsideration of the model of diffusion in cluster crystals, which shall be part of future work on this subject.

Appendix A

Appendix

A.1 Common variable definitions in statistical mechanics

density ϱ

$$\varrho = \frac{N}{V} \tag{A.1}$$

inverse temperature β

$$\beta = \frac{1}{k_{\mathrm{B}}T} \tag{A.2}$$

de Broglie wavelength Λ

$$\Lambda = \sqrt{\frac{2\pi\beta\hbar^2}{m}} \tag{A.3}$$

A.2 Reduced units

density

$$\varrho^* = \varrho\sigma^3 \tag{A.4}$$

temperature

$$T^* = \frac{k_B T}{\varepsilon} \tag{A.5}$$

energy

$$E^* = \frac{E}{\varepsilon} \tag{A.6}$$

pressure

$$P^* = \frac{P\sigma^3}{\varepsilon} \qquad (A.7)$$

distance

$$r^* = r/\sigma \qquad (A.8)$$

wave vector

$$k^* = k\sigma \qquad (A.9)$$

time

$$t^* = \sqrt{\frac{\varepsilon}{m\sigma^2}}\, t \qquad (A.10)$$

frequency

$$\omega^* = \sqrt{\frac{m\sigma^2}{\varepsilon}}\, \omega \qquad (A.11)$$

diffusion coefficient

$$D^* = \sqrt{\frac{m}{\varepsilon\sigma^2}}\, D \qquad (A.12)$$

Bibliography

[1] C. N. Likos. Phys. Rep. **348**, 267 (2001).

[2] C. N. Likos, B. M. Mladek, D. Gottwald, and G. Kahl. J. Chem. Phys. **126**, 224502 (2007).

[3] B. M. Mladek, P. Charbonneau, and D. Frenkel. Phys. Rev. Lett. **99**, 235702 (2007).

[4] B. M. Mladek, G. Kahl, and C. N. Likos. Phys. Rev. Lett. **100**, 028301 (2008).

[5] C. N. Likos, M. Schmidt, H. Löwen, M. Ballauff, D. Pötschke, and P. Lindner. Macromolecules **34**, 2914 (2001).

[6] B. M. Mladek, M. J. Fernaud, G. Kahl, and M. Neumann. Condens. Matter Phys. **8**, 135 (2005).

[7] F. H. Stillinger. J. Chem. Phys. **65**, 3968 (1976).

[8] C. N. Likos, M. Watzlawek, and H. Löwen. Phys. Rev. E **58**, 3135 (1998).

[9] B. M. Mladek. *Exotic phenomena in the phase behaviour of soft matter systems*. PhD thesis. University of Technology Vienna (2007) (http://tph.tuwien.ac.at/smt/extra/publications/phd/mladek.pdf).

[10] C. N. Likos, A. Lang, M. Watzlawek, and H. Löwen. Phys. Rev. E **63**, 031206 (2001).

[11] B. M. Mladek, G. Kahl, and M. Neumann. J. Chem. Phys. **124**, 064503 (2006).

[12] J. H. Holland. *Adaption in Natural and Artificial Systems*. The University of Michigan Press (1975).

[13] D. Gottwald. *Genetic Algorithms in Condensed Matter Theory*. PhD thesis. University of Technology Vienna (2005) (http://tph.tuwien.ac.at/smt/extra/people/gottwald/phd.pdf).

[14] D. Gottwald, G. Kahl, and C. N. Likos. J. Chem. Phys. **122**, 204503 (2005).

[15] B. M. Mladek, D. Gottwald, G. Kahl, M. Neumann, and C. N. Likos. J. Phys. Chem. B **111**, 12799 (2007).

[16] R. Evans. *Density Functionals in the Theory of Nonuniform Fluids*. Fundamentals of Inhomogeneous Fluids, edited by D. Henderson. Marcel Dekker (1992).

[17] B. M. Mladek, P. Charbonneau, C. N. Likos, D. Frenkel, and G. Kahl. J. Phys.: Condens. Matter **20**, 494245 (2008).

[18] D. Frenkel and B. Smit. *Understanding Molecular Simulation*. Academic Press, 2nd edition (2002).

[19] D. Frenkel and A. J. C. Ladd. J. Chem. Phys. **81**, 3188 (1984).

[20] B. M. Mladek, D. Gottwald, G. Kahl, M. Neumann, and C. N. Likos. Phys. Rev. Lett. **96**, 045701 (2006).

[21] B. M. Mladek, D. Gottwald, G. Kahl, M. Neumann, and C. N. Likos. Phys. Rev. Lett. **97**, 019901(E) (2006).

[22] C. N. Likos, B. M. Mladek, A. J. Moreno, D. Gottwald, and G. Kahl. Comp. Phys. Comm. **179**, 71 (2008).

[23] A. J. Moreno and C. N. Likos. Phys. Rev. Lett. **99**, 107801 (2007).

[24] N. W. Ashcroft and N. D. Mermin. *Solid State Physics*. Saunders College Publishing, international edition (1976).

[25] M. P. Allen and J. Tildesley. *Computer Simulation of Liquids*. Clarendon Press, Oxford, reprinted edition (1990).

[26] L. R. Pratt and S. W. Haan. J. Chem. Phys. **74**, 1864 (1981).

[27] J.-P. Hansen and I. R. McDonald. *Theory of Simple Liquids*. Academic Press, 3rd edition (2006).

[28] N. Metropolis, A. W. Rosenbluth, M. N. Rosenbluth, A. H. Teller, and E. Teller. J. Chem. Phys. **21**, 1087 (1953).

[29] N. Metropolis and S. Ulam. J. Am. Stat. Assoc. **44**, 335 (1949).

[30] A. Z. Panagiotopoulos. J. Chem. Phys. **112**, 7132 (2000).

[31] H. Fragner. Comput. Phys. Commun. **176**, 327 (2007).

[32] H. Fragner. *Lattice Monte Carlo Simulation mit rekonfigurierbaren Prozessoren*. PhD thesis. University of Vienna (2005).

[33] B. Widom. J. Chem. Phys. **39**, 2808 (1963).

[34] L. Verlet. Phys. Rev. **159**, 98 (1967).

[35] W. C. Swope, H. C. Andersen, P. H. Berens, and K. R. Wilson. J. Chem. Phys. **76**, 637 (1982).

[36] T. A. Andrea, W. C. Swope, and H. C. Andersen. J. Chem. Phys. **79**, 4576 (1983).

[37] L. D. Landau and E. M. Lifschitz. *Statistical Physics*, volume 5 of *Course of Theoretical Physics*. Butterworth-Heinemann, 3rd edition (1980).

[38] L. E. Reichl. *A Modern Course in Statistical Physics*. Wiley-Interscience, 2nd edition (1998).

[39] K. Petersen. *Ergodic Theory*. Cambridge University Press (1989).

[40] D. Coslovich. *Connections between structure, dynamics, and energy landscape in simple models of glass-forming liquids*. PhD thesis. University of Trieste (2007) (http://www.openstarts.units.it/dspace/handle/10077/2563).

[41] W. H. Press, B. P. Flannery, S. A. Teukolsky, and W. T. Vetterling. *Numerical Recipes in Fortran*. Cambridge University Press (1992).

[42] D. C. Liu and J. Nocedal. Math. Program. **45**, 503 (1989).

[43] S. D. Bembenek and B. B. Laird. J. Chem. Phys. **104**, 5199 (1996).

[44] T. Neuhaus. *Phonon Spectra of Cluster Crystals*. Master's thesis. Heinrich Heine University of Düsseldorf (2009).

[45] H. Jónsson, G. Mills, and K. W. Jacobsen. *Nudged elastic band method for finding minimum energy paths of transitions*. Classical and Quantum Dynamics in Condensed Phase Simulations, edited by B. J. Berne, G. Ciccotti, and D. F. Coker. World Scientific, Singapore (1998).

[46] C. Dellago, P. Bolhuis, F. S. Csajka, and D. Chandler. J. Chem. Phys. **108**, 1964 (1998).

Acknowledgements

During the years of my studies and the time I spent working on this thesis in particular, I was surrounded by a lot of people who accompanied me on my way and provided help and support whenever needed. I would like to thank . . .

Daniele Coslovich, for guiding me throughout this work, from the very basics of scripting and programming up to the completion of my thesis. For your patience in answering my questions, supporting my own ideas, and the time spent for extensive discussions about diverse subjects related to my work.

Gerhard Kahl, for your support and encouragement. For providing a friendly and relaxed working atmosphere in your group, and making it possible to meet a couple of very interesting people, here and abroad.

Bianca Mladek, for warmly welcoming me for a two-week visit at the Department of Chemistry at University of Cambridge. For taking your time to explain your work to me in full detail and developing a helpful extension of your code.

Daan Frenkel and **Christos Likos**, for enlightening discussions on the peculiarities of cluster crystals and your motivation to continue my work in this field.

The members of the soft matter theory group at TU Wien **Camille Jouvie**, **Dieter Schwanzer**, **Emanuela Bianchi**, **Günther Doppelbauer**, and **Jan Kurzidim**, for good company during lunch hours and many interesting discussions about physics and beyond.

My fellow students and friends. **Christoph**, **Hannes**, and **Hansi** for happy years of study and many convivial evenings, and for not mincing your words in whatever situation. **Birgit**, **Christian**, **Florian**, and **Lukas**, simply for being friends over so many years.

Meinen Eltern **Helga** und **Rudi**, für eure Unterstützung und Liebe, euer Vertrauen in meine Entscheidungen und Vorhaben und für all das, was mir dadurch erst ermöglicht wurde. Meinem Bruder **Martin**, für Gespräche und gemeinsame sportliche und musikalische Aktivitäten. **Meinen Großmüttern**, für die Sorge um das Wohl eurer Großfamilie und den ungebrochenen Enthusiasmus, den ihr euren Enkelkindern entgegenbringt. Meiner ganzen Familie.

Vroni, für deine Unterstützung und Liebe, deine Geduld, und deine Ermutigungen in Momenten des Selbstzweifels.